

Master Thesis

Exploring the mechanics of DNA origami nanopores
via DNA PAINT imaging

Materials Science and Engineering Department
Delft University of Technology

Paraskevi Kesapidou

Supervisors: Sabina Caneva
ZeYu
Georgy Filonenko



Acknowledgements

I am immensely grateful to Lilian Voudouri and the Onassis Foundation for their generous financial support, which has been instrumental in facilitating my entire master's degree journey and educational pursuits.

I would like to express my deepest gratitude to my supervisor, Sabina Caneva and ZeYu, for their unwavering support, guidance, and invaluable insights throughout the entire research process. Their mentorship has been instrumental in shaping the trajectory of this work. I am also indebted to Yabin Wang, who is a member of the DNA team and has been giving me constructive feedback and thoughtful contributions that greatly enriched the quality of this thesis.

I extend heartfelt appreciation to my family Konstantinos, Vaia and Antonis, who were always there for me providing me with everything I needed and supporting me unconditionally in every step. Additionally, to my dear friends in Greece Nikos, Anastasia and Dimitris, despite the geographical distance that separates us. Your unwavering support, friendship, and virtual presence have been a constant source of strength and joy. Your encouragement transcends borders, and I am profoundly grateful for the enduring connection that bridges the miles. Σας ευχαριστώ πολύ!

I am very grateful for Riccardo, for his constant support and understanding. His encouragement and help have been a grounding force, providing me with strength during this academic pursuit. Moreover, I am immensely thankful for the presence of my friends here in the Netherlands, Maria, Aravind, Stefano, Yuze, Roberto, Harsh and Liam. Your companionship, laughter, and shared moments have added warmth and joy to my academic journey. Our frequent gatherings have been a source of support making this experience truly memorable.

Finally, I want to express my gratitude to all those individuals whose names may not appear here but who, in various ways, have contributed to the completion of this thesis. Thank you for being a part of this academic endeavor.

Content

| | |
|--|----|
| Abstract | 4 |
| 1. Introduction | 5 |
| 1.1. Nanopores and their applications..... | 5 |
| 1.2. DNA and DNA origami..... | 6 |
| 1.3. DNA origami nanoactuators..... | 7 |
| 1.3.1. Trident-Shaped Nanoactuators..... | 7 |
| 1.3.2. DNA nanoactuator for 2D lattices..... | 8 |
| 1.3.3. Autonomous self-assembled DNA origami nanoactuator..... | 9 |
| 1.3.4. DNA motor triggered by pH..... | 10 |
| 1.3.5. Spring loaded nanosensors..... | 11 |
| 2. Characterization of DNA origami nanostructures | 12 |
| 2.1. Atomic Force Microscopy (AFM)..... | 12 |
| 2.2. Transmission Electron Microscopy (TEM)..... | 14 |
| 2.3. Fluorescence Microscopy..... | 15 |
| 2.3.1. Epifluorescence wide-field Microscopy..... | 16 |
| 2.3.2. Confocal Microscopy..... | 17 |
| 2.3.3. Total Internal Reflection Fluorescence (TIRF) Microscopy..... | 18 |
| 2.3.4. Super Resolution Microscopy..... | 20 |
| 2.3.4.1. SIM/STED/PALM/STORM..... | 21 |
| 2.3.4.2. DNA PAINT..... | 22 |
| 2.3.4.3. Forster Resonance Energy Transfer (FRET)..... | 23 |
| 3. Research Question and Objectives | 23 |
| 4. Methods | 26 |
| 4.1. Design of the nanopores..... | 26 |
| 4.2. Assembly of the DNA origami nanopores..... | 28 |
| 4.3. Purification of DNA origami nanopores..... | 28 |
| 4.4. Gel electrophoresis..... | 28 |
| 4.5. Sample preparation and imaging for TIRF..... | 29 |
| 4.6. Atomic Force Microscopy (AFM)..... | 32 |
| 4.7. Data analysis..... | 33 |
| 5. Results and Discussion | 34 |
| 5.1. Simulations..... | 34 |
| 5.2. Gel electrophoresis..... | 35 |
| 5.3. Atomic Force Microscopy (AFM)..... | 37 |
| 5.4. Total Internal Reflection Fluorescence (TIRF) Microscopy..... | 43 |
| 5.4.1. Fundamental Components of Sample Preparation..... | 43 |

| | |
|--|----|
| 5.4.2. Experiments with sealed chamber..... | 44 |
| 5.4.3. Experiments with non-sealed chamber..... | 46 |
| 5.4.3.1. Different Buffer solution concentrations..... | 46 |
| 5.4.3.2. Different DNA origami nanopore solution concentrations..... | 51 |
| 5.4.3.3. Different laser power from the microscope..... | 55 |
| 5.4.3.4. Different exposure time..... | 58 |
| 5.4.3.5. Different waiting and duration time..... | 61 |
| 6. Conclusions..... | 65 |
| 7. Appendix..... | 68 |
| 8. References..... | 74 |

Abstract

Nanopores are narrow channels in cell membranes that control the passage of small molecules. In recent years, they have been repurposed for diverse applications, including single molecule sensing and drug delivery. Due to the small diameters of conventional protein-based, current research efforts are directed to designing nanopores from other materials to achieve larger diameters. DNA origami has emerged as a promising method for the precise fabrication of nanoscale structures. Using advances in structurally-adaptable DNA origami nanotechnology, here we investigate DNA-based nanoactuators with size-adjustable diameters, which can potentially reach diameters of up to 100 nm, that could be used for macromolecules translocation. The focus of this thesis is the study of the mechanical states of these nanoactuators, which can be triggered to change shape in response to a specific molecular trigger. Given the nanoscopic dimensions of our actuators, we select DNA PAINT for imaging, which is a type of super resolution technique, that can achieve a resolution of 10 nm, beating the optical diffraction limit (~200 nm) of conventional light microscopy. DNA PAINT experiments are performed in combination with total internal reflection fluorescence (TIRF) microscopy to characterize the behavior of DNA origami nanopores in physiological conditions. By testing various parameters sample related and imaging software ones we identify optimal conditions suggesting 5mM Mg^{2+} ions in buffer solution and 1nM DNA nanopores. Laser power (40mW), exposure time (400ms), waiting time between frames (300ms), and image duration (50s) are optimized, resulting in the expected fluorescent blinking behavior which enables us to perform single-molecule localization. The individual corners of the nanopores were, however, not resolved with this technique due to limitations in the resolution of the imaging system. We recommend that future work could exploit the even better resolution of a modified DNA PAINT approach i.e. Exchange PAINT, which has been proven to achieve Angstrom level resolution for imaging of DNA nanostructures.

1.Introduction

1.1. Nanopores and their applications

Nanopores are nanostructures that have as main characteristics an open channel surrounded by a biological membrane. They are important to cells, as they act as gatekeepers, regulating the passage of ions and nutrients through cell membranes to maintain proper function. [1] An important application is single molecule detection and biosensing, in which individual molecules can be analyzed, and we can have information about the molecules' size and/or sequence. More specifically, we can connect two reservoirs with electrolyte solution when the nanopore is in aqueous environment, and when a voltage is applied an ionic current passes through the channel. Once a single molecule passes through the pore, the ionic current gets blocked, as the molecule reduces the ions flowing. By monitoring the ionic current flow from the channel and the disruptions present due to the single molecules, we can detect the molecules. [1],[2] Other applications in which they can be used are controlled drug release, by functionalizing them with stimuli-responsive molecules that change their conformation in response to specific triggers. These conformational changes can then be used to regulate the release of drugs through the nanopore. One of the key advantages of nanopores lies in their ability to regulate the release of drugs on a nanoscale level, allowing for sustained and targeted delivery to specific cells or tissues. The controlled release through nanopores can be tailored based on factors like size, shape, and surface properties of the nanostructures, enabling tunable drug delivery kinetics. This precision in drug delivery can minimize side effects, improve therapeutic efficacy, and pave the way for innovative approaches in personalized medicine. [3],[4]

There are different types of nanopores that can be found in nature or are synthesized in the lab. An example of the former are protein nanopores, while the latter includes artificial nanopores can be assembled from DNA. Protein nanopores are constructed from amino acids and exhibit small diameters, which are usually from 1-5 nm, while DNA-based nanopores exhibit larger dimensions with diameters that can range from 2-30 nm. For protein nanopores, the design and engineering through modifications of protein structures requires dedicated protein expression and purification facilities. It is therefore challenging to achieve de novo design, which is creating an entirely new protein from scratch. On the other hand, DNA nanopores are more easily designed, as DNA is a programmable molecule, with a resulting structure that is based on a simple base-pairing rule. [2] DNA nanopores offer more variety in terms of their size and shape, and more easy adoption by non-specialized labs due to easy design and fabrication protocols. Compared to protein pores, DNA nanopores are more stable in various conditions of pH or temperature and can be produced in high yields of identical copies. [1]

Due to the small and fixed diameter size, both of conventional protein and DNA nanopores result in limiting the size of molecules that can pass through. This can be a constraint for applications that require the delivery of larger molecules (macromolecules) for therapeutic applications, rather than only ions and nano-sized molecules. Therefore there is a need to find

different designs that can achieve the passage of macromolecules. Specifically, DNA-based nanostructures can be very useful, since they can be built with larger channel dimensions. The next section will provide an overview of possible approaches to generate shape-changeable nanopores, featuring larger diameters. We term these DNA origami nanoactuators for their ability to adopt different shapes in a pre-determined manner.

1.2. DNA and DNA origami

DNA nanoactuators are made of DNA and are structures that respond with mechanical movement in response to an external stimulus. DNA is a double stranded biomolecule. Each strand consists of four different types of nucleotides, made up of one sugar molecule (deoxyribose), a phosphate group and a nitrogenous base molecule. The latter involves one of the nitrogenous bases in each nucleotide (Adenine (A), Thymine (T), Cytosine (C), and Guanine (G)), which can form specific base pairs with each other (A-T and C-G), giving DNA its characteristic double helix form. (Figure 1)[5]

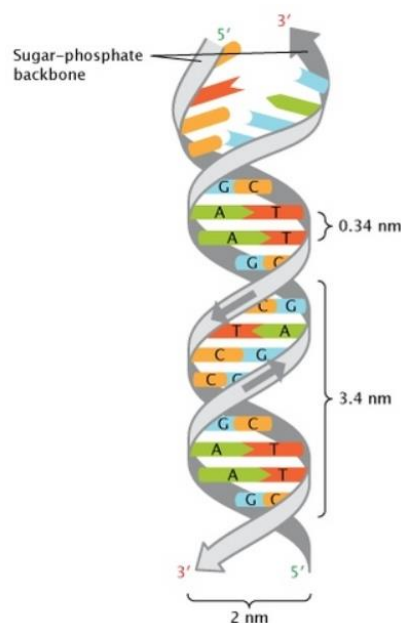


Figure 1: Representation of the double helix structure of DNA.[5]

DNA nanoactuators can be fabricated by using a technique called DNA origami nanotechnology. DNA origami is a bottom-up fabrication technique that enables the fabrication of well-defined nanostructures made entirely out of DNA. Specifically, the predictable base pairing behavior allows for the precise design and construction of DNA structures at the nanoscale. By carefully selecting the sequence of nucleotides in a synthetic DNA strand, researchers can program the strand to fold into specific shapes and structures. DNA origami involves a long single-stranded scaffold that can be folded to generate 2D and 3D objects. The folding is carried out by using hundreds of single-stranded DNA staple strands that hybridize at specific positions on the scaffold and collectively fold it into the desired nanostructure, while annealing. A representative image of the components necessary for this method are shown in Figure 8. This approach provides precise control over the geometry of the structure, which can be designed in an automated manner by programming the DNA

sequences, and several open source tools have been developed to aid the design process. Due to the self-assembly process, DNA origamis can be produced with very high yields, producing millions of identical copies from a single assembly process. Beyond static structures, this method is also able to fabricate mechanically dynamic nanostructures, which can mimic mechanical machines at the macroscopic level. Additionally, the programmability of the DNA origami fabrication method provides control over the surface functionality and chemistry, since it allows for the precise placement of chemical groups onto the surface, and these can be used to trigger reactions that lead to actuation. [6],[7]

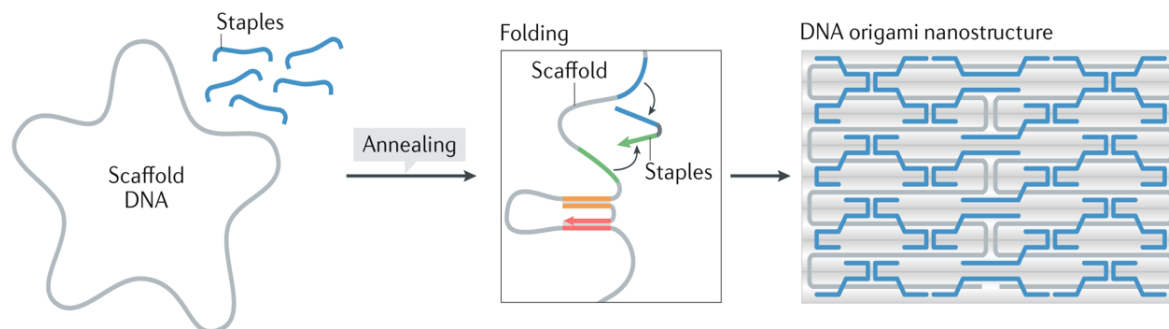


Figure 8: DNA scaffold that can hybridize with the staple strands due to sequence complementarity. [6]

1.3. DNA origami nanoactuators

DNA origami nanoactuators are important to study because they have the potential to be applied in various applications such as in drug delivery, biosensing, nanorobotics and nanoelectronics. Depending on the different geometry and surface chemistry we can manipulate them through external stimuli in order to control their mechanical movements. These movements can be used, for instance, to release drugs, in the case of nanoactuators being used as drug delivery carriers. DNA nanoactuators can be a very efficient way for drug delivery use, since the surface chemistry can allow for the dynamic behavior, which is necessary for the release of the drug. Additionally, DNA is a biocompatible material, which reduces the risk of reactions that could cause toxicity and harm to the cells, and is also biodegradable, allows it to be eventually removed from the body. Finally, it is possible to functionalize the surface of DNA nanostructures, in order to place certain ligands that can bind to specific cells, accomplishing the stochastic drug release in this way. [8]

There are several nanoactuator examples that have been developed in the field, which will be briefly discussed in the state-of-the-art review below.

1.3.1. Trident-Shaped nanoactuator

This is a type of DNA nanoactuator system that can adopt four distinct structural states by utilizing trident-shaped DNA (TS DNA) as a mechanical scaffold. The TS DNA nanoactuator contains three "arms," and biomolecules such as fluorescent/quenching molecules. The nanoactuator design is shown in Figure 2. The distances between the three arms of the TS DNA nanoactuator can be reversibly tuned using a process called strand displacement

reaction. This reaction involves the use of complementary DNA strands (Fuel and anti-Fuel) that can hybridize to the existing DNA strands, leading to the displacement of the original strands and changes in the overall structure of the nanoactuator. It has been demonstrated that the efficiency of the two-enzyme cascade reaction can be spatially regulated by switching the nanoactuator between opened, semi-opened, and closed states. An enzyme cascade is a biochemical process in which the product of one reaction serves as the reactant of the next one leading to a series of enzymatic reactions. In the open state, the two enzymes are separated and have lower reaction efficiency. In the semi-opened state, the distance between the two enzymes is reduced, leading to increased reaction efficiency. In the closed state, the two enzymes are brought into close proximity, leading to the highest reaction efficiency. Gold nanoparticles (AuNPs) can be tethered to the arms, in order to make it easier for visualization. Additionally, glucose oxidase (GOx) and horse-radish peroxidase (HRP) are attached to the two outer arms of the TS DNA nanoactuator. GOx and HRP are enzymes commonly used in biotechnology and biochemistry due to their ability to catalyze specific reactions with high efficiency. This new TS DNA nanoactuator system provides a platform for designing complicated enzyme cascade systems and could find application in diagnostic and therapeutic applications. The characterisation methods that have been used for revealing information about this nanoactuator are AFM, agarose gel electrophoresis, TEM and fluorescent/quenching microscopy. [9]

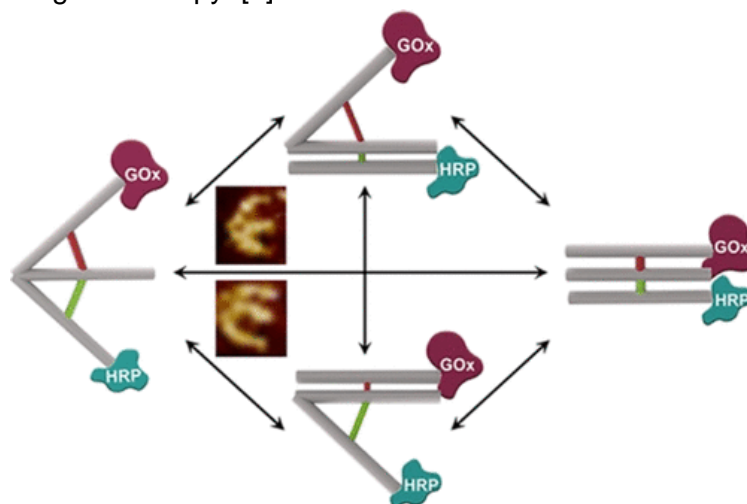


Figure 2: Conformational change of Trident-Shaped nanoactuator. [9]

1.3.2. DNA origami nanoactuator for 2D lattices

The device consists of two sets of DNA strands (S1 and S2) that are initially in their complementary duplex form. The nanoactuator schematics and the operation are shown in Figure 3. To initiate the conformational change, the set strand (SS1 in red), that is already bound to the structure, is removed from the duplex by the addition of a fuel strand (FS1 in green), which is complementary to the set strand. The fuel strand displaces the set strand from its complementary strand by forming a more stable duplex with it. In the first step, the nanoactuator is in the S1 state and with the addition of FS1 an unpaired intermediate (INT) state is formed. In the second step, the INT is fixed to S2 state by the addition of SS2 (a set strand in blue), forming a stable duplex structure. In the third step, FS2 (a fuel strand in purple) is added to remove SS2, converting S2 back to the unpaired intermediate (INT). Finally, SS1 is added to restore the S1 state and complete the cycle. This process results in a conformational change of the nanoactuator device, with the two sets of DNA strands moving

relative to each other by two turns of the helix, which corresponds to a displacement of approximately 6.8 nanometers. This device can be incorporated into a 2D DNA lattice. More specifically, two nanoactuator devices were incorporated in two opposite edges, forming a rhombus-like cavity of 14 nm and then participating in 2D lattices. These devices are useful for controlled nanofabrication of molecular nanoelectronic wires for electronic components and devices on a molecular scale. In this way, we can have fabricated structures in 2D and 3D arrays that would have an 'on' and 'off' state. Another application can be the manipulating and transporting of molecules that are attached to the tiling arrays of the device. By programming the movement of the motor devices, it is possible to selectively transport molecules or nanoparticles to specific locations on the tiling array. This could be used, for example, to transport reactants to specific locations in a chemical reaction, enabling the programmed synthesis of specific molecules. For the analysis, gel electrophoresis was used, while, for the motion of the 2D DNA lattice, AFM was used by depositing the sample in mica substrate and FRET by binding covalently the donor and acceptor dyes in the structure. [10]

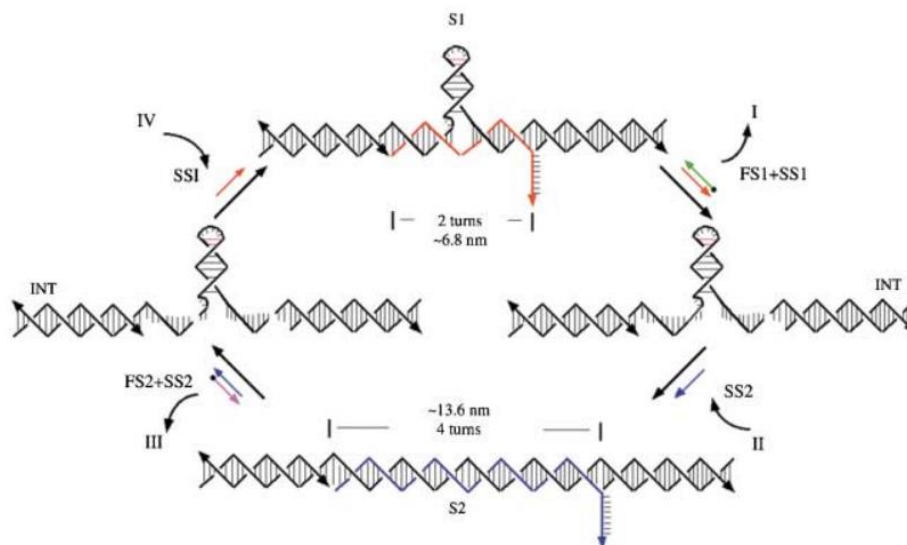


Figure 3: Schematic of the design and operation of the duplex nanoactuator. [10]

1.3.3. Autonomous self-assembled DNA origami nanoactuator

In this case a self-assembled DNA origami structure is created that can undergo conformational changes in response to external stimuli. The structure is 2D, with an external ring of 60 nm and internal disc of 20 nm linked to each other in the two opposite points, can be seen in Figure 4. At the surface of the disc a single stranded DNA molecule is placed called the probe (yellow color in the Figure), which was designed to be fully complementary to a hairpin target molecule, during hybridization results in a tensile force on the internal disc. To introduce reversibility, the scientists used a partially complementary target and probe, which allowed for wing movement upon binding, as shown in Figure 5. A fully complementary competitor was used to bind to the target to reverse the procedure and leave the probe unbound. This nanoactuator can be used in electrical components, given its ability to switch from on to off and back again. The nanodevice was characterized using liquid-phase AFM, and FRET was used by attaching a fluorophore molecule to the edge of one side of the internal disc and a quencher attached to the external ring, very close to the fluorophore. Gel electrophoresis was used to confirm the successful folding of DNA strands into the desired shape during the assembly process. [11]

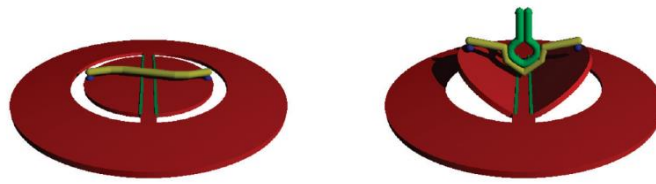


Figure 4: Schematic model of the DNA origami. [11]

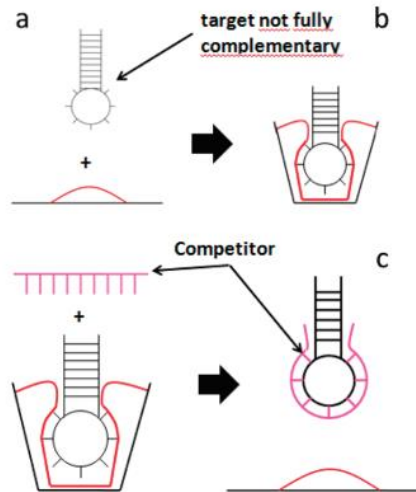


Figure 5: Schematics of the reversible modes of the nanoactuator. [11]

1.3.4. DNA motor triggered by pH

In this example a DNA tweezers are presented as a real time sensor of pH. A DNA tweezer that is attached to the cell membrane with a cholesterol group, in order to ensure that it is in close proximity with the cell surface and its function is to sense the extracellular pH. The structure of such a motor is depicted in Figure 6. The DNA tweezer consists of a DNA frame that has been labeled with cholesterol, an i-motif domain in the middle, and a pair of fluorophores that can undergo FRET. The i-motif domain is a specific type of DNA structure that can form in slightly acidic conditions. When the cell is in a slightly acidic environment, the i-motif domain forms in the middle of the DNA tweezer, causing it to close and bring the two fluorophores close together. This results in a high FRET signal, which can be detected using fluorescence microscopy. On the other hand, when the cell is in a neutral environment, the i-motif domain does not form, because it is not stable at such pH values and the DNA tweezer remains open, separating the two fluorophores. This results in a low FRET signal. [12]

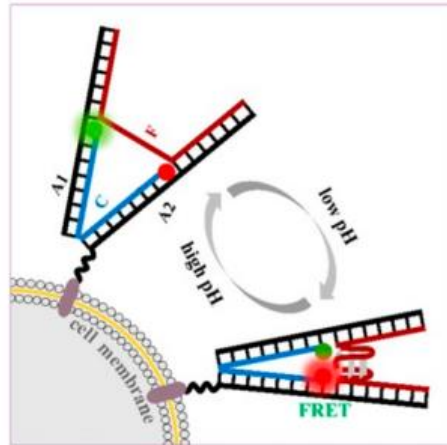


Figure 6: DNA motor triggered by different pH values. [12]

1.3.5. Spring loaded nanosensors

In this example the scientists designed a rhombus shaped nanoactuator, with four arms, each of which is approximately 60nm. This device has locking strands at the top and bottom corner, as shown in Figure 7. The diameter can vary and reach up to 100nm, as the nanostructure has the ability to exist in two different states. There are three different mechanisms in which the nanoactuators transform from a closed to open state:

1) Changing the buffer concentration. In this case the nanoactuator uses G-quadruplex DNA structures as sensing elements. The device consists of six strands of DNA, three top-corner locking strands, and three bottom-corner locking strands. Each locking strand has a 34-base single-stranded overhang with a specific sequence, which is stable in the presence of K⁺ ions. G-quadruplexes are structures that can form in single-stranded DNA sequences that are rich in G-base. In the presence of K⁺, the single-stranded overhangs of the locking strands can form stable G-quadruplex structures, which lock the top and bottom strands together, resulting in a closed conformation. When K⁺ is selectively removed from the system using buffer exchange, the G-quadruplex structures become unstable, and the device transitions to an open conformation.

2) Specific recognition of the palindromic sequence by the restriction enzyme BamHI, which cleaves the DNA locking strands and allows the device to open. The pre-stressed enzyme-sensitive origami device consists of DNA locking strands that contain a specific sequence with a palindromic region, which allows the locking strands to form dimers that are recognizable by the BamHI enzyme. The device is pre-stressed, meaning it is in a closed conformation due to the interactions between the locking strands. When the device is incubated with BamHI, the enzyme recognizes and binds to the palindromic sequence in the locking strands, causing them to cleave and allowing the device to open.

3) Nucleic-acid sensitive activation. A 12-base toehold single strand is used as complementary to a segment of the DNA strand in the top and bottom corner of the nanoactuator. However, the toehold single strand is also complementary to miR-210. So when

the miR-210 strands are also present, they bind to the toehold strand and then the toe hold single strand on the DNA is left with no hybridization binding. This is the initiation of the configurational change of the DNA nanoactuator. The 20-base lock strand gives the optimum result to yield the opening of the nanopore and detection of miR-210. [13]

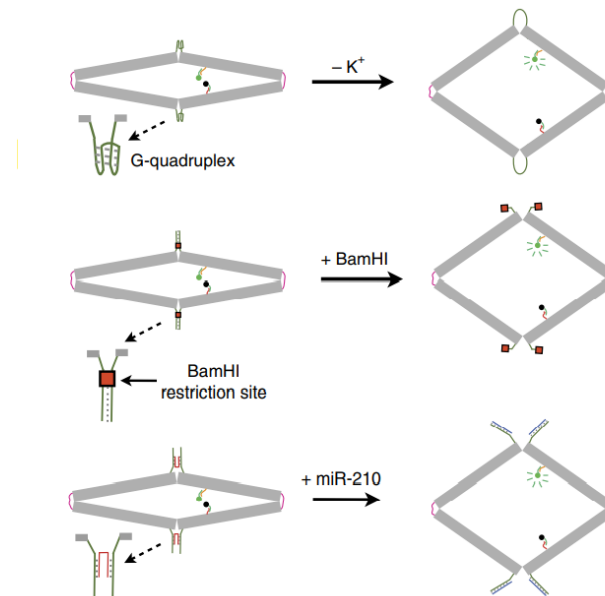


Figure 7: Design of spring loaded nanoactuators.[13]

The last example of DNA nanoactuators, has been an inspiration for our project, since the diameter is not fixed. The nanoactuator can reach up to 100nm of size when in open state, which makes it promising for the translocation of larger molecules.

2. Characterization of DNA origami nanostructures

It is crucial to conduct a thorough investigation and analysis of the DNA nanoactuators' structure and behavior after their design and synthesis to ensure they function as intended. A variety of techniques are commonly employed for characterizing nanoscale materials, including soft biological materials. These techniques play a key role in determining whether the DNA nanoactuators function as efficient nanopores, i.e with reliable open and close cycles upon triggering. In the following section we review the techniques and we select the optimal ones.

2.1. Atomic Force Microscopy (AFM)

Atomic Force Microscopy (AFM) is a powerful technique that allows for high resolution imaging of surfaces at the nanoscale level. It works by scanning a sharp tip over the surface of the sample while measuring the forces between the tip and the sample. It is used in a wide variety of fields including materials science, nanotechnology and biology. As can be seen on the left of Figure 9a), the sharp tip on the bottom of a reflective cantilever is scanned across the sample acquiring the topography of the sample line by line. During this whole process the

cantilever bends, because of the forces between the tip and the sample. This bending is detected from the reflection of a laser source that hits the back side of the cantilever. The photodiode detecting the light converts it into voltage, which is read by the feedback loop. The role of the feedback loop is to maintain the force or the amplitude of the cantilever constant, depending on the mode that is used. AFM can be operated in a variety of modes but two of them are most frequently used: contact and tapping mode. In contact mode the process is the same as described above, the feedback loop used to maintain a constant force between the tip and the sample. It is not the most suitable mode to study the topography of a biological soft sample, as the tip is in constant contact with it, thus the sample is more prone to get damaged. On the other hand, in tapping mode the tip oscillates at its resonance frequency above the sample, without being constantly in contact. This makes it more appropriate for the studying of biological material. The feedback loop in this case makes sure to maintain the amplitude of the oscillation stable. [14]

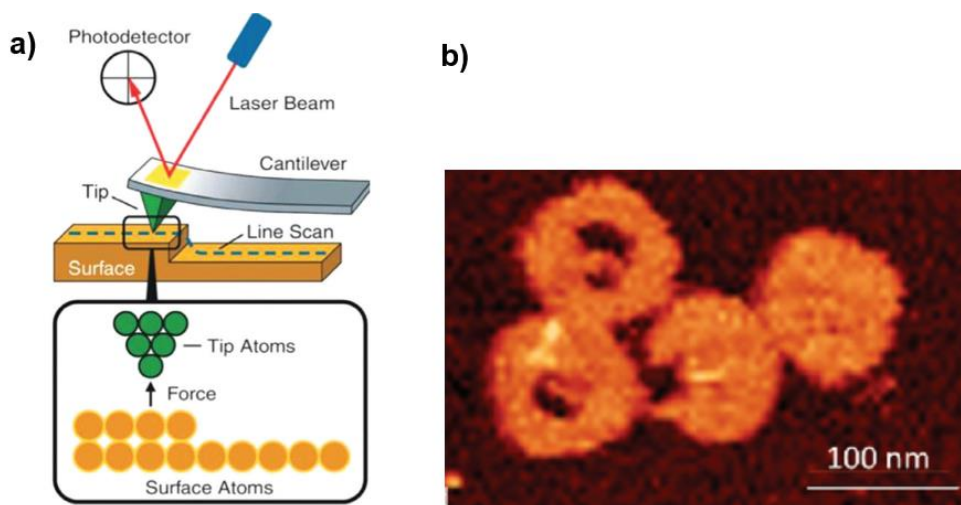


Figure 9: a) Schematic of AFM imaging setup.[15], b) AFM topographic image of DNA origami nanostructure in tapping mode. [9]

AFM is a versatile imaging technique with a simple and cost-effective setup. A representative image we can obtain from AFM is shown on the right of Figure 9b.

A specialized imaging technique in AFM that falls within tapping mode is the Quantitative Imaging (QI) mode. In this mode, it is possible to measure the mechanical properties of materials, such as stiffness, viscoelasticity, adhesion, and others. Additionally, it is a valuable method for imaging challenging materials, particularly soft and sticky ones, which are typically encountered in biological samples. This is because the QI mode is a force-curve based imaging method, in which the AFM tip approaches close to the sample surface and measures the interaction forces as the tip is approached or retracted. [16],[17] A typical force-distance curve is shown in Figure 10. During the QI mode imaging process, the cantilever approaches the sample surface, and the interaction forces between the surface and the tip are measured. As the cantilever approaches even closer, it eventually snaps into contact with the sample, and then it gradually starts retracting while the interaction forces increase. Finally, the tip returns to its original state as the z-distance increases, and the tip moves away from the sample surface.

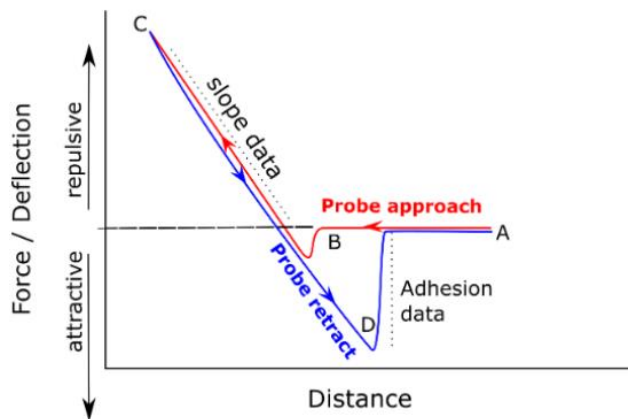


Figure 10: Schematic of the Force-Distance curve in AFM.[17]

AFM offers high spatial resolution of up to 1 nm, which is significantly better than optical microscopes. However, AFM suffers from low temporal resolution, as it may require several minutes to acquire an image. For this reason high speed AFM was developed, which can capture several frames per second. It uses a small cantilever with high resonance frequency and thus it allows for imaging in real time. This way, the temporal resolution problem is resolved. Finally, immobilization of the sample is required, as AFM is a scanning technique, which may damage the sample. [15]

2.2. Transmission Electron Microscopy (TEM)

Transmission Electron Microscopy (TEM) is a high-resolution imaging technique that uses a high energy electron beam to visualize the structure of materials and biological samples down to the atomic level. In this technique the electrons are produced from an electron gun and then accelerated to a voltage of 80-300 keV. [18] Then the electrons are focused into a beam after passing through a series of electromagnetic lenses and being directed towards the sample. During the interaction of the incident beam with the sample the amplitude and the phase of the electron wave change resulting in transmitted signals that are detected from the bottom side of the sample. TEM works under high vacuum conditions, so that the electrons do not collide with gas molecules inside the systems and decrease their energy. [18] A schematic representation of the setup is shown in Figure 11a).

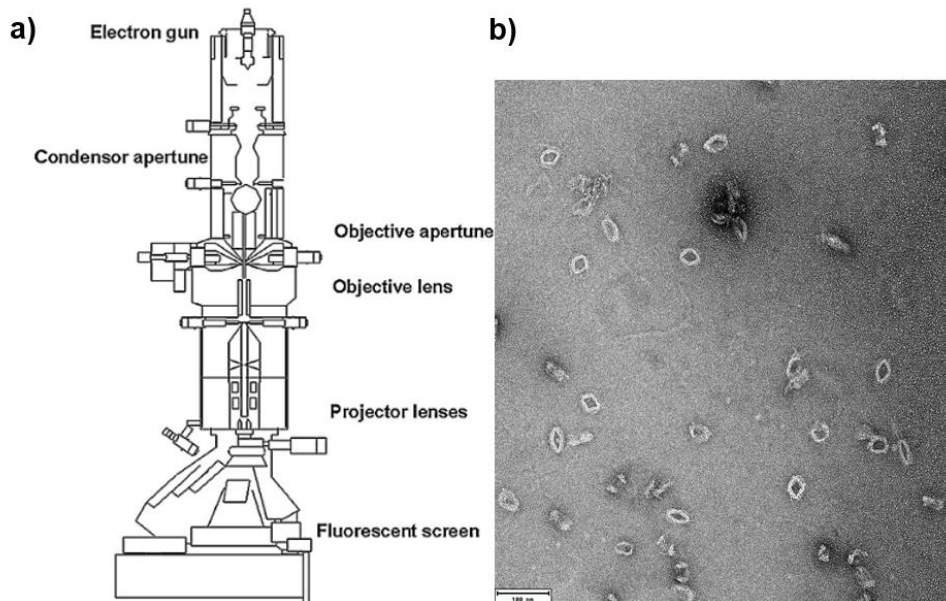


Figure 11: a) Schematic diagram of Transmission Electron Microscope [19], b) TEM data of our DNA origami nanopores open configuration.

TEM is a powerful tool in nanoimaging, providing high spatial resolution (approximately 0.2 nm) and detailed structural information about a material, making it useful in DNA nanotechnology. However, TEM has limitations, as it can only be used for very thin samples and may damage the sample due to bombardment with high energy electrons. Additionally, electron microscopes require conductive samples, or electrical charges will build up on the surface. Conventional TEM is conducted under vacuum and cannot provide information about the real environment of the sample. [15]

Cryo-TEM was developed as an alternative, where samples are frozen in liquid ethane to preserve their native structure, allowing for study under physiological conditions. However, this method is not ideal for studying the dynamics of DNA nanostructures as the sample is frozen, i.e static. Preparing and freezing multiple samples at different time steps is time-consuming and impractical. [15]

Liquid phase-TEM is an alternative approach where the sample is inserted in a thin liquid layer between two transparent windows made of silicon nitride (Si_3N_4). This method provides analysis of the material under physiological conditions but is limited by low contrast. The electron beam is scattered by the silicon nitride windows and the contrast is reduced due to the accumulation of charges on these surfaces. [20]

2.3. Fluorescence Microscopy

Fluorescence microscopy is a widely used technique for visualizing biological structures and processes with high spatial resolution. In this section, we will briefly introduce several different fluorescence microscopy techniques, including epifluorescence wide-field microscopy, confocal microscopy, total internal reflection fluorescence (TIRF) microscopy, and super-resolution techniques such as DNA PAINT (Point Accumulation for Imaging in Nanoscale

Topography). The main fluorescent microscopes are shown in Figure 12. Each of these techniques has its own strengths and limitations, and choosing the right technique depends on our project.

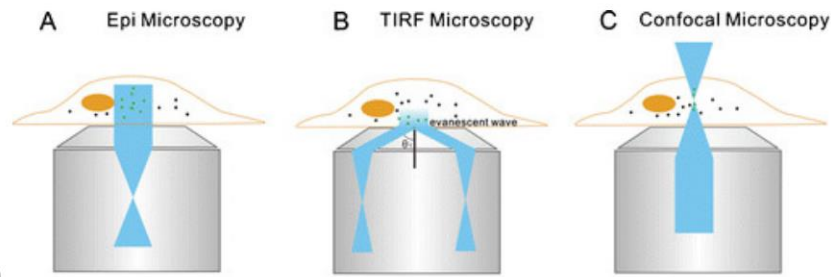


Figure 12: Illumination principles of A) Epifluorescent Microscopy, B) TIRF Microscopy and C) Confocal Microscopy [21]

2.3.1. Epifluorescence wide-field Microscopy

Fluorescence microscopy is a widely used and powerful technique in biotechnology for providing information about biological samples. In this technique, fluorescent dyes are used to label the molecules in the sample, which emit light at higher wavelengths when excited by the excitation light. This enables monitoring of the position and intensity of the molecules. As can be seen in the set up in Figure 13a), a dichroic mirror is used in order to reflect the excitation light to the objective and then to the sample and simultaneously transmit only the emitted light from the sample to the detector. The excitation filter (in blue) from the figure is used to narrow the wavelengths of the excitation light before it goes to the sample, while the emission filter in green color is used to block any other light coming from the excitation filter and let only the emitted light from the sample pass. With this method, the dynamics of the sample under its native conditions can be studied with high sensitivity, since changes in the sample's environment are easily detectable. The spatial resolution reaches down to 200 nm, as it is constrained by the optical diffraction limit. Additionally, the signal to noise ratio is not very high, as can be seen in Figure 13b), because the whole sample is illuminated at the same time. [15] Photobleaching is another important limitation of all fluorescent techniques, as the fluorophores fade when they are exposed to excitation light or high illumination power. This irreversible modification occurs when the fluorophore transits from the singlet to triplet state. When the fluorophore reacts with oxygen in this state, then it can become non-fluorescent. [22]

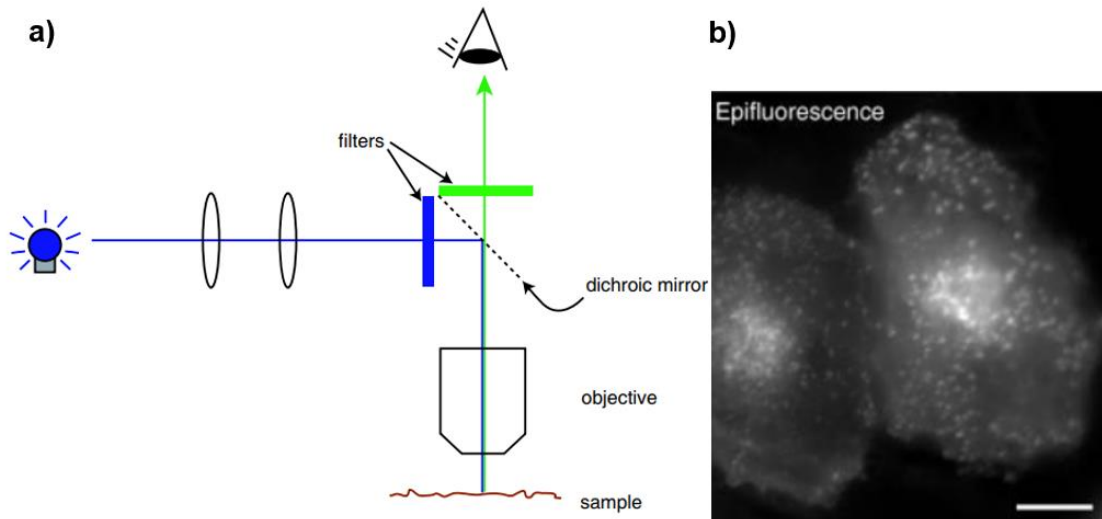


Figure 13: a) Basic principle of epifluorescence microscopy [19]., b) epifluorescent illumination for Imaging of HeLa cells. Scale bar is 10 μm . [23]

2.3.2. Confocal Microscopy

Confocal microscopy is a specific type of fluorescent microscopy that overcomes the problem of signal-to-noise ratio by illuminating a smaller volume of the sample. In this technique, a high-intensity laser is used to excite the fluorophores. The setup of a confocal microscope is similar to that of a fluorescent microscope, as shown in Figure 14a). However, the light is focused through the objective lens onto a small spot with a diameter of approximately 0.5 μm . A pinhole is used in confocal microscopy to block out-of-focus light from excited fluorophores, resulting in a high-contrast image that eliminates background light. The confocal light is detected by a sensitive light detector on the other side of the pinhole. Compared to conventional fluorescent microscopy, confocal microscopy offers greater sensitivity and image detail, as can be understood from Figure 14b). The technique can penetrate up to 200 μm in depth, making it suitable for studying the 3D structure of samples. However, confocal microscopy equipment is expensive, and the high-intensity laser used can lead to photobleaching of the fluorophores. The lateral resolution is limited to 200-300 nm by the diffraction limit, as with other light microscopes. [15],[24]

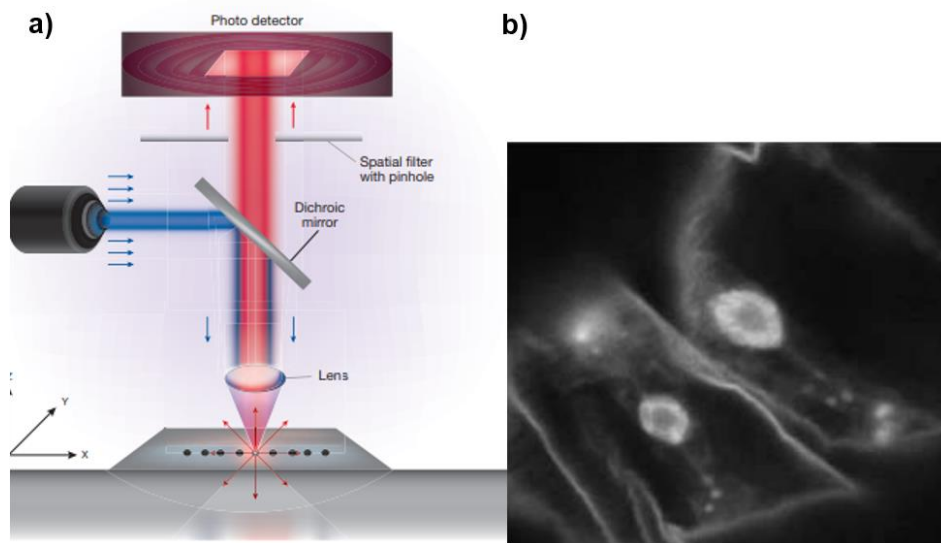


Figure 14: a) Representation of Confocal Microscope [21], b) Image of cells of spirogyra [22]

2.3.3. Total Internal Reflection Fluorescence (TIRF) Microscopy

Total Internal Reflection Fluorescence (TIRF) microscopy is also a specific type of fluorescence microscopy and a powerful optical technique that excites fluorophores in a very thin axial region. The principle of this method is based on total internal reflection, which occurs when the incident light is reflected at the interface of two media with different refractive indices, such as a solid coverglass and a liquid sample. In TIRF microscopy, the solid medium has a refractive index similar to that of glass ($n=1.51$), while the liquid medium has a refractive index similar to that of water ($n=1.33$). At the interface of the two media, an electromagnetic evanescent field is generated that has the same frequency as the incident illumination. The intensity of this field decays rapidly after 100-200 nanometers away from the surface, enabling the excitation of fluorophores only on the surface of the sample. This feature provides a high signal-to-noise ratio, as only the fluorescent signal from the surface is detected. The experimental setup is similar to that of epifluorescence widefield microscope, except for the way that the sample is illuminated and how the emitted light is collected. The excitation light is directed to the sample with a very big angle so that total internal reflection is achieved, while the emitted light that is gathered to the objective lens is only the fluorescence light generated from the evanescent electromagnetic field.

Figure 15a) illustrates, how the evanescent field is generated and 15b) the data of the same sample as in Figure 13, but using TIRF illumination here. Comparing the data images between Figure 13b) and 15b) it is clear that TIRF microscopy offers higher contrast and resolution. TIRF is commonly used in biophysics, biology, and nanotechnology, with the sample usually placed in an aqueous environment very close to the transparent solid. [25] The spatial resolution of TIRF microscopy depends on the wavelength of the illumination used, typically around 100 nm, while its temporal resolution is very high, allowing real-time capture of sample dynamics. [26]

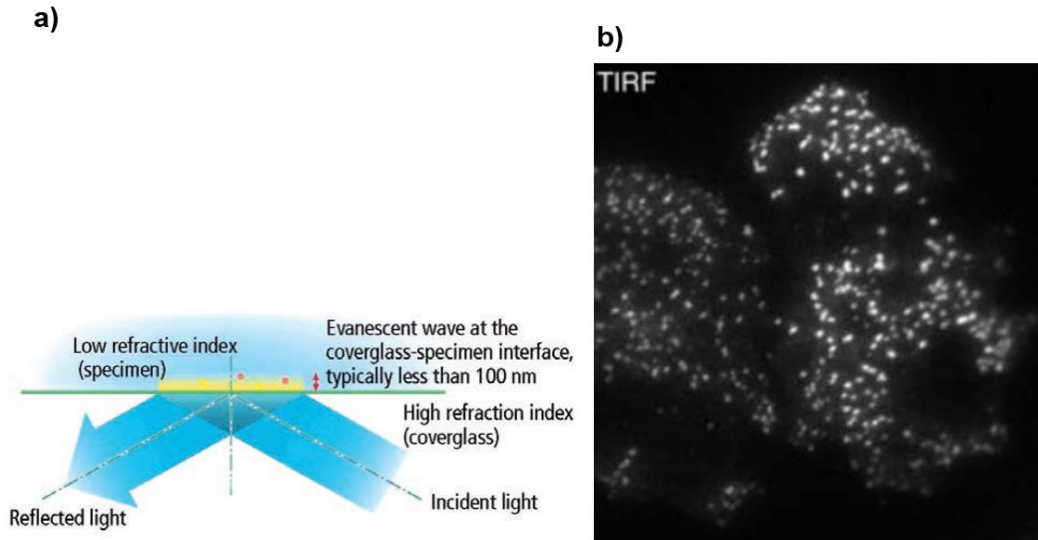


Figure 15: a) Generation of evanescent electromagnetic field in TIRF microscopy [27], b) TIRF illumination for Imaging of HeLa cells. [23]

As mentioned above, TIRF requires total internal reflection of the incident beam at the interface of the two media, in which the propagating beam comes into contact with the boundary to the medium that has a lower refractive index. This happens only at and above a specific incident angle that is called critical angle θ_c , which can be obtained from Snell's law as shown in equation 1.1. In this equation n_1 is the refractive index for the transparent solid and n_2 is the refractive index of the liquid medium, while θ_1 is the angle of the incident beam with respect to the normal to the interface and θ_2 is the angle of the refracted beam with the liquid medium. The amount of light being reflected increases, as the incident angle also increases, while the refracted beam decreases in intensity. The critical angle for internal reflection is given by equation 1.2, and it occurs from equation 1.1 in the case of the refraction angle θ_2 is equal to 90 degrees, meaning that $\sin\theta_2=1$. [27]

$$n_1 \sin\theta_1 = n_2 \sin\theta_2 \quad (1.1)$$

$$\theta_c = \sin^{-1}\left(\frac{n_2}{n_1}\right) \quad (1.2)$$

The intensity of the evanescent field that decreases exponentially as the depth in the sample increases is represented by equation 1.3, where I_z is the intensity at a depth z , I_0 the intensity at the interface, d the penetration depth, which is dependent on the wavelength of the incident illumination.

$$I_z = I_0 e^{-\frac{z}{d}} \quad (1.3)$$

In Figure 16 it is possible to see the geometry for the incident angle at the interface and also the evanescent field created in the second medium.

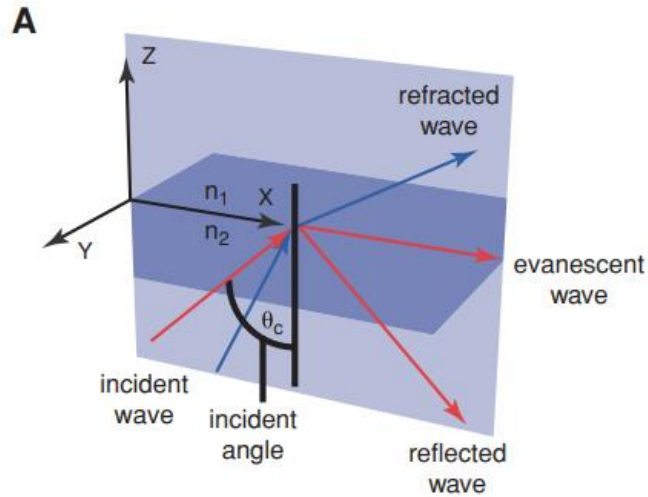


Figure 16: Representation of the incident and refracted beam on the interface between the two media. [25]

2.3.4. Super Resolution Microscopy

Super resolution microscopy techniques have developed in order to enhance the spatial resolution and are mostly used for the visualization of biological structures with a higher resolution that reaches beyond the diffraction limit from the objective lenses in light microscopy. It is important to explore the super resolution microscopy techniques, as in this project we need to image at the nanoscale, as our DNA nanoactuators have a size of 30nm.

In the world of optical microscopy, the diffraction limit is an inherent boundary that constrains the level of detail we can capture in our observations. This fundamental limitation arises from the wave nature of light itself. When light encounters an obstacle, such as the aperture of a microscope objective or tiny structures within a specimen, it exhibits a characteristic behavior known as diffraction. This phenomenon causes light to spread out, preventing us from detecting the exact location of a point source with unlimited precision. As a result, we face difficulties in distinguishing fine details. Ernst Abbe's equation encapsulates this limitation and is shown in equation (1.4) below, where d is the diffraction limit, λ the wavelength of the incident light and NA is the Numerical Aperture of the objective lens, which is given by equation (1.5). The angle θ is the angular aperture that is shown in Figure 17.

$$d = \frac{\lambda}{2 \cdot NA} \quad (1.4)$$

$$NA = n \sin \theta \quad (1.5)$$

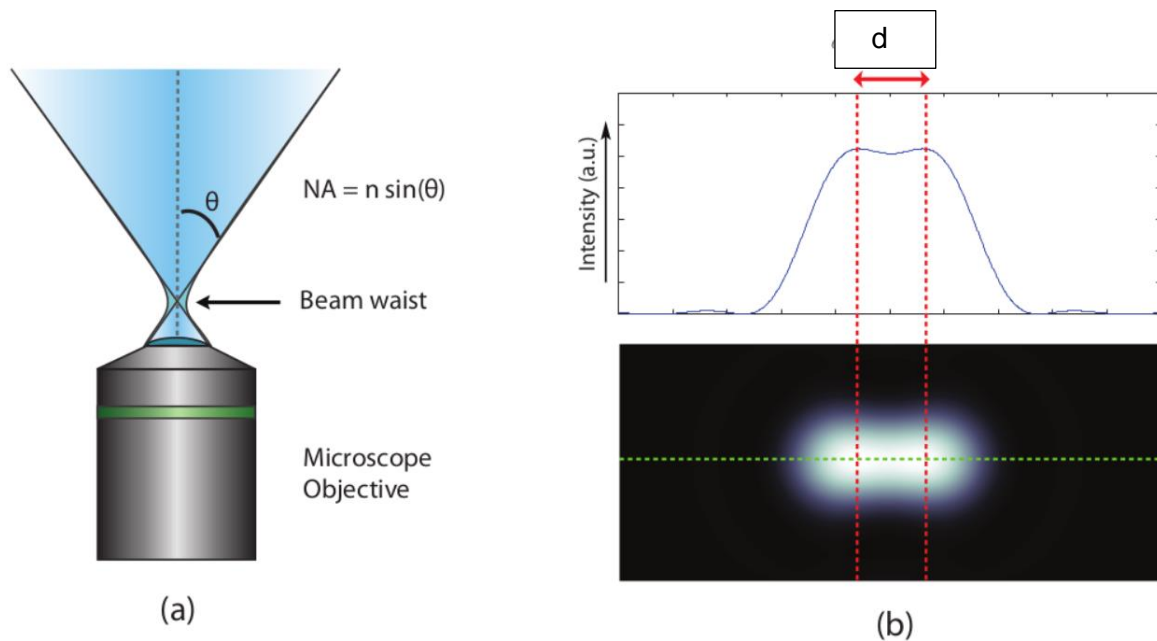


Figure 17: a) Representation of the NA from objective lens, b) the intensity of two points that have been under the effect of diffraction under the microscope and the smallest resolvable distance is 'd'. [28]

The smaller 'd' is, the higher the resolution, but this is limited by both the wavelength of light used and the numerical aperture, the latter being a measure of the lens's ability to capture light. However, real-world microscopes face additional challenges. Optical aberrations, like spherical and chromatic aberrations, come into play, causing distortions in the image. These aberrations mean that the practical diffraction limit in real microscopes is not solely defined by the diffraction of light. These optical imperfections introduce complexity and affect the quality of images. [28],[29]

The sparse distribution of illumination in super resolution imaging allows for the visualization of smaller structures that are not resolvable with conventional light microscopy. Sparse distribution of illumination is achieved by letting only a small subset of fluorophores to get detected at a certain time, resulting in a super resolution image that contains the emitting light from a part of the sample that got collected in different moments. Super resolution imaging techniques use a variety of approaches to achieve sub-diffraction resolution that will be explained below. [30]

2.3.4.1. SIM/STED/PALM/STORM

Structured Illumination Microscopy (SIM) is an advanced imaging technique that allows imaging of samples beyond the diffraction limit. It uses a grid pattern that consists of a series of phase-shifted patterns to illuminate the sample. The resulting patterned illumination creates Moire patterns that interact with the sample, allowing for the extraction of high-frequency information. The sample acts as a grating that reflects the light, creating diffraction orders. When the light interacts with the sample, the interference of the Moire pattern and the sample creates a high-frequency information that can be detected by the microscope. By taking multiple frames at different phases of the illumination pattern, the high-frequency information from different patterns can be combined to create a super-resolved image that reveals details beyond the diffraction limit. The lateral resolution reached up to 50 nm. [31]

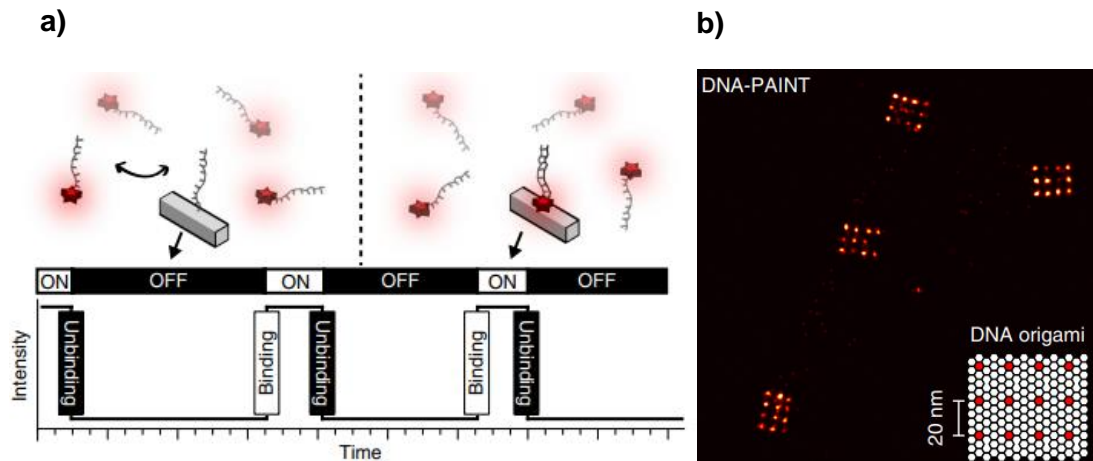
Stimulated Emission Depletion (STED) microscopy uses two laser beams in order to illuminate the sample. The excitation beam, which excites the fluorophores in a small region of the sample and then a high intensity depletion beam, which has donut shape. This means that there is a dark spot in the center. The outer region outside of the spot causes the fluorophores to return to their ground state, so that the only fluorophores emitting photons are only the ones in a small spot in the center. By repeating this procedure many times at different points of the sample we can obtain a super resolution image with spatial resolution between 30-80 nm. [31]

PhotoActivated Localization Microscopy (PALM) uses a low intensity laser to excite a small part of the sample. The molecules emitting light are imaged and localized by using Gaussian fitting. By completing many cycles of the same process we have the result of a super resolution image that provides information about the position of the molecules having a lateral resolution of 10-20 nm. [31]

Stochastic Optical Reconstruction Microscopy (STORM) uses a low intensity laser for exciting the fluorophores in the sample, but then a higher intensity laser is used to stochastically deactivate the fluorophores. This results in having only certain fluorophores emitting fluorescent light that can finally cause an image beyond the diffraction limit. [31]

2.3.4.2. DNA PAINT (Point Accumulation for Imaging in Nanoscale Topography)

DNA PAINT uses short stranded strands of approximately 8-10 nucleotides long in order to image the sample. Firstly, a set of docking strands is fixed onto the surface of the sample. Then an imaging solution containing fluorescently-labeled imager strands is then introduced to the sample. The imager strands hybridize to the docking strands, resulting in transient blinking events that can be visualized using a fluorescence microscope. This process is illustrated in Figure 18a). By analyzing the position of each blink, the precise location of the target molecule can be determined with high accuracy, achieving spatial resolutions of at least 10 nm. The process is repeated many times, so that we can obtain a super resolution image, as shown on the right of Figure 18b). In each cycle, a washing solution is introduced to remove any unbound imager strands, and a new imager solution is then added to the sample to replenish the fluorophore-labeled strands. This renewal of imager strands in each cycle helps to reduce photobleaching. This technique is able to study the dynamics and conformational changes in real time, depending on the hybridization time for the opening and closing of the nanopore, while it also provides multiplexing capability. The latter holds, since the strength of fluorescent signals is dependent on the length and sequence of the strands being used for the probing. However, DNA PAINT is a slow technique, since hybridization takes several minutes to happen, thus the temporal resolution of this technique is low. [30]



2.3.4.3. Forster Resonance Energy Transfer (FRET)

Forster Resonance Energy Transfer (FRET) is a process that involves labeling two molecules with suitable fluorophores. The molecules are known as the donor and acceptor. When the donor and acceptor molecules are in close proximity (typically within 2-8 nm), energy is transferred from the excited donor molecule to the acceptor molecule. This energy transfer is non-radiative and causes the acceptor molecule to become excited and emit fluorescent light. The energy transfer occurs due to dipole-dipole interactions between the two molecules, and is distance and orientation dependent. This means that the efficiency of energy transfer is influenced by the distance and relative orientation of the donor and acceptor molecules. FRET is not ideal for studying the structure of a sample, but it can provide valuable information about the dynamics of biological samples in real time and under physiological conditions. For example, FRET can be used to study protein-protein interactions or conformational changes in proteins. It is worth noting that FRET is sensitive to the local environment of the fluorophores, such as pH and temperature, which can affect the efficiency of energy transfer. A simplified illustration of FRET is shown in Figure 19. [15],[32]

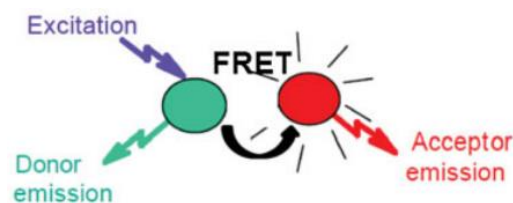


Figure 19: FRET technique [32]

3. Research Question and Objectives

How can we detect the nanomechanical state of a DNA origami nanoactuator?

To answer this question we divide the project into three objectives:

Objective 1: Identifying the optimal way of imaging the state (open/closed) of DNA nanoactuators.

Objective 2: Finding how reliable/robust are the states and what is the nanomechanical state of the closing and opening of the nanoactuators.

Objective 3: Investigate how do the environmental factors affect the nanomechanical state of the DNA nanoactuators.

For the characterization of DNA origami nanopores we need to select the most efficient method that gives reliable information about the mechanical state in real time and good quality images. The comparison between the different microscopes and the techniques are shown in Table 1, 2 and 3. Because of its high spatial resolution, DNA PAINT provides precise localization of the molecules and once the docking strands are fixed on the sample surface, is a very simple technique to use. In addition to that, photobleaching does not constitute a big problem, since the process of DNA PAINT technique includes the introduction of new imaging solutions in each cycle.

In DNA PAINT, the imager strands carry a dye and they are non-fluorogenic, which means that they do not emit on their own, unless they bind to a certain molecule. The nature of this bond is hybridization and the imager strands stay there for an extended time before they unbind. Therefore, there is an accumulation of fluorescent emission from that specific area (the “blinking”), which is detectable. However, the imager strands can also bind non-specifically to some molecules in the sample, producing fluorescent background light, which can decrease the signal-to-noise ratio. Combining DNA PAINT with a suitable microscope can help address this issue. Conventional fluorescent microscopy is not ideal, because the whole sample is illuminated at a specific moment, so emission of light comes from every point of the sample. Confocal microscopy uses a laser that is focused on the objective lens of the microscope and forms a spot with a diameter of approximately 0.5 μm . Its field of view is usually around a few hundred micrometers, which makes it able to analyze many nanopores each time and provide abundant statistical evidence. The depth of penetration is about 200 μm . This means that confocal is also not capable of providing us with a high signal to noise ratio, as there will be excitement of fluorophores throughout the whole volume of the sample. Additionally, it can lead to more photobleaching, as the intensity of the laser beam is higher, since it is focused on one point. In contrast, TIRF microscopy is considered to be more suitable, because it produces an evanescent electromagnetic field in the solid-liquid interface that decays after 100 nm away from the surface. This means that there will be fluorescent signals generated mostly on the surface, which increases the contrast.

| Microscopes | | | | |
|---------------|--|--|--|--|
| | Transmission Electron Microscopy (TEM) | | | Atomic Force Microscopy (AFM) |
| | Conventional TEM | Cryo-TEM | Liquid-Phase TEM | |
| Advantages | <ul style="list-style-type: none"> -High spatial resolution (~0.2 nm) -Detailed structural information -High sensitivity | <ul style="list-style-type: none"> -Preserves native structure of the sample -High resolution | <ul style="list-style-type: none"> -Imaging under physiological conditions -Able to study the conformational changes | <ul style="list-style-type: none"> -Very high spatial resolution (~1 nm) -Able to study biological samples under physiological conditions in real time |
| Disadvantages | <ul style="list-style-type: none"> -Under vacuum -Thin samples (<100 nm) -Destructive technique -Not real environment sample information -Requires conductive sample | <ul style="list-style-type: none"> -Time consuming for the dynamics -Cannot capture conformational changes | <ul style="list-style-type: none"> -Requires the design and creation of the cell -Scattering of the electron beam from the membranes and liquid solvents | <ul style="list-style-type: none"> - Challenging sample preparation: Immobilization -Only topology of the sample -Interaction between tip and soft tissue may damage the sample |

Table 1: Advantages and disadvantages of TEM and AFM characterization techniques. The advantages are shown in blue color, while the disadvantages in yellow.

| Fluorescent Microscopes | | | |
|-------------------------|---|--|---|
| | Conventional Fluorescence Microscopy | TIRF | Confocal Microscopy |
| Advantages | <ul style="list-style-type: none"> -Simple setting -Inexpensive equipment -High sensitivity -Dynamics in real time | <ul style="list-style-type: none"> - High temporal resolution -High signal-to-noise ratio (contrast) → -Evanescent electromagnetic field decays after 100 nm -Studying the dynamics in real time | <ul style="list-style-type: none"> -Obtaining 3D detailed images -High temporal resolution -Large field of view (few hundred μm) |
| Disadvantages | <ul style="list-style-type: none"> -Photobleaching -Limited spatial resolution (200-300 nm) -Limited signal to noise ratio -Phototoxicity | <ul style="list-style-type: none"> -Limited spatial resolution (~100 nm) -Photobleaching | <ul style="list-style-type: none"> -Limited lateral resolution (200-300 nm) -Photobleaching -Not very high signal to noise ratio -High cost equipment |

Table 2: Advantages and disadvantages of fluorescent microscopes. The advantages are shown in blue color, while the disadvantages in yellow.

| Super Resolution Microscopy Techniques | | | |
|--|--|---|--|
| | SIM/STED/PALM/STORM | FRET | DNA PAINT |
| Advantages | -Image resolution beyond the diffraction limit→sparse distribution fashion | -Can study the dynamics in real time -High sensitivity -Studies the sample under physiological conditions | -Eliminated photobleaching effect -High spatial resolution (<10nm) -Precision in localization of molecules (high specificity) -Able to study the dynamics -Multiplexing capability |
| Disadvantages | -Photobleaching -Very specialized equipment | -Signal only in close proximity (2-8 nm) -Careful choice of fluorophores (spectral overlap) -Signal depends on orientation and local environment of fluorophores -Photobleaching -Not information about structure | -Expertise in sample preparation (designing the probes) -Low temporal resolution -Signal to noise ratio depends on the concentration of imager strands |

Table 3: Advantages and disadvantages of Super Resolution Microscopy techniques. The advantages are shown in blue color, while the disadvantages in yellow.

4. Methods

4.1 Design of the nanopores

For this project, we will employ the DNA nanopores that have already been designed by our project team, which bear resemblance to the rhombus-shaped nanoactuators that have been previously reported in the literature. As illustrated in Figure 20, the nanopores in our study have a rhombus shape and are composed of four arms. The nanopores are programmed to have a height of 18 nm. Locking strands are positioned at the top and bottom corners of the nanopores, which are responsible for maintaining their closed conformation. When triggering strands are inserted in the system the conformation can change from close to open and vice versa. It should be noted that the mechanism of the conformational change is based on the hybridization between complementary strands, which facilitates the formation of stable duplexes between the locking and triggering strands, leading to a cooperative response.

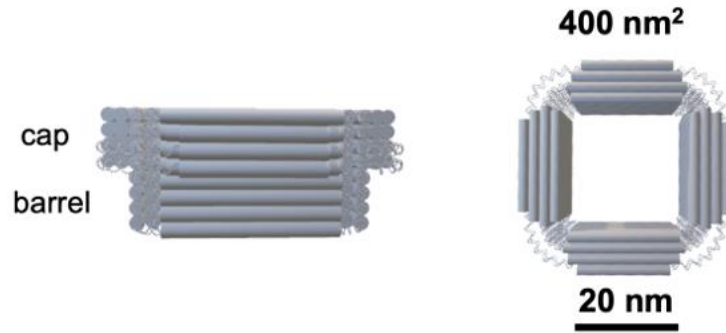


Figure 20: Designed rhombus-shaped nanopores by our project team.

Designing appropriate probes to image the structure's state (open/closed) before and after nanomotion is central to answering our scientific question. In DNA PAINT technique we need to make sure that the location of the docking strands on the sample surface and the type of probes is suitable in order to provide such information. As can be seen in Figure 21, the docking strands will be placed at each corner of the nanopore, so that the imager strands can hybridize in these positions and provide precision in the location of the molecules. This allows for DNA PAINT images from which we can measure the angles and be able to find the angle distribution. Moreover, the probes need to have certain properties that allow for the transient blinking during imaging. This means that the hybridization should not be very strong, thus the structure should not be very stable. DNA structures stability are affected by several parameters like pH, temperature, strand length, cation concentration during the assembly (Mg^{2+}) and C-G concentration. More specifically, the imager strands should have shorter length than the docking strands, which enables them to hybridize for shorter time periods. In addition to that, since it is already known that C-G pairing is more stable than A-T, we should use a low C-G content. This happens because C-G pairing happens with more hydrogen bonds, compared to A-T pairing. [33]

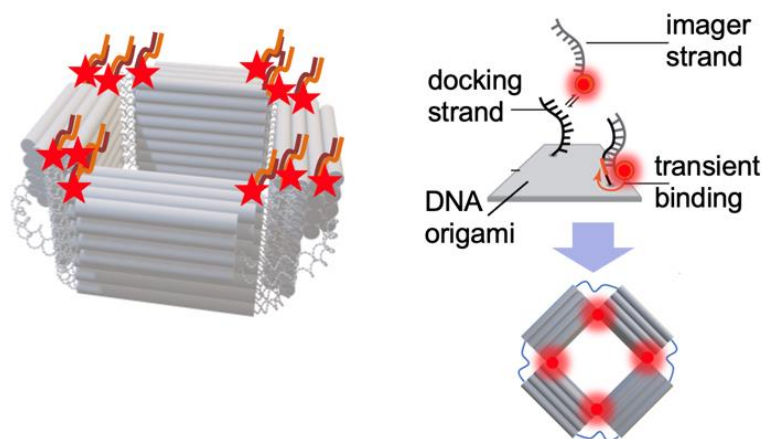


Figure 21: Design of the docking strands in the surface of DNA nanopore and the imaging strands blinking after hybridization.

4.2. Assembly of DNA origami nanopores

For achieving the above described DNA nanopores we need to follow a specific procedure. We pipette all the materials necessary for the staple mixture in one eppendorf tube. In one eppendorf tube we mix 80 μL of DNA scaffold 100 nM, 160 μL of DNA staple strand mixture 250 nM, 80 μL of TAE Tris-Acetate-EDTA with pH=8.3, 120 μL of MgCl_2 x10 and 360 μL of H_2O . The DNA staple strands are complementary to the DNA scaffold, so that hybridization is able to take place. The MgCl_2 solution is necessary, as it contains Mg^{2+} ions, which provide stability in the structure. Mg^{2+} ions get attached to the phosphate groups in the backbone of the DNA and neutralizes the electrostatic repulsion between the negatively charged groups, thus the DNA origami is less likely to dissociate. The final solution undergoes a thermal cycle for 48 hours. The annealing during the thermal cycle is important, as it ensures that the staple strands hybridize in the correct positions and we get the desirable structure with high stability and yield. [12]

4.3. Purification of DNA origami nanopores

Purification of the assembled DNA origami nanopores is necessary for removing the remaining solution with the staple strands that do not contribute to the system, because they did not get attached to the DNA structure. The main principle is that the filter used for the purification is able to keep the larger structures.

First we pipette 500 μL of the 10nM DNA origami to a 0.5 mL filter, which is placed inside an eppendorf tube, and then we place it to the centrifuge machine, operating under 4000 RCF (Relative Centrifugal Force) for 3 minutes. After the centrifuge is done, we take the filter out of the eppendorf tube and throw the remaining solution in the tube away. Consequently, we add the remaining 300 μL of DNA origami solution from the assembly to the filter and fill with 100 μL of buffer solution that contains 1xTAE and 15mM Mg, in order to fill the whole volume of the filter, and put it in the centrifuge machine. Once this is finished and the remaining solution inside the eppendorf tube is thrown away, we fill the filter with 400 μL and repeat the same procedure 3 more times. The final solution with DNA origami will have a concentration of 56nM.

4.4. Gel electrophoresis

Gel electrophoresis is a technique that is used to analyze and separate charged molecules in an electric field, like DNA, RNA or proteins. This technique can give information about the different sizes or shapes and charge of the molecules. We specifically prepare agarose gel in our experiment. Agarose gel is a network of connected molecules that form a gel-like structure, which is a porous environment that allows the charged molecules to migrate in the presence of an electric field. Smaller molecules can move faster and reach further at the gel, while larger molecules move slower through the porous of the gel, so we can distinguish them in bright bands existing more upwards than the ones belonging to the smaller molecules. [34]

For preparing the gel we put 0.45g of agarose powder together with 42.5 mL of running buffer, inside a beaker, then place it in a microwave oven and let it heat for 1 minute. The running

buffer contains 25 mL of 10xTBE (Tris-Boris-EDTA), 2.5mL of $MgCl_2$ solution and 472.5mL of de-ionized H_2O . We take out the beaker to steer for a while and place it for further 30 seconds in the microwave. After this, we throw 2.5 μ L of a stain dye and then put the solution to the gel tray containing the sample comb. We cover the whole tray with aluminum foil and leave it for 30 minutes till the gel solution solidifies. When the required time for the solidification has passed we take the gel and place it in the chamber, while filling it with the running buffer solution till the gel surface is covered. The chamber is located inside a white basket, which we have to fill with water and put two ice boxes in the water. We carefully take the comb out and load 1.5 μ L of the solution with the base pairs in the first sample well, 5 μ L of DNA scaffold 10nM in the second well and finally 8 μ L of the mixture that includes 6 μ L diluted DNA origami and 2 μ L of loading buffer, in the third well. Diluted DNA origami is made by mixing 1.07 μ L of DNA origami 56nM + 4.9 μ L of 1xTAE solution with 15mM Mg. Eventually we close the chamber with the two electrodes and turn on its power. We need a Voltage of 90 Volt, a current of 400mA and we leave it for 90 minutes before we come back and obtain the final image with the camera equipment. [34] An example of how the gel electrophoresis process looks like is shown in Figure 22. We can see that the power supply creates a cathode at the top part of the chamber, while an anode at the bottom part of it. This will make the DNA nanopores to migrate within the gel towards the positive terminal. In the first well we place base pairs of DNA, at the second one we place DNA scaffold, while at the third we place the DNA nanopores. After the 90 minutes has passed we can see how far our DNA nanostructures have reached within the third well, and according to the bands at the two first wells we can get an estimate about the size of the nanopores. This happens because the two first wells are used as a reference and we already know how many nucleotides are in those bands. The longer bands tend to migrate slower, while the shorter ones move faster and they reach further within the gel.

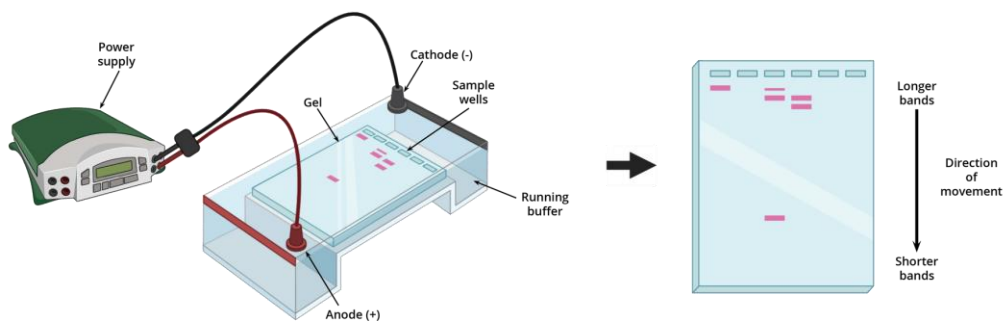


Figure 22: Schematic of the gel electrophoresis process and an example of how the result should look like.[35]

4.5. Sample preparation and imaging for TIRF

-Sealed Flow Cell

The two main materials needed for the chamber are a microscopy slide and a coverglass. Firstly, it is necessary to clean the materials used for the chamber. This is executed by placing them in beakers of acetone and then isopropanol sonicating them for 1 minute. Following that,

we conduct oxygen plasma cleaning for 10 minutes. An oxygen plasma is an ionized gas that contains charged oxygen ions and/or electrons, and it carries internal energy. It flows inside a chamber at low pressure, in which the target material are placed.[36] When the plasma interacts with the surface of a material some properties may change like surface roughness or hardness and hydrophilicity. In this project oxygen plasma is used for creating higher hydrophilicity on the glass surface. More specifically, when the oxygen plasma interacts with the glass surface the oxygen collides with it, transferring energy to the chemical groups existing onto the surface, like (Si-OH) groups, creating hydroxyl (OH^-) groups, like shown in Figure 23. These groups are polar, which make them attracted to water molecules, which are also polar. This means that the water or other types of polar molecules tend to spread more easily upon the surface, thus hydrophilicity has been achieved. In this way, the solutions for the sample preparation are more efficiently deposited inside the sample chamber. [37],[38]

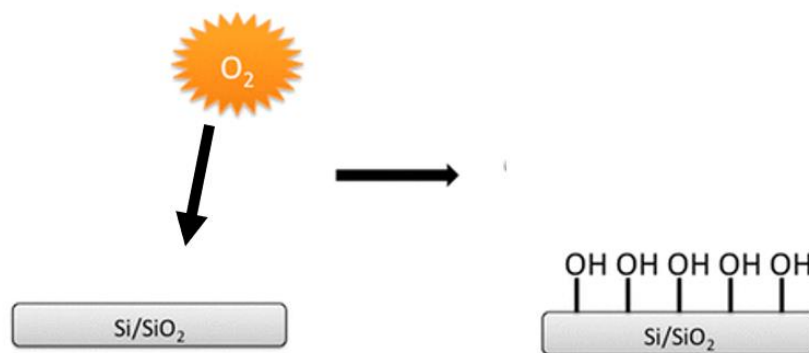


Figure 23: Schematic representation of silica surface functionalization after oxygen plasma cleaning.[39]

After cleaning, we place two pieces of parafilm as spacer, which we prepare by folding it into stripes, on top of the microscopy slide, such that they are parallel to each other and keep a small (~1-2 cm) distance between them. Then we place the coverglass on top and heat the stack on a hotplate, at 150° C degrees until the parafilm melts (~1 minute) and becomes adhesive from both sides, such that a leak tight chamber is formed.

Once the glass substrates are cleaned and the chamber is formed, we pipette inside 100 μ L of 0.0001% polylysine and let it incubate for 10 minutes. Polylysine is a positively charged polymer and is important in order to ensure that the DNA nanopores will stay immobilized on the substrate. The backbone of DNA is negatively charged due to phosphate groups being exposed on the outer side of the DNA, thus the DNA nanopores will get attached due to electrostatic forces. with the polylysine. [40] Then we rinse with 200 μ L of H_2O three times, in order to remove the unbound polylysine. Following that, we pipette 100 μ L of DNA origami at a concentration of 1 nM inside the chamber and let it incubate for another 5 to 10 minutes. The reason we use diluted DNA origami of 1 nM is because DNA tends to aggregate and we want the structures to be isolated and well distributed for clear visualization and sufficient statistics. After incubation we rinse the chamber with 200 μ L of Buffer B+ solution (5mM TAE, 10mM MgCl₂, 1mM EDTA) three times. Finally, we pipette 100 μ L of imaging solution (which contains Buffer B+ solution and 10 nM of ATTO 647N fluorophores) and seal the chamber with tape from both sides, so that there is no leakage. A demonstration of the profile of the chamber is shown in Figure 24.

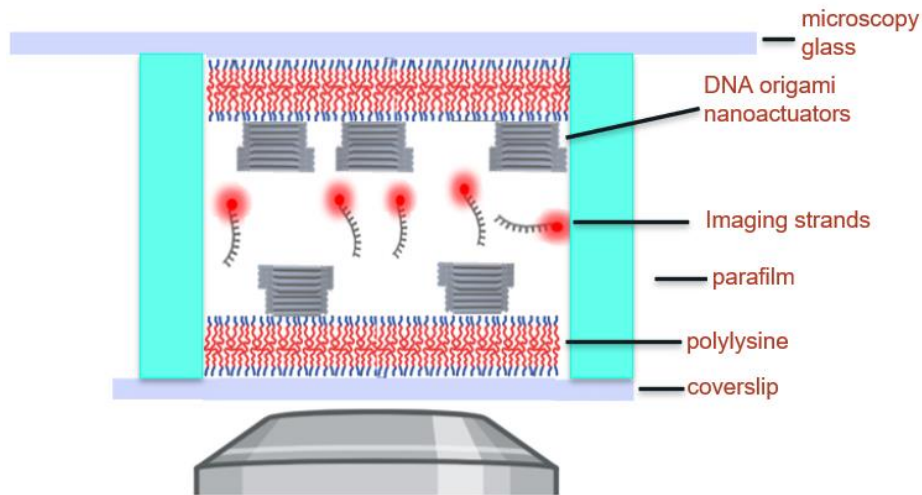


Figure 24: Schematic drawing of sealed flow chamber for TIRF experiments.

-Non-sealed flow cell

For the non-sealed chamber two coverslips are needed. The cleaning procedure is the same as described for the sealed chamber above, by using sonication with acetone and isopropanol and finally oxygen plasma. After the cleaning we deposit 50 μ L of polylysine at the centre of one of the coverslips and then immediately put the second one on top in order to be in contact with the first one, so that the polylysine spreads at the second coverslip as well. The direction in which we position the second one, is orthogonal with respect to the first one, like a cross shape is formed with the two coverslips. This direction is chosen, so that the most central part of the second coverslip is covered with polylysine too, in case we want to prepare two samples at the same time. Once the contact has been achieved and the coverslips are separated, we leave them for 10 minutes for incubation. The washing part with de-ionized H_2O follows, and then the deposition of 50 μ L DNA origami nanopores with 5 minutes of incubation time. Final step is to wash away the remaining DNA nanopores from the chamber with 200 μ L of Buffer B+ solution and introduce 50 μ L of imaging solution. The schematic drawing of how the non-sealed chamber looks is shown in Figure 25.

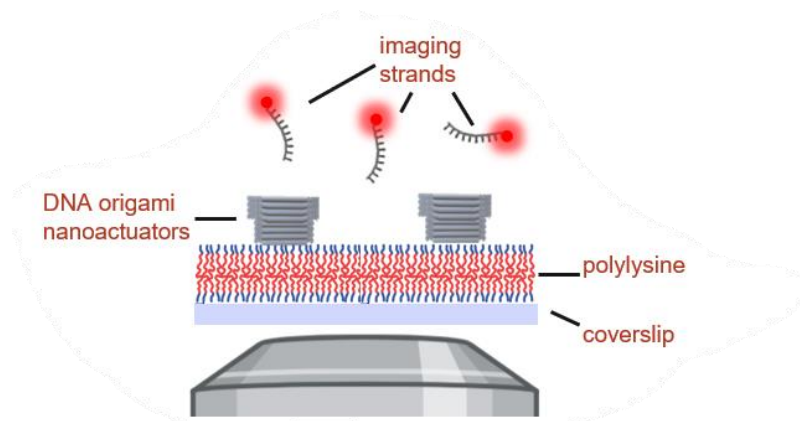


Figure 25: Schematic drawing of non-sealed flow cell.

The fluorophore selection is crucial for the quality of the imaging experiments, as some fluorophores may be more prone to photobleaching than others, leading to reduced signal intensity and shorter imaging times. The TIRF microscope that we will use has an incident laser wavelength of 642 nm, thus we need a specific fluorophore that absorbs in this specific wavelength. ATTO 647N is a suitable fluorophore for our experiments. As shown in Figure 26 the spectra of the fluorophore shows that there is absorption at 645 nm, while emission occurs at 680 nm. Furthermore, ATTO 647N has very high thermal and photochemical stability, which are essential properties to achieve high-quality imaging results and reliable experimental outcomes. [41]

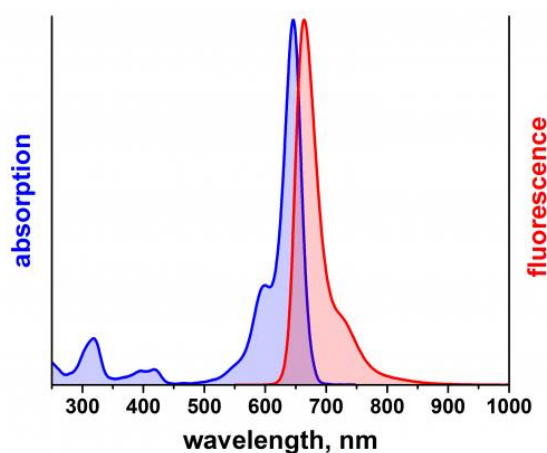


Figure 26: Spectra of ATTO 647N fluorophore. [41]

Imaging in TIRF microscopy was conducted by using the red filter which gives a wavelength in red color of 642nm. Before placing the sample at the stage we need to put a droplet of water on the objective lens, as water will behave as the second medium for the total internal reflection of the incident beam. The objective lens is 60x magnification, while the pixel size of the instrument camera is 0.11 μ m. Most of the experiments were carried out in 30mW of laser power, 100ms of exposure time, 1s of waiting time and 2 minutes of total duration for the capture of one image, which are parameters of Nikon software that can be manually changed while the experiment is conducted. Exposure time is the time in which the sample is exposed to light for the acquisition of one frame, while waiting time is the one between two sequential frames. Duration time is the time needed to capture one super resolved image, which is equal to 121 frames for all our experiments. However, the software parameters are varied during some experiments, but when this happens the values are mentioned in the results section of this report.

4.6. Atomic Force Microscopy (AFM)

We prepare the sample for AFM imaging by attaching a mica substrate on top of a microscopy slide. We first cut a piece of tape and place it on top of the mica substrate in order to take the top layer off, so that we start with a freshly cleaved and clean one for the new experiment. We

draw a circle in the center of the mica substrate, so that we have marked the exact area in which the liquid solutions will be deposited. Then we pipette 4 μL of 0.001% polylysine at the center of the circle, let it incubate for 3 minutes and then rinse with 200 μL of H_2O three times. Polylysine is used here for the same reason as in the sample preparation of TIRF microscope, i.e. to attract the negatively charged DNA nanopores towards the substrate. After that we pipette 4 μL of diluted solution DNA origami 2 nM on the circle and let it incubate for 1 minute before we rinse with 200 μL of Buffer B+ solution three times.

For imaging the DNA nanopores with AFM the SCANASYST-AIR-HR tip was used, which has a spring constant of 0.4 N/m. [42] This value is considered to be among the lowest values that cantilever spring constants can have, and are thus used mostly in soft, biological samples. [43] The scanning mode that we used is the Quantitative Imaging (QI) mode, which can provide accurate quantitative measurements for the material's properties. The experiments were conducted in liquid with buffer solution that contains Mg^{2+} ions), so that the DNA nanopores' structure remains compact. The setpoint was set at 0.22 nN, which is low enough to resolve the fine details of the sample surface. The setpoint is a predefined value by the user, which the AFM system uses to regulate the interaction forces between the tip and sample during the imaging process. During scanning, the AFM system continuously monitors the interaction forces and adjusts the tip-sample distance to maintain the setpoint. If the forces deviate from the setpoint, the system applies feedback mechanisms to control the distance between the tip and the sample, ensuring that the desired interaction forces are maintained.

4.7. Data analysis

Because of the small dimension of the structures, we need to find an approach that allows us to obtain precise localization from the fluorescence images, which are typically diffraction limited. For this reason we employed Single Molecule Localization Microscopy (SMLM), and specifically DNA PAINT, as it provides nanoscale resolution while also having high temporal resolution. This technique uses of the stochastic blinking of the fluorophores during the imaging process at different times, termed blinking, to achieve non-overlapping point spread functions (PSFs) which are used to construct the super-resolved image. The Picasso open-source software is capable of doing this localization. More specifically, the localization of individual fluorophores is performed by using the localization function which operates by fitting a Gaussian function to the PSFs of each fluorophore in each frame of the image which are the combined to form a super resolution image, as shown in Figure 27. The center of the Gaussian function is then taken to be the location of the fluorophore, which allows for high resolution imaging of the sample. After obtaining the localization file, it is saved as an hdf5 file, which we can directly import it to the render function, in order to generate the image that incorporates the localization. We thus obtain the final image, which we can further analyze, for instance for measuring the angles of the nanopores and determine their open/closed state.[44]

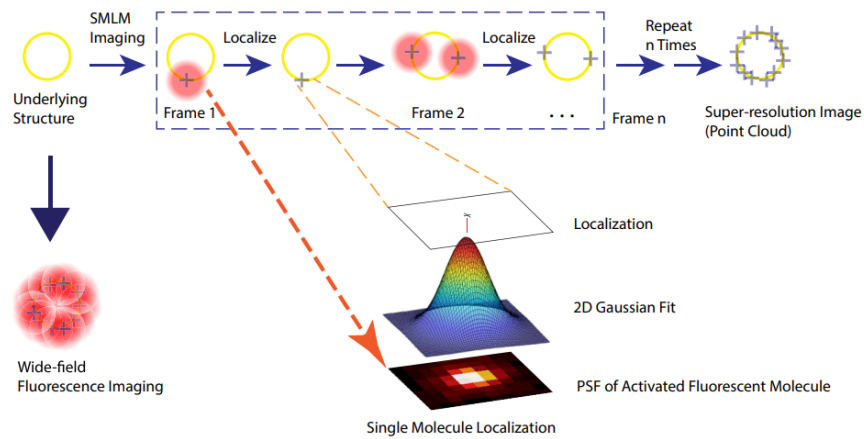
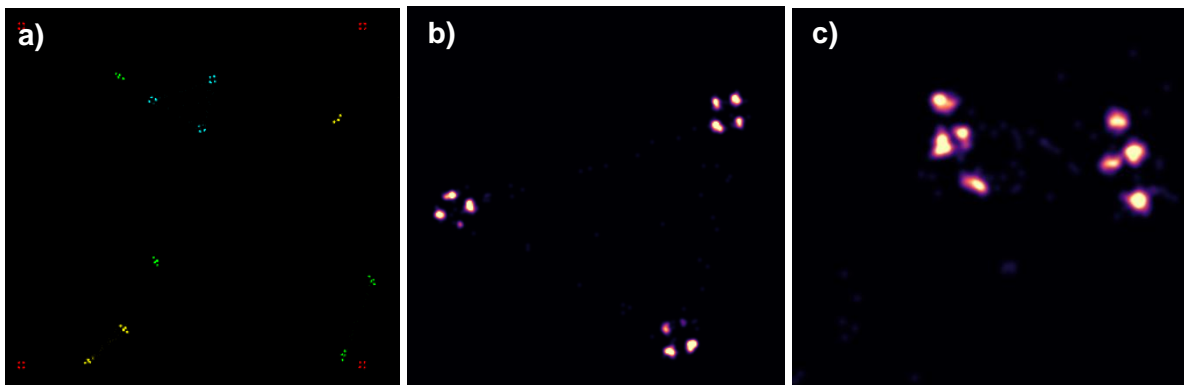


Figure 27: Localization function algorithm in SMLM using Picasso software [44]

5. Results and Discussion

5.1. Simulations

Picasso software can also provide with simulations with which we can estimate how the images after the experiments should look like in ideal conditions. Within this simulation part, it is possible to select the number and type of structures that we want to visualize. Selecting one of the options in the custom function allows us to have an arbitrary coordinate system in which we can input exactly the position of the fluorophores. In this way we can simulate how the structures will look like after the localization. An example of how the nanopores should look like with the experimental conditions we will use is shown in Figure 28.



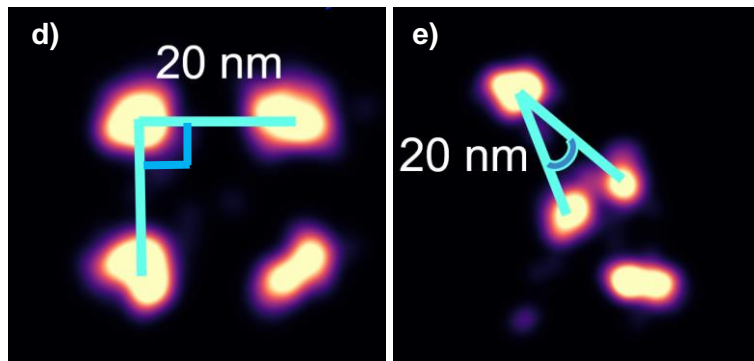


Figure 28: Simulation images of a) DNA nanopores at 30° and 90° angle, b) DNA nanopores at 90° angle, c) DNA nanopores at 30° angle.

In Figure 28a) we see the simulation of several nanopores that are in closed and open state, as their angles are 30° and 90°. In b) we have another simulation image in which we can see how the nanopores would look like in 90° angle, while in c) it is for 30° angle nanopores. Finally, in d) and e) we can see the zoomed images of nanopores that exist in both angles respectively and the distances together with the angles that can be measured are shown. By measuring the angles of a very large numbers of the DNA nanopores in different experiments we can get information about their dynamics and the nanomotions.

5.2. Gel Electrophoresis

Gel electrophoresis analysis is a fundamental technique in biochemistry, allowing for the separation and characterization of macromolecules based on their size and charge. In the context of our research on DNA origami nanopores, gel electrophoresis serves as a critical tool for evaluating the structural integrity and purity of our constructed nanopore assemblies. In this section, we present the results and subsequent discussion of our gel electrophoresis experiments conducted to assess the migration behavior of DNA origami nanopores.

1st DNA origami nanopores sample

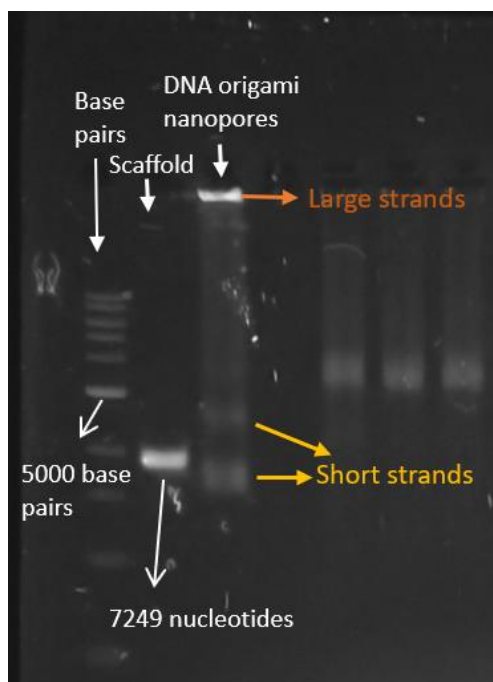


Figure 29: Agarose gel electrophoresis of the 1st DNA nanopores sample we assembled. 15mM Mg^{2+} ions were used for the purification of this assembly. The first well is used as a reference and it contains base pairs, which increase by 1000 in the upward bands. Second well contains the scaffold, which is a single stranded DNA molecule used as a reference, while the third well contains the DNA nanopores.

In the above Figure 29 we have the image of gel electrophoresis for the 1st sample of DNA origami nanopores that we assembled. The first well contains base pairs of nucleotides and is used as a reference, while the second well contains DNA scaffold, which is also used as a reference. The third well is the one that consists the DNA nanopores and we can observe that the smaller nanopores migrated farther from the loading well (yellow arrows) compared to the larger ones (orange well), reflecting their faster mobility. The well resolved band in the top indicated with the orange arrow, provides us with information that these are slower structures with no mobility and do not migrate within the gel, which means that the fragments are too large to move through the agarose gel. This seems reasonable since the DNA origami nanopores synthesized should be 13744 nucleotides in total. The DNA nanostructures that stayed in the bright band on top, may also contain aggregates, which have on overall larger size. This might be due to the high Mg^{2+} ion concentration (1.5x) during the assembly process, which promotes compact DNA structures and the tendency to aggregate with each other due to less repulsion between the DNA strands. On the other hand, the next brighter band we observe is below the scaffold, shown in yellow arrows, and it means that these are more compact structures that were able to move and run faster. Comparing it to the scaffold reference, we estimate that these structures consist of less than 7249 nucleotides.

2nd DNA origami nanopores sample

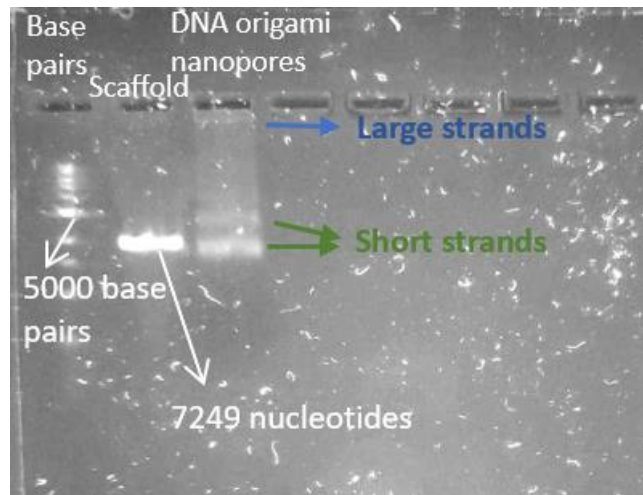


Figure 30: Agarose gel electrophoresis of the 2nd DNA nanopores sample we assembled. 10mM Mg^{2+} ions was used for the purification of this assembly. The first well is used as a reference and it contains base pairs, which increase by 1000 in the upward bands. Second well contains the scaffold, which is a single stranded DNA molecule used as a reference, while the third well contains the DNA nanopores.

In Figure 30, we can see for the second sample of DNA nanopores that the DNA origami structures do not form aggregates, compared to the 1st sample, as we do not see any clear bright band at the top, where the blue arrow points. Also, the structures migrate down to approximately the same point as the scaffold bright band, and we can see these nanopores in the band being pointed with the green arrows. However, in the 1st sample above, the nanopores reach a bit further down, as seen in the yellow arrows in Figure 29. The reason for these results may be that we used different buffer solution for the purification part of the 2nd DNA origami sample, which contains 10 mM of Mg^{2+} ions (Buffer B+ solution), instead of 15mM as in the 1st sample. This means that the structures may not become so compact but a bit larger in size, so they cannot migrate a lot further to the gel. Additionally, with less Mg^{2+} ions the structures do not have the tendency to form aggregates that will stay at the top part of the gel.

5.3. Atomic Force Microscopy (AFM)

Atomic Force Microscopy (AFM) is a versatile imaging and characterization technique widely employed in nanoscience to probe the topographical and properties of nanostructures with exceptional precision. AFM played an important role in validating the successful assembly of our DNA origami nanopores, by finding the suitable conditions to visualize the open channels. Among the three different modes for AFM, the tapping and QI mode were used, and the experiments were conducted mostly in a liquid medium of the buffer solution that contains the Mg^{2+} ions for ensuring the stability of the DNA origami.

Sample A: Nanopores without polylysine-tapping mode-in air

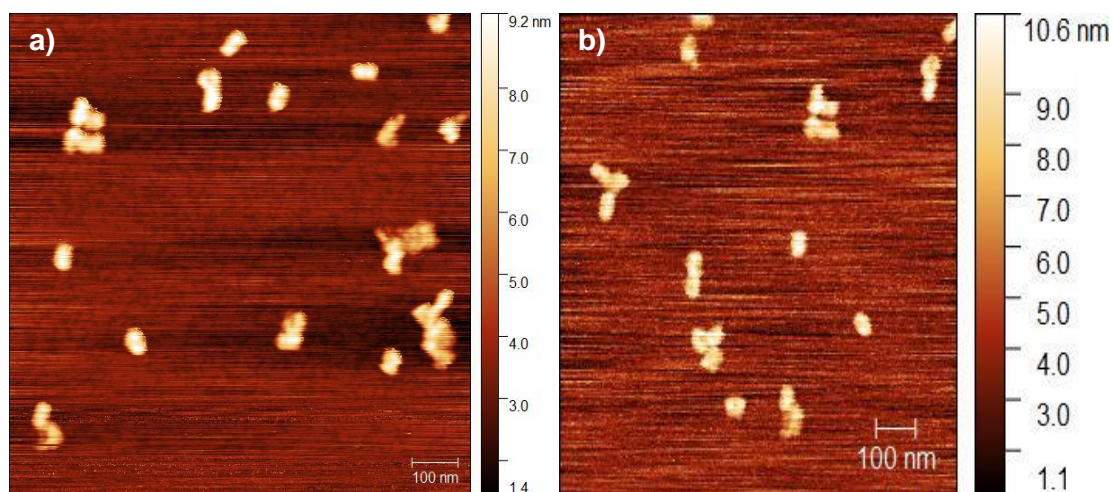


Figure 31: a) Atomic Force Microscopy (AFM) image of Sample A without Polylysine at the substrate- under tapping mode-in air. The AFM image indicates the height of the DNA nanopores, b) selected zoomed area image of the Sample A without Polylysine at the substrate- under tapping mode-in air.

In the above Figure 31 we visualize the DNA origami nanopores in tapping mode AFM. It is not possible to assess the nanopore structure from the above images, as there are no channels visible in the images. We measured a few of the DNA nanopores' height as shown in Figure 32 and Table 4 and we determined an average height of 4.87 nm, which could mean that the structure of the nanopores is not the desirable one, or the nanopores do not stay flat on the mica surface. It is possible that many of the DNA origami nanopores are sitting in a certain angle on the substrate. Therefore we repeated the AFM imaging but this time adding polylysine on the mica surface in order to increase the probability of the nanopores aligning with the substrate surface. Importantly, the experiment is conducted in air, which means that the DNA origami is without the presence of Mg^{2+} ions, thus its structure tends to expand. This could justify the low value of average height of the nanopores. The expansion happens due to the negatively charged phosphate groups in DNA that experience greater electrostatic repulsion, causing the DNA strands to repel each other.

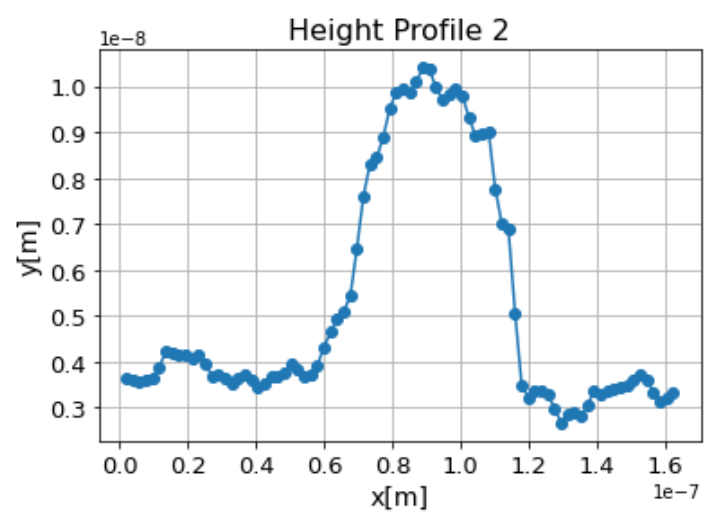
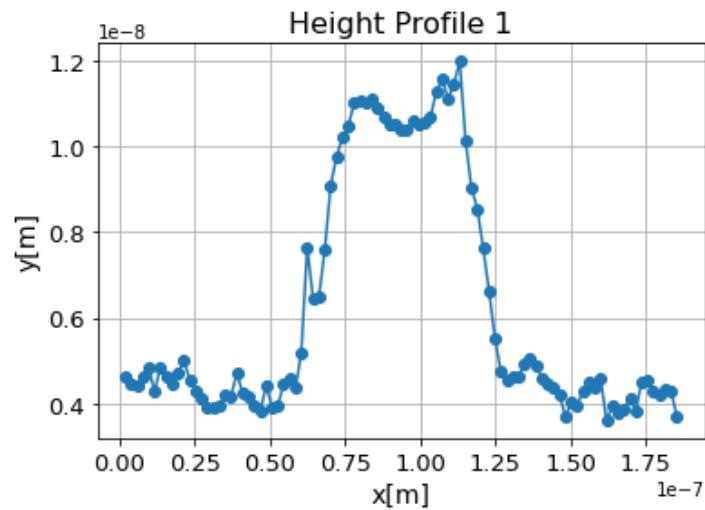
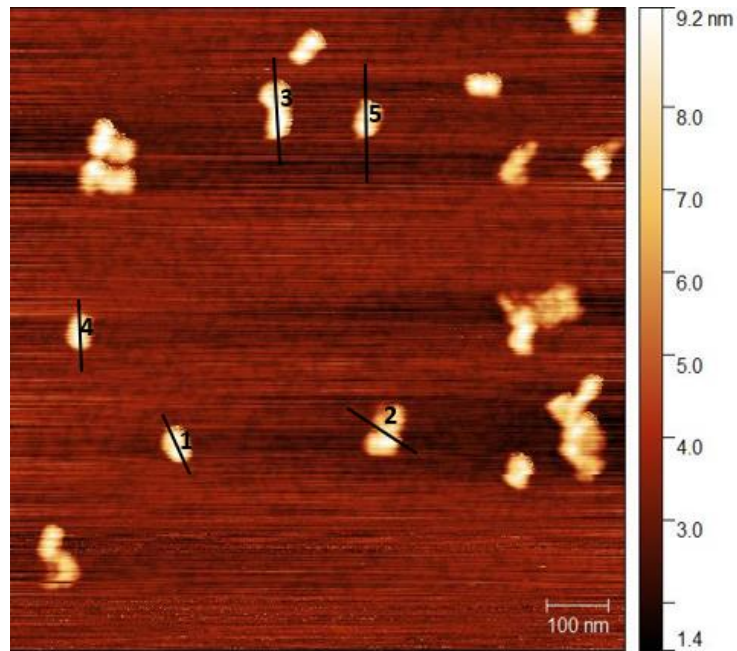


Figure 32: AFM image of the Sample A indicating the height profiles that got measured. In the two graphs we see the height profiles of the first and second nanopore that are shown in the AFM image. The x axis is multiplied by 10^{-7} , as seen on the bottom right, while the y axis is multiplied by 10^{-8} as seen on the top left of the graph.

| Profile | Height [nm] | Error [nm] |
|---------------------------------|-------------|------------|
| 1 | 5,12 | 1,3 |
| 2 | 5,27 | 1 |
| 3 | 4,75 | 0,51 |
| 4 | 5,15 | 1,3 |
| 5 | 4,1 | 0,45 |
| Average height: 4,878 nm | | |

Table 4: Measured heights of the nanopores shown in Figure 32, providing the errors in measurements and the average height.

Sample B: Nanopores with polylysine-QI mode-in liquid

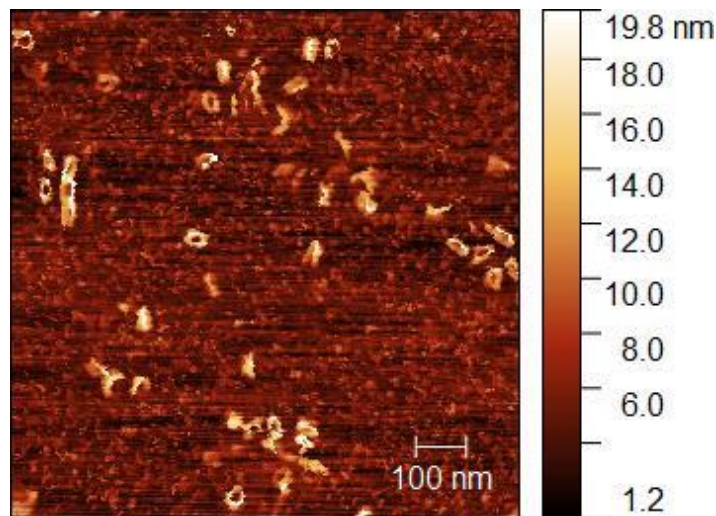
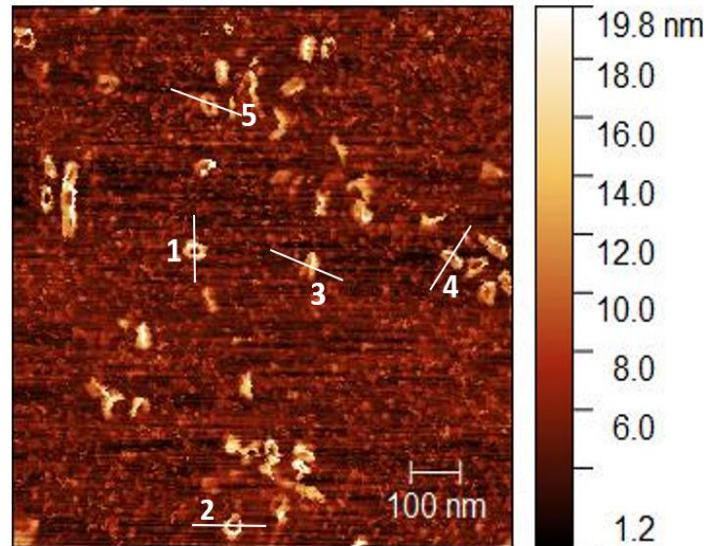


Figure 33: Atomic Force Microscopy (AFM) image of DNA origami nanopores with Polylysine deposited on the substrate, under QI mode-in liquid.

In this mode, in Figure 33, we can see the real shape of the nanopores, as well as the channels. This means that polylysine attracts the DNA nanopores so that they stay immobilized on the substrate surface. In this way we can prove that what we have assembled is actually DNA nanopores with open channels. In Figure 34 we can see the selected profiles for the height measurement. The fact that the graphs with the height profiles have two peaks

and one deep area between them, which has a height approximately at the same value as the background (polylysine) shows that the nanopore is facing with the channel open. The two peaks are shown with black arrows in the graphs of Figure 34, while the deep area indicating the open channel of the nanopore is shown with orange arrow. The measurements are shown in Table 5, where we can see that the average height is 10.91 nm, which is significantly higher than the average from Table 5 (no polylysine, air mode). The fact that we have used liquid mode makes the nanopores more compact, as the Mg^{2+} ions help with keeping the structure more stable. Therefore the nanopores, compared to the previous air mode, do not expand.



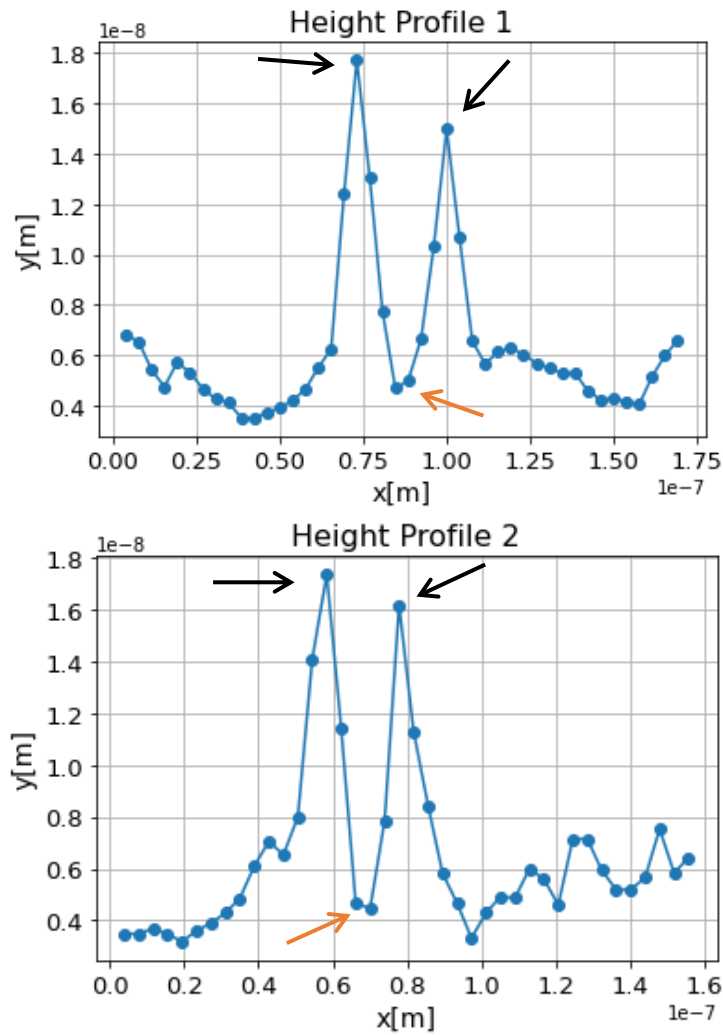


Figure 34: AFM image of the Sample B DNA origami indicating the height profiles that got measured. In the two graphs we see the height profiles of the first and second nanopore that are shown in the AFM image. The x axis is multiplied by 10^{-7} , as seen on the bottom right, while the y axis is multiplied by 10^{-8} as seen on the top left of the graph.

| Profile | Height[nm] | Error [nm] |
|--------------------------------|------------|------------|
| 1 | 12,45 | 1,8 |
| 2 | 7,03 | 1,2 |
| 3 | 12,45 | 1,8 |
| 4 | 6,82 | 1,5 |
| 5 | 15,802 | 1,1 |
| Average Height: 10,91nm | | |

Table 5: Measured heights of the nanopores shown in Figure 34, providing the errors in measurements and the average height.

In Figure 35 we can directly see the comparison between the two images we just analyzed of the first sample (S1). It is worth mentioning that the substrate roughness in the first case without polylysine is 375.5 pm, while in the second case is 1326 pm.

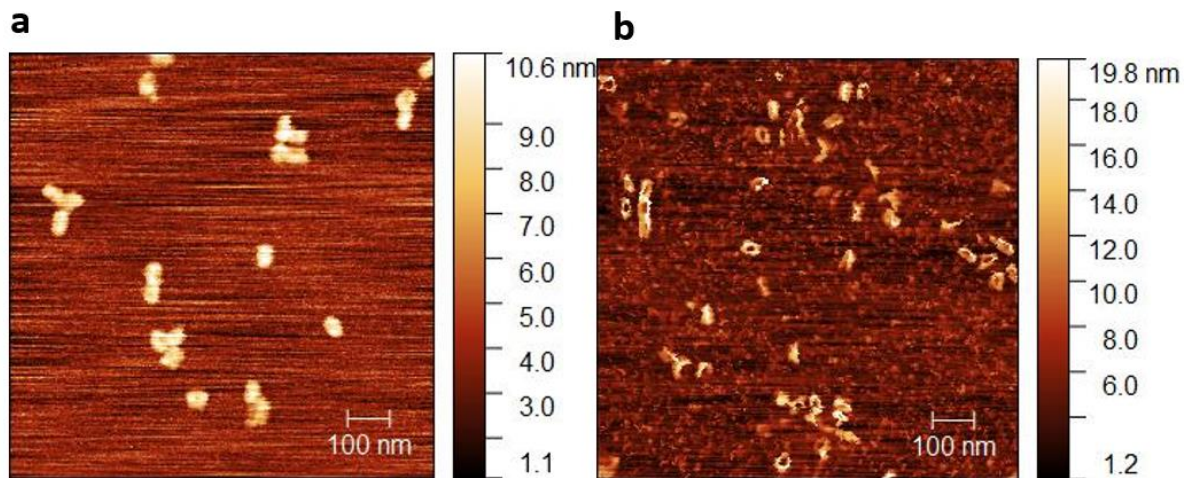


Figure 35: AFM images of S1 (Sample 1). a) Represents the AFM image in tapping mode, using a mica substrate without polylysine and conducting the experiment in air, b) Represents the AFM image in QI mode, using a mica substrate with polylysine and conducting the experiment in liquid.

Sample C: Nanopores with polylysine-QI mode-in liquid

In Figure 36 we can see the AFM images from Sample C. Polylysine was incubated at the mica substrate, so that the DNA origami can immobilize on the surface, The visualization was conducted in liquid using QI mode. The structure seems to be like the nanopore structure, as open channels can be seen from the images. This experiment is conducted in the same way exactly as Sample B, thus we see that our results are reproducible.

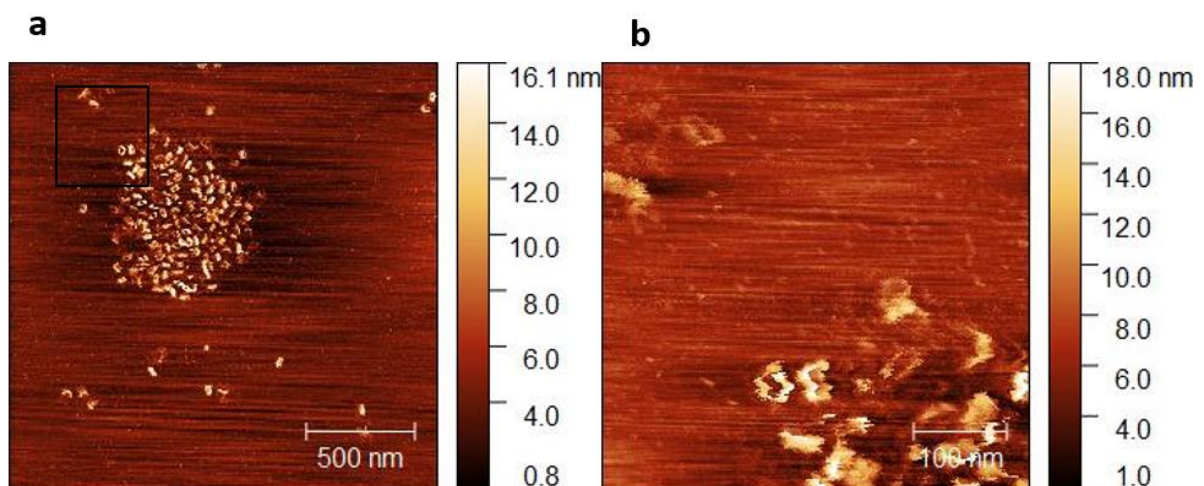


Figure 36: AFM images of S2 (Sample 2). a) AFM image of S2 in QI mode, using mica substrate with polylysine. b) Zoomed in scan of the selected region in the black square from panel a).

5.4.Total Internal Reflection Fluorescence (TIRF) Microscopy

Total Internal Reflection Fluorescence (TIRF) microscopy, as discussed in the theoretical section, is a powerful optical imaging technique that enables the selective visualization of fluorophores near a surface. In this section, we present the results and discussion of our TIRF experiments, which were conducted to visualize the blinking that we expect to observe between the imager strands and the docking strands due to transient hybridization. We set out to systematically determine the optimal conditions for the fluidic chamber that could give us these blinking effects, thus enabling DNA PAINT imaging and analysis for our system. More than one type of chamber was developed, however, only two successfully allowed the flow of the solutions, and were therefore used for our sample preparation. While conducting the experiments for TIRF, we were varying three main parameters, namely (1) the buffer concentration, which contains the Mg^{2+} ions for the stabilization of the DNA origami in the fluid chamber, (2) the concentration of the DNA origami nanopores and (3) the polylysine concentration. There are also other parameters that can be varied, which are the ones related to the image acquisition. Therefore, in the following sections we will analyze how the results change while varying the concentration and values of these selected parameters.

5.4.1. Fundamental components of sample preparation

In Figure 37 below we observe three different cases of sample preparation. In case a) we have prepared a sample with only polylysine on the microscopy slide substrate, and we can clearly see that there is no fluorescence signal coming from any region of the sample. In case b) we have prepared a sample with polylysine and DNA origami nanopores. The background is mostly dark, with no fluorescent spots except for very few ones that we attribute to dirt or dust from the glass slide that was not removed during cleaning. Case c) contains only the polylysine with the imaging solution added to the chamber (i.e. no nanopores). In the last case the image was static with no fluorescent light moving during the whole imaging procedure. This suggests that the imager strands have tendency to attach to the polylysine-coated surface, which is reasonable, since the negatively charged backbone of the DNA imager strands can be attracted by the positively charged polylysine coating of the substrate. This is further supported by experiments in which fluorescent DNA imaging strands exhibit strong binding to the whole length of a polylysine-coated substrate. [45] From this figure we understand that the only source of fluorescent light in the following experiments is the fluorophores from the imaging solution. It should be noted that the images of b) and c) were processed by ImageJ Software and were enhanced in contrast, in order to be able to see any type of fluorescent signal.

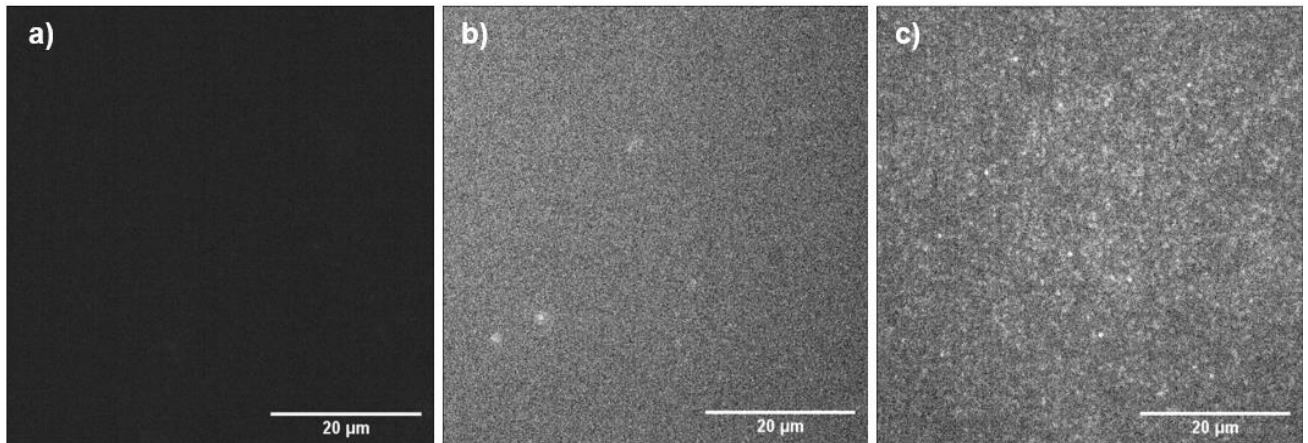


Figure 37: TIRF microscopy images of a) Sample with only polylysine on the substrate, b) sample with polylysine on the substrate and DNA nanopores solution, c) sample with polylysine on the substrate and imaging solution. The indicated scale on the bottom right of the images is 20 μm .

5.4.2. Experiments with sealed chamber

From this section onwards, the experiments involve samples that contain all the components (i.e. polylysine, DNA imager strands and DNA origami nanopores), as described in section 4.5.

Before we start analyzing the results it is important to mention that in many experiments the parameters we vary are the buffer solution concentration and the DNA origami nanopores concentration. The buffer solution contains Mg^{2+} ions, that contribute to the stability of the DNA structure. When there is low Mg^{2+} ions concentration the hybridization between the docking and imager strands will be weak, while with high concentration the hybridization is strong. For the DNA PAINT technique the hybridization should not be too strong, since the transient blinking comes from the binding and unbinding of the docking with the imager strands. It should not be too weak either, as sufficient time is needed during transient binding to localize the fluorophores. Therefore, the buffer solution should not be too low or too high in Mg^{2+} ions concentration, and an optimal concentration of Buffer B+ solution needs to be found. Additionally, when the concentration of DNA origami nanopores is low there might be lower DNA PAINT statistics, affecting the reliability of the analysis. On the other hand, when the concentration of DNA nanopores is high it is possible that aggregates form and the fluorescent signal is too bright, so it might be difficult to understand where it comes from and analyze it properly.

Figure 38 depicts the results of TIRF coated with 0.0001% polylysine and in different concentrations of DNA origami nanopores solution, which was washed with 10x diluted of Buffer B+ solution. Image a) contains 0.nM of DNA nanopore solution, while b) contains 0.5nM and finally c) contains 1nM of DNA nanopores. We observed no blinking during the whole imaging process. As shown, the three images are very similar but also with Figure 37c), that does not contain any DNA nanopores. Since the similarities are associated with the case of DNA nanopore absence, this could mean that the fluorescent signal comes from imager strands that are not bound to the DNA nanopores. It is very possible that the nanopores have not get attached to the substrate. It is rather possible that the nanopores are dispersed in the

chamber. This probably means that there is a problem with the hydrophilicity of the substrate, meaning that the polylysine is not properly attached on the substrate or it is not strong enough to attract the DNA nanopores. On the other hand, the 10x diluted Buffer B+ solution concentration could also be a problem because it may not contain enough Mg^{2+} ions in order to make the hybridization between the docking and the imager strands to happen.

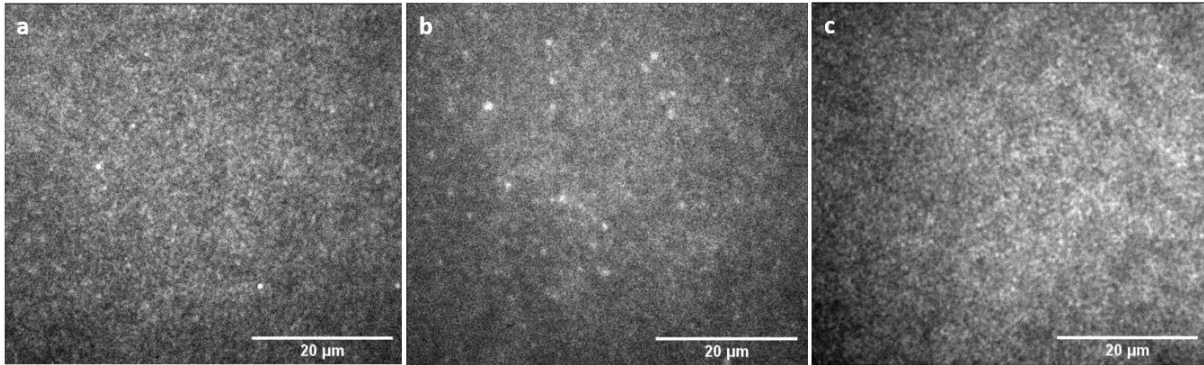


Figure 38: TIRF microscopy images of a) 0.3nM, b) 0.5nM and c) 1nM of DNA origami nanopores samples. that contains 0.0001% polylysine and has been washed with 10x diluted buffer solution. The scale bar at the bottom right is 20 μm .

For the above possible reasons, we wanted to use higher content of polylysine, with 0.001% concentration and see the images in the case of 10x diluted solution and also 4x diluted buffer solution, which contains more Mg^{2+} ions, that could make the hybridization more possibly to happen and then observe blinking. For this experiment the concentration of DNA nanopores was 1 nM. Figure 39a) represents the image of the sample with 4x diluted buffer solution, while b) with 10x diluted. The samples showed no blinking, throughout the whole experiment. Even though we increased the buffer solution concentration and also the polylysine concentration the problem remained. This could either mean that the buffer solution concentration is still not enough to make hybridization happen or that the problem could lay in the hydrophilicity, since the DNA nanopores do not seem to get attached to the surface. If the latter was true there would be blinking signal detected from the location of the nanopores laying on the polylysine substrate. Therefore, we tried to achieve hydrophilicity by using a different way of chamber preparation that is described in section 4.5.

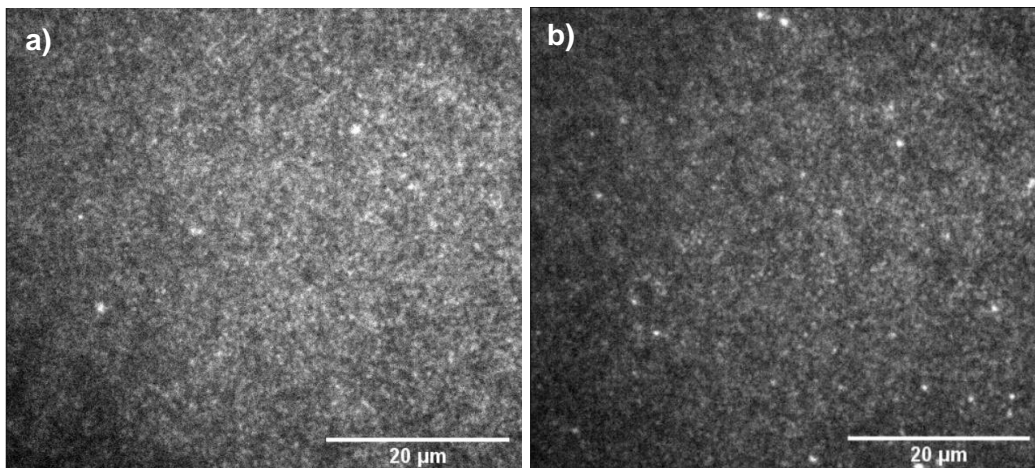


Figure 39: TIRF microscopy images of 1nM DNA nanopores and 0.001% polylysine on the substrate and with a) 4x diluted, b) 10x diluted Buffer B+ solution. The scale bar at the bottom right is 10 μm .

5.4.3. Experiments with non-sealed chamber

5.4.3.1 Different buffer solution concentrations

In Tables 6 and 7 below we can see the TIRF experimental results for a series of samples that are made with 0.001% of polylysine on the substrate and 1nM of DNA origami nanopores in the solution.

In this series of experiments blinking was noticed, thus DNA PAINT technique was successful for every sample with all the different buffer solution concentrations. This indicates that the construction of flow cell together with the concentration of polylysine in this type of chamber is suitable for creating the hydrophilicity needed for the DNA nanopores to get attached to the substrate. The buffer solution concentrations are also proper for giving the blinking behavior, but it is important to find out which one is the optimal one for giving the best image. This can be identified by the image that provides the largest number of localizations, which means that the image had many blinking spots that could be identified and fitted by the Picasso Software.

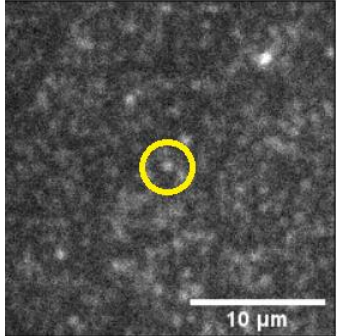
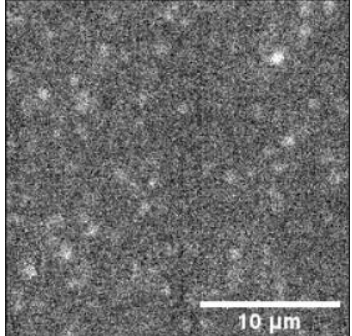
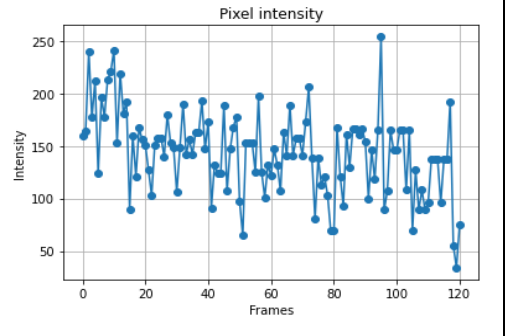
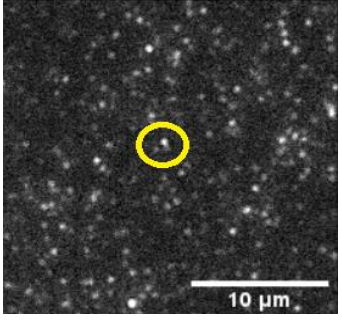
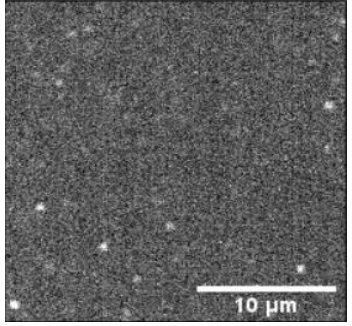
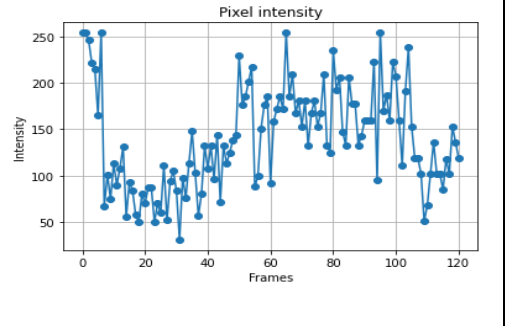
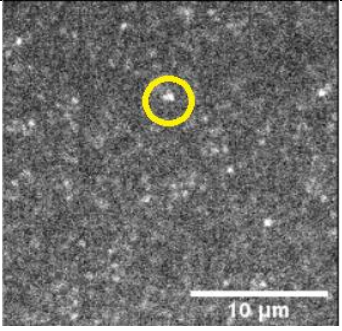
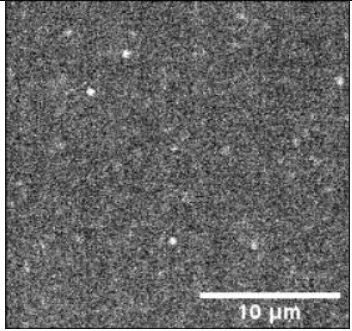
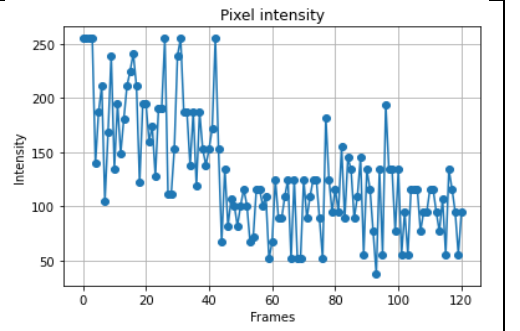
In the first column of Table 6 the different buffer solution concentrations are written, while in the second column the first frame from the TIRF images are shown, which are accompanied by the last frame visible in the third column. The last column represents the intensity of the indicated spot that is shown in the first frame images. In all samples, the images between the first and the last frame differ and more specifically it seems that the intensity drops, along with the bright spots that can be visible. This is most probably the effect of photobleaching, where the fluorophores fade when they are exposed to excitation light. Oxygen has been found to enhance photobleaching of the fluorescent probes, leading to reduced fluorescence signal and shorter imaging times. The fluorophores are found to react with oxygen when they get excited from the singlet to triplet state. It has been found that the triplet state has a longer lifetime than the singlet one, thus they react with oxygen for a longer time. [22] This makes even more sense, given the fact that in the non-sealed chamber case the solution is totally exposed to air, thus the fluorophores are even more prone to photobleaching. The images from the last column prove that the blinking exists, since the fluctuation in the intensity at the span of all frames is observable.

In Table 7 the localization images are shown, which are the location of the bright spots that can be identified by the Picasso Software. It is not possible to identify the structure of our DNA nanoactuators, as there is no indication of the four bright spots coming from the four corners where the docking strands are placed. That is most probably due to the fact that the objective lens used for our experiment is not suitable for resolving less than 20 nm.

In Figure 40 we can see the number of localized spots for all samples within the whole frame span. In Figure 40a) we have the histograms of the counts of localizations of all different samples. In order to be able to directly compare the results the number of counts are normalized to 1. In Figure 40b) the graph indicates the number of counts for the 7 frames that belong to this area [0,120], as shown in x axis. During the measurements of some experiments there was drift and the bright spots were getting blurry and it was difficult to distinguish, thus

the focus of the objective lens on the z-axis was manually changed. That can be seen in the image a) where the arrows indicate the point that there was a sudden drop in the counts of localizations and then an increase again. From both a) and b) cases it is obvious that the number of localizations generally drops with time, which shows the photobleaching. However, the sample with the most localizations in the initial state is the one with the 2x diluted buffer solution, as the localizations exceed the value of 2500 in the first frame. Figure 40 also shows that the bright spots in this sample are very distinguishable and clearly shown. However, there is not a certain pattern that is observed between the different concentrations of buffer solutions and the counts of localization. Nevertheless, another experiment with the same concentrations of 0.001% polylysine, 1nM DNA nanopores and 2x diluted buffer solution was conducted and it showed very similar results as this one. Therefore, the buffer solution concentration that is chosen for the next experiments is 2x diluted Buffer B+ solution.

DNA origami concentration: 1nM – Polylysine of 0.001%

| Buffer solution concentration | First frame | Last frame | Spot intensity |
|-------------------------------|---|---|---|
| 1x diluted |  |  |  |
| 2x diluted |  |  |  |
| 4x diluted |  |  |  |

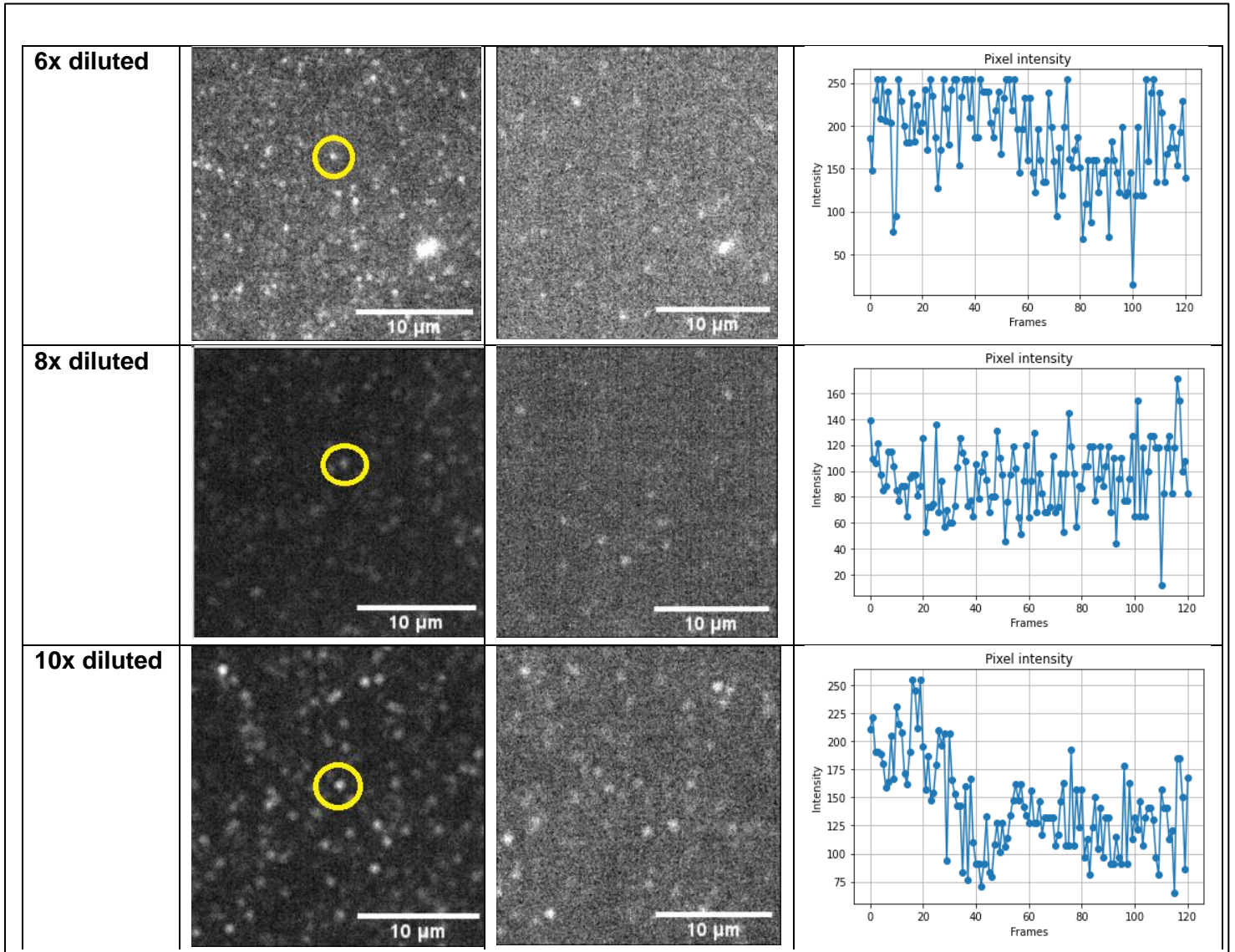


Table 6: Experimental results of TIRF microscopy experiments with 0.001% polylysine on the substrate and 1nM of DNA origami nanopores in the system. In the first column the concentration of Buffer B+ solution is indicated, while in the second the image of the first frame is shown. In the third column the last frame is shown, while in the last one the intensity of the spot that is indicated in the first frame.



| Localization Images | |
|-------------------------------|--|
| Buffer solution concentration | |
| 1x diluted |  |
| 2x diluted |  |
| 4x diluted |  |
| 6x diluted |  |
| 8x diluted |  |
| 10 diluted |  |

Table 7: First column indicates the buffer solution concentration, while in the second column the localization images from Picasso Software are shown.

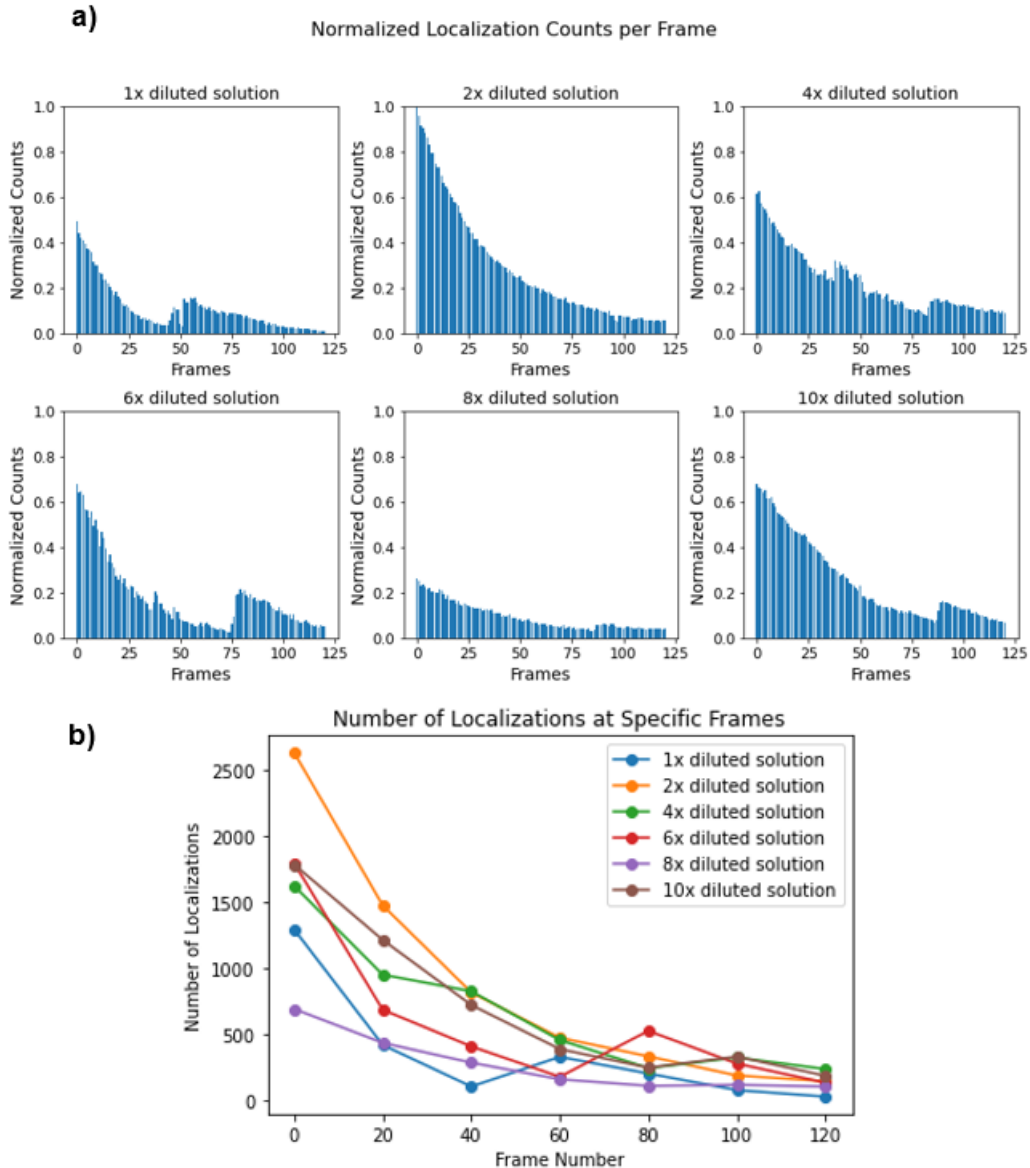


Figure 40: a) Histograms indicating the normalized localization counts for every frame for the experiments of Table 6, b) graph showing the number of localizations for each of the frames shown in x axis.

5.4.3.2 Different DNA origami nanopore concentrations

In Table 8 and 9 below we can now see the results for the experiments that were conducted with 0.001% of polylysine on the surface, using the 2xdiluted Buffer B+ as buffer solution and varying the DNA nanopores concentration every time. The experiments are exhibited in the same way as in the previous tables 6-7 above. They also appear blinking behavior, thus the DNA PAINT was successful for all concentrations of DNA nanopores in the system. It is important find the nanopores concentration which can give the optimal results. DNA nanopores concentration can modify the density of fluorescent signal, as mentioned above. From the images of the first frame belonging to the second column of the table, we can already

observe a difference in the signal density, that increases as the concentration of nanopores also increases. The last frame images indicate that the amount of signal decreases with respect to the first frame images, which clearly shows in a qualitative way the effect of photobleaching. This can also be confirmed by Figure 41, where the graph shows that the number of localizations drops with the number of frames. The last column of Table 8 confirms the blinking behavior of the experiments, as the fluctuation of the intensity of a blinking spot over the frames is graphed. Figure 41 does not contain the histograms with the normalized counts per frame, because there was a problem with the data file exported from Picasso Software. The problem lies in the fact that during the measurement of the third sample with the 0.7nM of DNA nanopores there was much drifting, resulting in the value of zero counts at a certain point, which can also be visible at Figure 41 at the value of 40 frames in the green line. However, we can still get information from this graph and understand that the sample with the most localizations is the one with the 1nM of DNA nanopores in the chamber. This makes sense, since the nanopores in which the imager strands bind to and create the blinking are even more, in order to provide more localization spots for analysis. Therefore, we select to move with our experiments by using 1nM of DNA origami nanopores.

2x diluted Buffer solution – 0.001% Polylysine

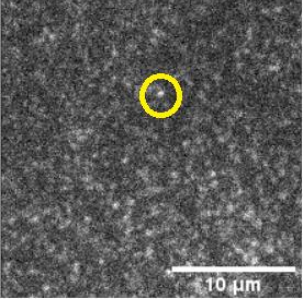
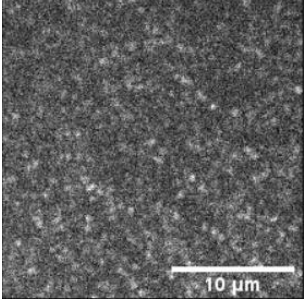
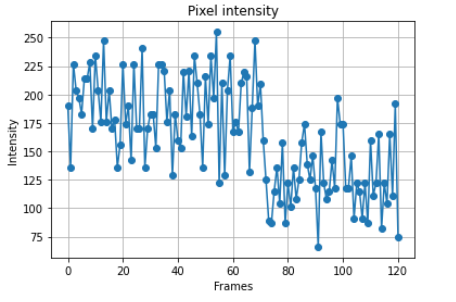
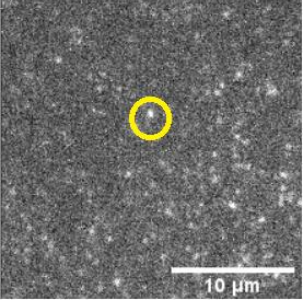
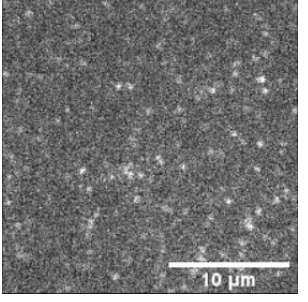
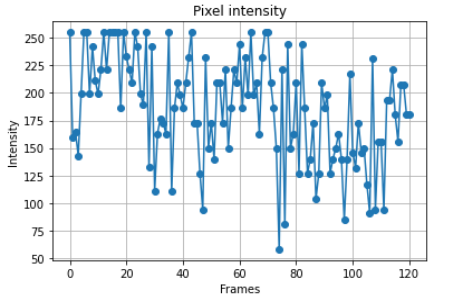
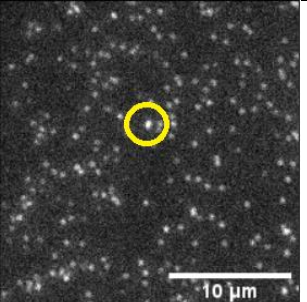
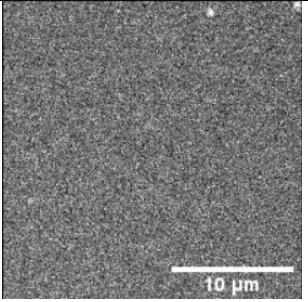
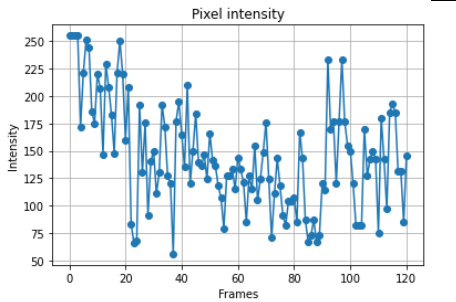
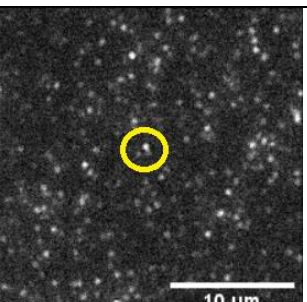
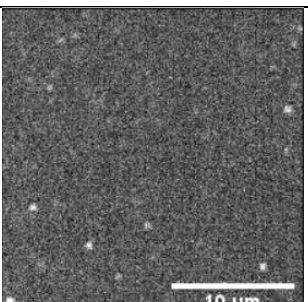
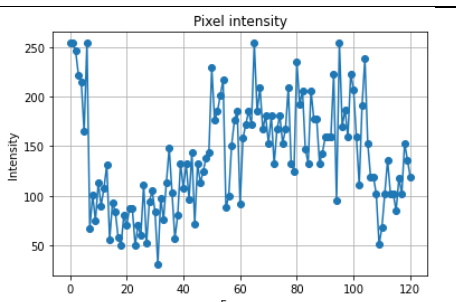
| DNA nanopores concentration | First frame | Last frame | Spot intensity |
|-----------------------------|---|--|---|
| 0.3nM DNA nanopores |  |  |  |
| 0.5nM DNA nanopores |  |  |  |
| 0.7nM DNA nanopores |  |  |  |
| 1nM DNA nanopores |  |  |  |

Table 8: Experimental results of TIRF microscopy experiments with 0.001% polylysine on the substrate and 2x diluted Buffer B+ solution. In the first column the concentration of DNA origami nanopores is indicated, while in the second the image of the first frame is shown. In the third column the last frame is shown, while in the last one the intensity of the spot that is indicated in the first frame.


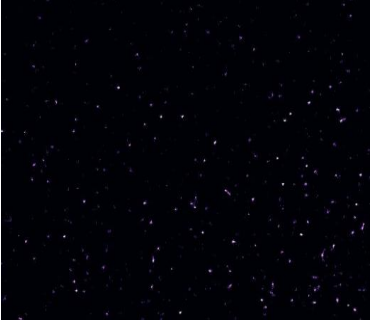


| Localization Images | |
|--|--|
| DNA origami nanopores concentration | |
| 0.3nM DNA nanopores |  |
| 0.5nM DNA nanopores |  |
| 0.7nM DNA nanopores |  |
| 1nM DNA nanopores |  |

Table 9: First column indicates the DNA origami nanopores concentration, while in the second column the localization images from Picasso Software are shown.

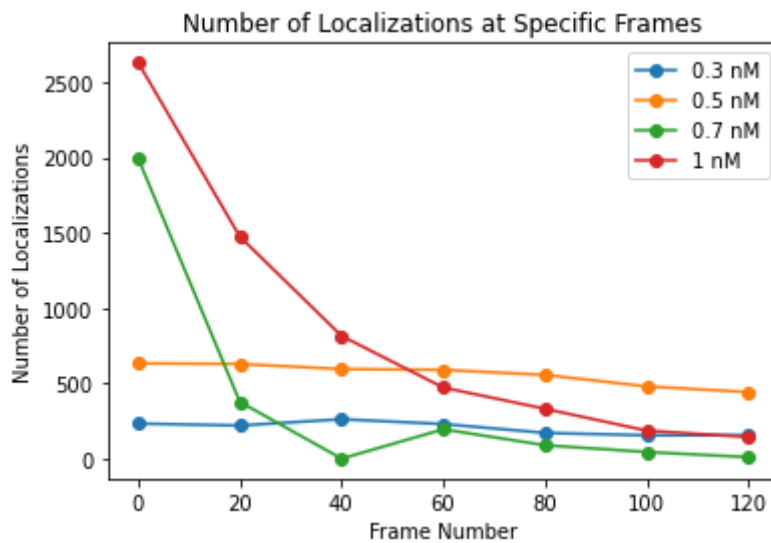


Figure 41: Graph with the number of localizations for each of the frames that are shown in x axis.

5.4.3.3 Different laser power from the microscope

Changing the laser power, which we use for the microscope, can have big effect on the results. More specifically, the fluorophores that are attached to the imager strands get excited when they are exposed to light. High laser power can result in smaller number of fluorophores being excited, while higher laser power can give a larger number, thus a larger signal intensity. However, in last case could also lead to photobleaching faster than the cases with lower laser power.

In Tables 10 and 11 the experimental results of one sample with 2x diluted buffer solution and 1nM DNA nanopores are visualized in three different laser powers of 20mW, 30mW and 40mW, as can be seen from the first column of the table. The difference between the first frames for each laser power is clear, as the signal intensity increases with laser power. In the case of 20mW is very difficult to distinguish the blinking spots properly, while this slowly changes reaching out to 40mW. The same can also be seen in a qualitative manner from the localization images in Table 11, as at the last one the localizations are much more detectable, while the ones at 20mW are barely visible. The last column of Table 10 indicates the fluctuating behavior in intensity of one blinking spot, which confirms that transient blinking occurs. In Figure 42 the normalized counts per frame and the graph showing the real number of counts for specific frames are shown. Something that can be understood from both a) and b) is that in the case of 20mW the number of localizations is very low and they increase in the cases with higher laser power. When using the 40mW laser power the number of counts is much more significant. However, these counts drop with time, as the number of frames increases, since the fluorophores are exposed to more light in this case. On the other hand, when using 20mW and 30mW photobleaching does not appear to be an issue, as the counts do not decrease with time. Despite this, we choose the case of 40mW to be the most appropriate to continue with our experiments, as the number of localizations is very important, so that we have more information for the analysis. It is important to mention that the images obtained

from this sample were from the same area, so that the hydrophilicity stays the same and the results can be comparable under the same conditions.

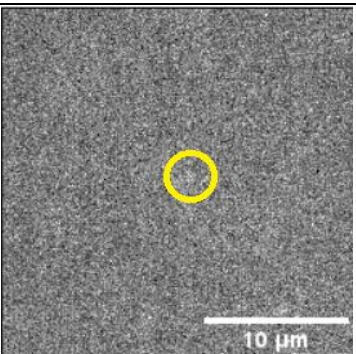
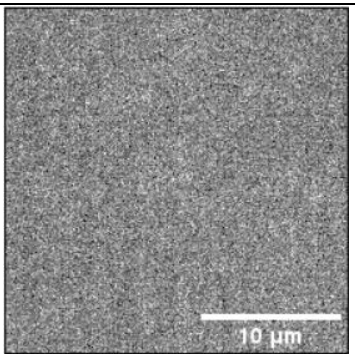
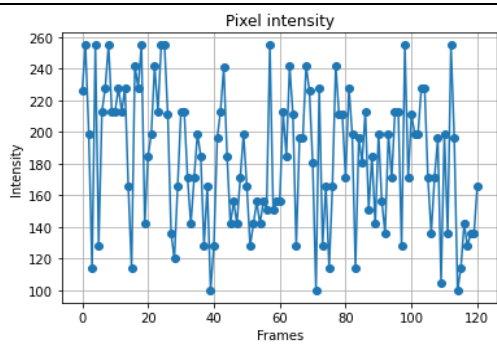
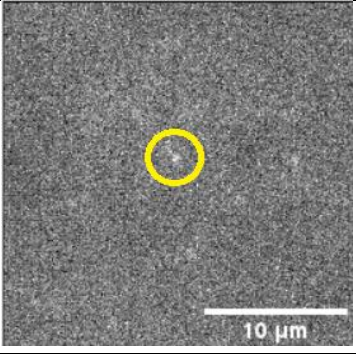
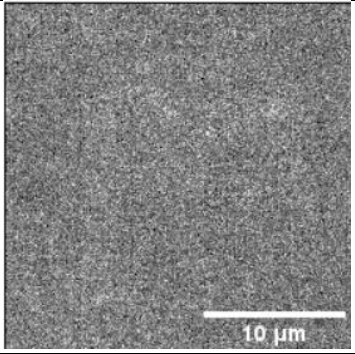
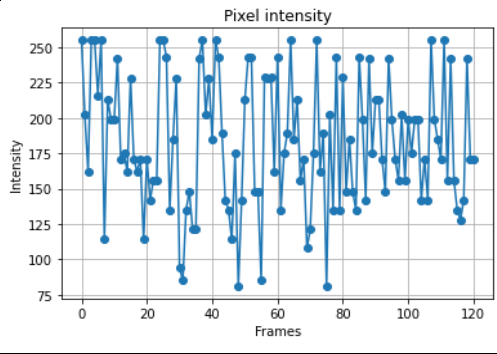
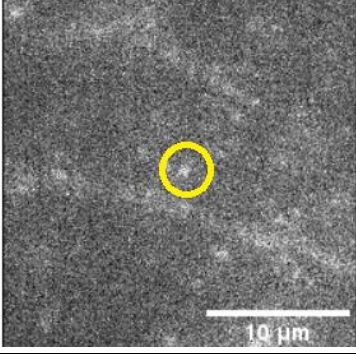
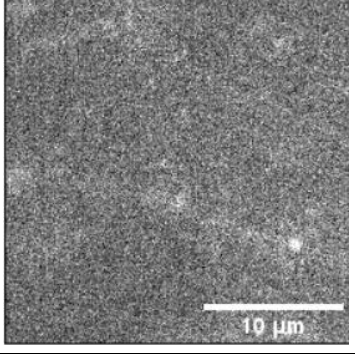
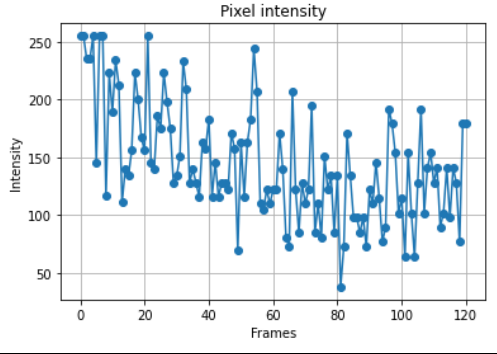
| 2x diluted Buffer solution – 0.001% Polylysine – 1nM DNA nanopores | | | |
|--|---|---|---|
| Laser Power | First frame | Last frame | Spot intensity |
| 20 mW |  |  |  |
| 30 mW |  |  |  |
| 40 mW |  |  |  |

Table 10: Experimental results of TIRF microscopy experiments with 0.001% polylysine on the substrate, 2x diluted Buffer B+ solution and 1nM DNA nanopores. In the first column the laser power is indicated, while in the second the image of the first frame is shown. In the third column the last frame is shown, while in the last one the intensity of the spot that is indicated in the first frame.



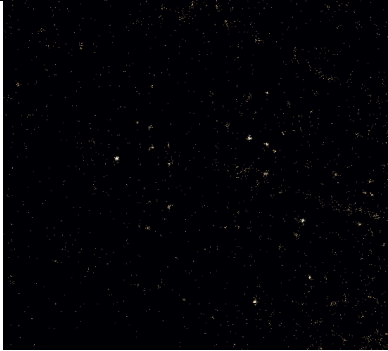
| Localization spots | |
|--------------------|--|
| Laser Power | |
| 20mW |  |
| 30mW |  |
| 40mW |  |

Table 11: First column indicates the value of laser power, while in the second column the localization images from Picasso Software are shown.

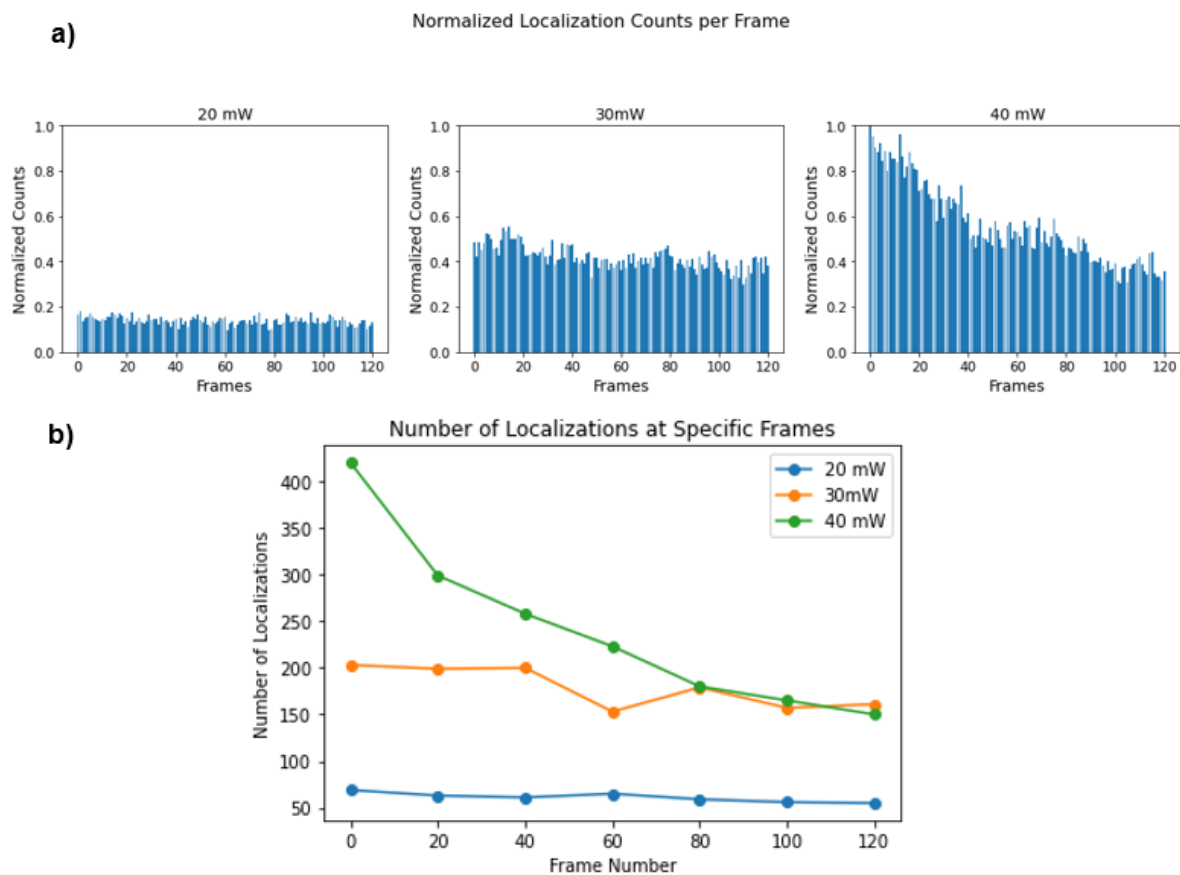


Figure 42: a) Histograms indicating the normalized localization counts for every frame for the experiments of Table 10, b) graph showing the number of localizations for each of the frames shown in x axis.

5.4.3.4. Different exposure time

DNA PAINT is a super resolution microscopy technique which requires many different frames that compose the final image. We can decide the duration which the sample will be exposed to for the acquisition of one frame. The more the acquisition of a frame lasts, the more fluorescent light there is that gathers at the detector. This means that since the amount of signal captured increases, the localization spots will be more.

In Tables 12 and 13 the experimental results are shown in the same way as the previous experiments. The sample that was observed has 0.001% of polylysine on the substrate, 1nM of DNA origami nanopores, that were washed with 2x diluted of Buffer B+ solution and finally, the laser power used for the whole experiment was 40mW. Four different exposure times were used, in order to understand what is the optimal one for accomplishing the DNA PAINT technique and get as much information as possible. Initially, by looking at the images for the first frame it is easy to understand that the brightest image is the one with 400ms exposure time. In parallel, we can see that the localization image of the case of 400ms exposure time in Table 13 has more localization spots that are visible for analysis. This can be confirmed by Figure 43, where we can see that the largest number of localization counts is when 400ms of exposure time is used, while the photobleaching does not seem to be significantly different in such case, thus we select to continue the experiments by using 400ms exposure time.

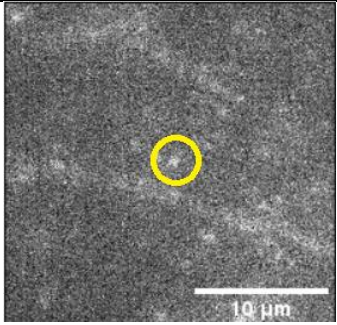
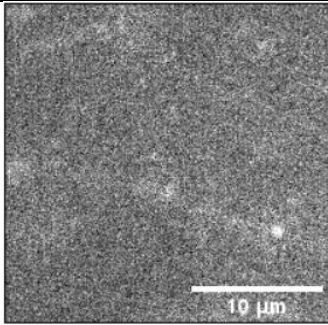
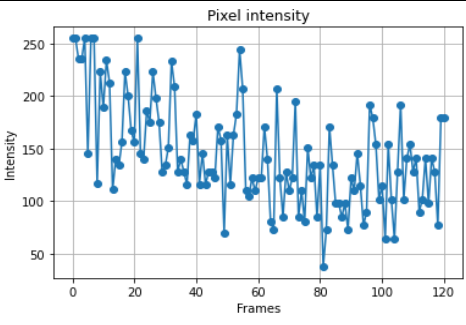
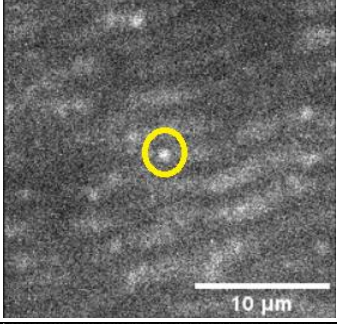
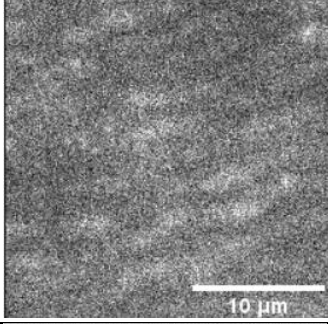
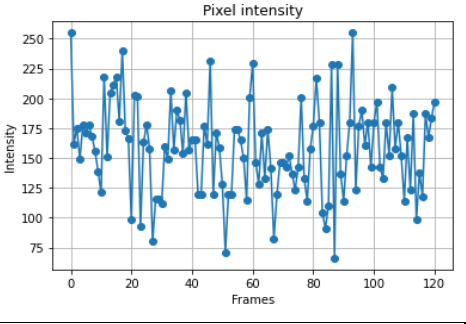
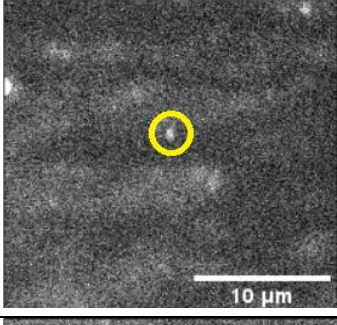
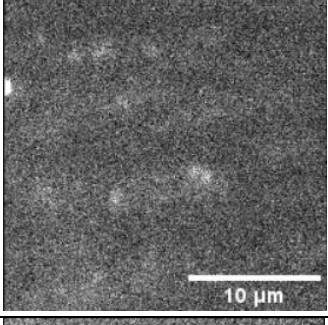
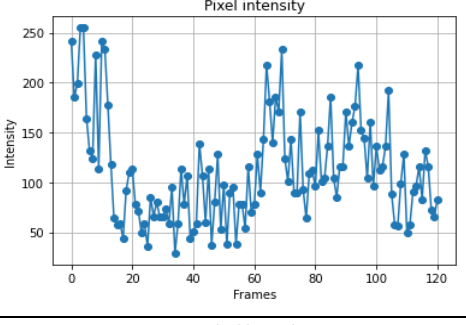
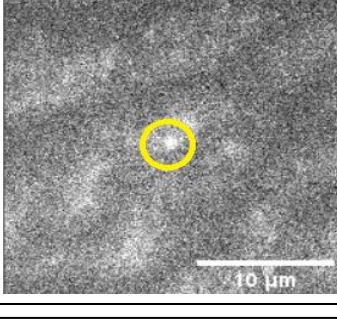
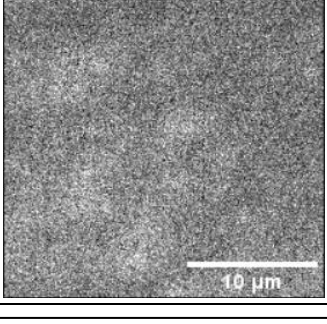
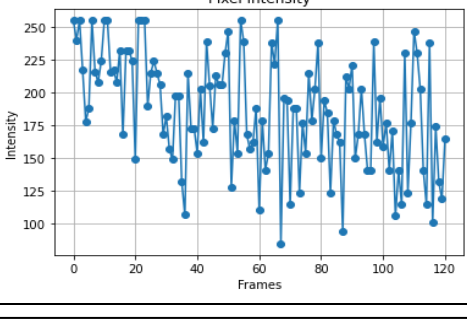
| 2x diluted Buffer solution – 0.001% Polylysine – 1nM DNA nanopores – 40mW | | | |
|---|---|--|---|
| Exposure time | First frame | Last frame | Spot intensity |
| 100ms |  |  |  |
| 200ms |  |  |  |
| 300ms |  |  |  |
| 400 ms |  |  |  |

Table 12: Experimental results of TIRF microscopy experiments with 0.001% polylysine on the substrate, 2x diluted Buffer B+ solution and 1nM of DNA nanopores. The experiments are conducted in 40mW of laser power. In the first column the concentration of DNA origami nanopores is indicated, while in the second the image of the first frame is shown. In the third column the last frame is shown, while in the last one the intensity of the spot that is indicated in the first frame.

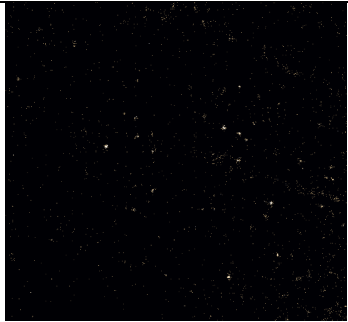


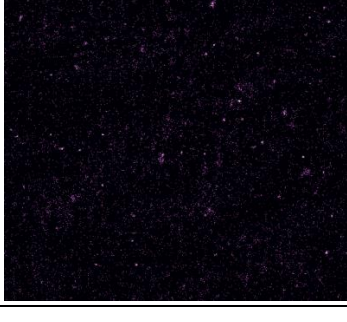
| Localization Images | |
|---------------------|--|
| Exposure time | |
| 100ms |  |
| 200ms |  |
| 300ms |  |
| 400ms |  |

Table 13: First column indicates the exposure time, while in the second column the localization images from Picasso Software are shown.

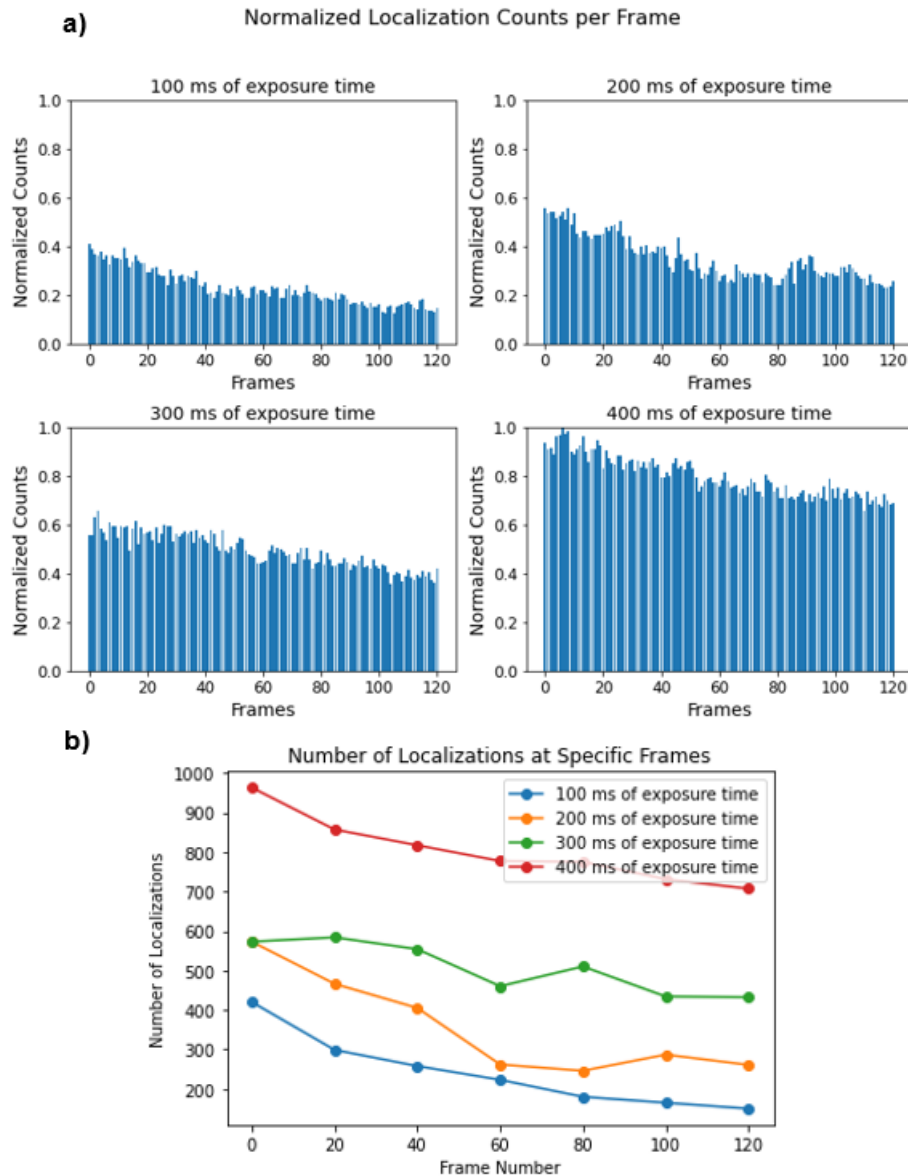


Figure 43: a) Histograms indicating the normalized localization counts for every frame for the experiments of Table 12, b) graph showing the number of localizations for each of the frames shown in x axis.

5.4.3.5. Different waiting and duration time

As mentioned above about DNA PAINT technique, since it is a super resolution technique, many frames need to be captured in order to get a final super resolution image. The frames that we use in our project are 121 for all cases. The acquisition of these frames can happen by using different waiting time and duration time. Waiting time is the time between the acquisition of two sequential frames, while duration time is the whole time needed to capture all 121 frames, meaning the final image.

In Tables 14 and 15 there are the experimental results that were conducted for a sample that was prepared with 0.001% of polylysine coating, 2xdiluted Buffer solution concentration, 1nM DNA nanopores concentration, using 40mW of laser power and 400ms of exposure time. The

different waiting and duration times are indicated in the first column of the table. The successful photobleaching for all cases can be seen from the last column, where the fluctuating intensity of the specific blinking spot indicated in the yellow circle of the first frame images is shown. The smallest the waiting time of the experiment is, the smallest the duration time, as the same number of frames needs to be preserved. Since the duration time differs, this should have an impact on the photobleaching rate, as we saw previously that the localization counts drop in every case over time due to the photobleaching effect. In the current experiment, since the same exposure time, laser power and concentrations of the different components of the flow cell are used, the localization counts should not differ between the different measurements. The fact that there is a slight difference in the counts has to do with the changing of the area of imaging every time. What we focus on in this experiment is the photobleaching rate, which is shown in Figure 44. From a) we can see that in the last case of 300ms waiting time – 50s duration time, the localization counts do not decrease significantly and compared to the other two cases. The same thing can be confirmed in Figure 44 b), where the orange and blue lines are steeper over time, compared to the green line. Therefore, shorter times are chosen to be the most suitable ones in order to achieve having less photobleaching.

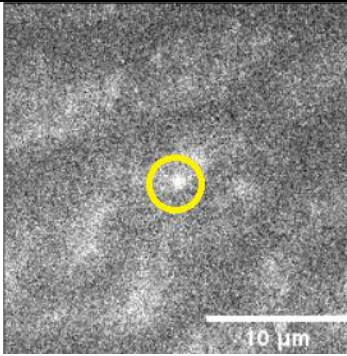
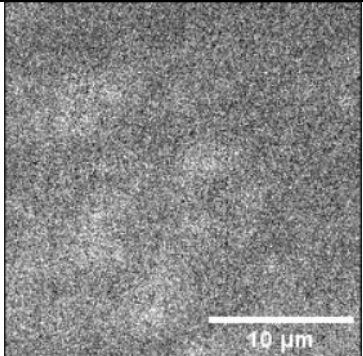
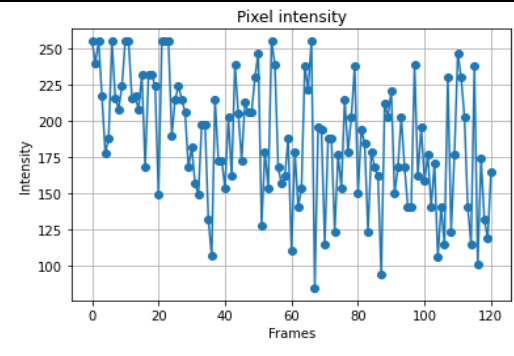
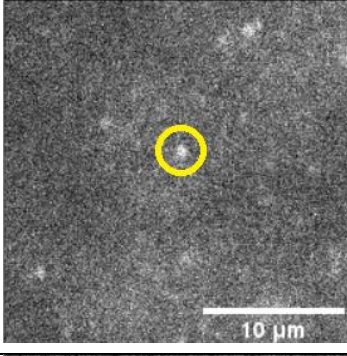
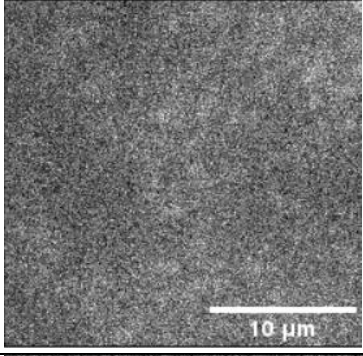
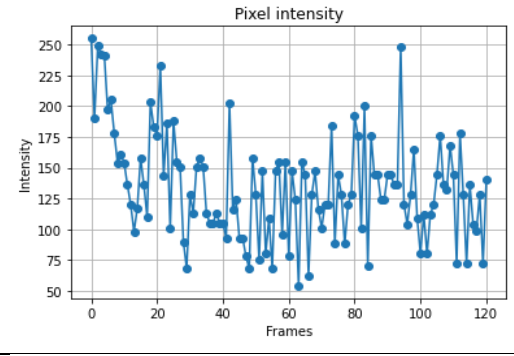
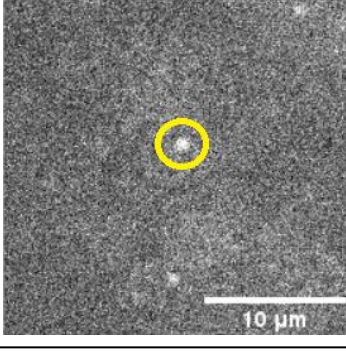
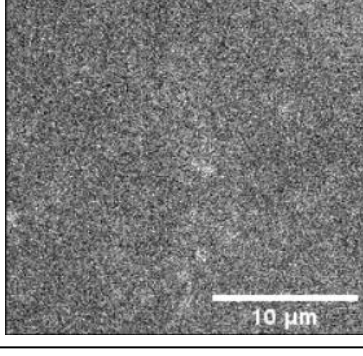
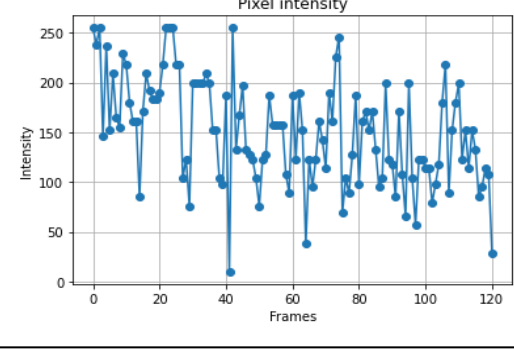
| 2x diluted Buffer solution – 0.001% Polylysine – 1nM DNA nanopores | | | |
|--|---|--|---|
| Waiting time – Duration | First frame | Last frame | Spot intensity |
| 1s – 2 min |  |  |  |
| 500ms – 1min |  |  |  |
| 300ms – 50s |  |  |  |

Table 14: Experimental results of TIRF microscopy experiments with 0.001% polylysine on the substrate, 2x diluted Buffer B+ solution and 1nM of DNA nanopores. The experiments are conducted in 40mW of laser power and 400ms of waiting time. In the first column the waiting time and duration of the experiment are indicated, while in the second the image of the first frame is shown. In the third column the last frame is shown, while in the last one the intensity of the spot that is indicated in the first frame.

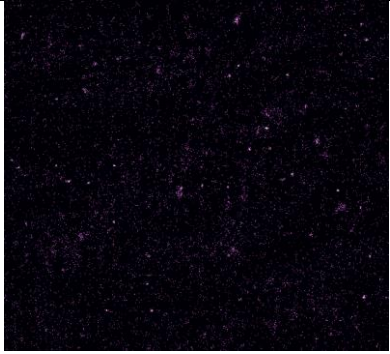
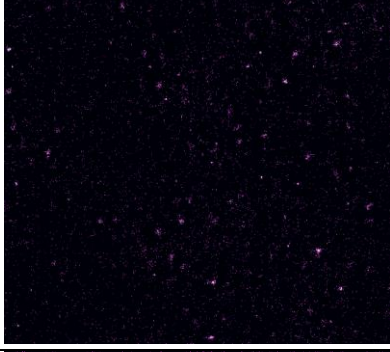
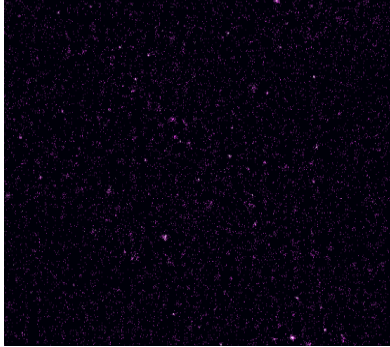
| Localization Images | |
|-------------------------|--|
| Waiting time - Duration | |
| 1s – 2min |  |
| 500ms – 1min |  |
| 300ms – 50s |  |

Table 15: First column indicates the waiting time -with the duration time, while in the second column the localization images from Picasso Software are shown.

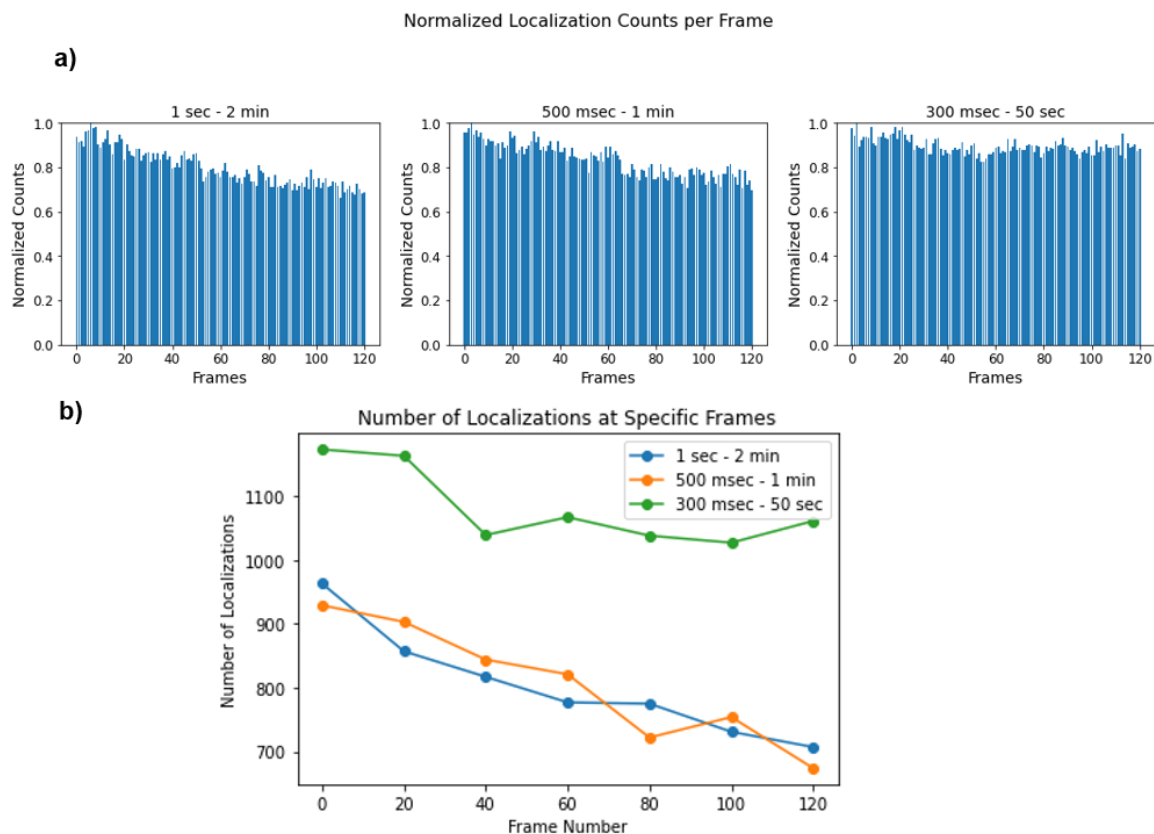


Figure 44: a) Histograms indicating the normalized localization counts for every frame for the experiments of Table 14, b) graph showing the number of localizations for each of the frames shown in x axis.

6. Conclusions

Our research has made significant progress in creating and visualizing DNA origami nanopores. We successfully assembled DNA origami nanopores, confirming their structural integrity through AFM experiments and Gel electrophoresis. Additionally, we established the optimal conditions and flow cell configuration for successful DNA PAINT imaging. It was crucial to maintain a non-sealed chamber to ensure the appropriate hydrophilicity for the deposition of polylysine on the substrate, facilitating the attachment and immobilization of DNA nanopores. This has been the key to achieving the blinking behavior for our experiments. Our exploration of various parameters yielded optimal results, characterized by maximum localization spots, an optimal signal density, and minimal photobleaching. The optimal conditions are summarized in Table 16 below.

| | |
|---|-------------------------------|
| Buffer solution concentration | 2x diluted Buffer B+ solution |
| DNA nanopores solution concentration | 1 nM |
| Laser power | 40 mW |
| Exposure time | 400 ms |
| Waiting time | 300 ms |
| Duration | 50 s |

Table 16: Optimal parameters found for DNA PAINT imaging.

While our findings are promising, further experiments conducted under consistent conditions and repeated iterations are essential to enhance the statistical robustness and reliability of our results. One of the prominent challenges encountered in our study is related to spatial resolution. We were unable to visualize individual corners of the DNA nanopores and study their dynamics due to the spatial limitations. This limitation prompted us to explore innovative solutions, leading us to the Exchange PAINT method, in which we could succeed Angstrom resolution, according to the paper Reinhardt et al, 2023 [46]. This can be achieved by using a sequential targeted labeling of docking strands in the sample. Many cycles are needed in order to obtain the final super resolved image. In each cycle different imaging strands are introduced, which have different orthogonal DNA sequences, so that different targets are labeled every time. This means that there is no simultaneous blinking from two neighboring docking strands, which gives the opportunity to visualize them and localize them precisely, as the fluorescent signal emits at different moments. As a result, it not only surpasses the diffraction limit but also eliminates photophysical effects occurring at distances less than 10nm, thereby enhancing lateral resolution and opening new avenues for the study of DNA nanopore dynamics.

In conclusion, our work sets the stage for further advancements in the field of nanoscale imaging and nanopore research. By addressing current limitations and pushing the boundaries of imaging techniques, we hope to unlock new insights into the behavior and function of DNA nanopores.

7. Appendix

A.1 Sequences of staple strands

| Name | Sequence |
|------------|--|
| Pore_ST_1 | GGTTTAGATTTTCGTCGCTAGTACATAATCAGAGCCAATAGGT |
| Pore_ST_2 | GTAATCATGGTCATAAGAGTACCTTTAATTGC |
| Pore_ST_3 | CAAATTCTTACTAATTTTCATCT |
| Pore_ST_4 | GTAGGGCTTCAAATGGTGGAAACGTAAGTTTTGTCGTCTTTATAG |
| Pore_ST_5 | GATTTTGCTAAATGATACAACATCACTTGCTGGTAAAATGAAA |
| Pore_ST_6 | GAAAGACGATAACATAACGCCAAAAGGAATTACGAGGAAAA |
| Pore_ST_7 | GAAAGCTTGACGGGGCTCCAGTGGAAAATACATTTTGACGC |
| Pore_ST_8 | CATCTCAGGACGTTGGGAAGAAAAATCTACG |
| Pore_ST_9 | AATGTCATACATGGCTTTTGACAACCTTTTGCAAATCTGGT |
| Pore_ST_10 | ATGTAATTTAGTCTGCGAACGA |
| Pore_ST_11 | AACATAGCTATCTTACCGAAACAAAGTTAATAATATGCCAGTA |
| Pore_ST_12 | TCAGGTAACAGTAGTTACAAACCTGAGCAAAAAGAAGTAGC |
| Pore_ST_13 | CGCATTAGACGGGAGAATTAAGT |
| Pore_ST_14 | AAATCGGTTGTACGAAATCCAATAAATCATAC |
| Pore_ST_15 | ATAAGAGAAAGTTTCATCAGACTGTAACCGCCTCCCTCAGACACC |
| Pore_ST_16 | AACACAAAAACAGGACCTGACATTGAGACATTATGACCCTG |
| Pore_ST_17 | TAGCTGCTCCATGTTACTTAAACACTCGGAATCGCTCAACA |
| Pore_ST_18 | GCCGACAATGACAACAAGGTGAATTATCATAAATAAGTATATAACAAA CA |
| Pore_ST_19 | ACTATGGGATTTAGAAACCGTCTATCATTTTGGGGTCGATAAA |
| Pore_ST_20 | TTAACAATCGCAAAAAATACTGAGAGCCAGC |
| Pore_ST_21 | TCGCCATGTAATGGGTCAACATTAATGTGAGCGAGTAAGCCA |
| Pore_ST_22 | TAGAGCGTCTTTGTTTAATTTCAACTTTAAT |
| Pore_ST_23 | TGACGCATCAATTGCGCGTATGCTTTCCTCG |
| Pore_ST_24 | AGCCCTCATAGGTCACCAGCAAAGGCCACCGAGTAGTATAACGACC A |
| Pore_ST_25 | ACGGAGTAAGCAGATAGCCGAGCCCTTTTCGAG |
| Pore_ST_26 | ATTAGACAAAGTAGTAATAGGAG |
| Pore_ST_27 | ACGCCAACGTAGATTTACACC |
| Pore_ST_28 | CACCTGCAACAGTAGAAGAAAATGCTGACAACAGTTGACTTGAGCC |
| Pore_ST_29 | GGCGACATTTTGAATTGAGAACTACGAAACCCCGAGCGATTATATGT C |
| Pore_ST_30 | TCAACTAAAAAATTT |
| Pore_ST_31 | GAAAGCGCAGTCTCTGAATTTAGAAAGGAGGTTGGGTGCGT |
| Pore_ST_32 | ATGCAGAAGATATATGTACAAATCAAAGTAAGCGCCCCCTG |
| Pore_ST_33 | TAATACTTTTTCGTTCCCAATGCAGAGGCTCATGAGGAAGTT |
| Pore_ST_34 | GACGGGTGCCGCAATAGTGGCCGTCAAGCCTTGATTTAGGAT |
| Pore_ST_35 | GCTGGCGAAAGGCGCCAGGGTTTTCCAGAGAAGGAATTCAC |
| Pore_ST_36 | GCAAAGTAATGTAGATGGGCGCATTGCGTTGCGGATTGACCTCAG |
| Pore_ST_37 | CGCTCTACTAAAGGCAAGGTACA |
| Pore_ST_38 | ACCCATCAATATTTTCAATTAATCGCGCAGAGGCGAAGCA |

| | |
|------------|--|
| Pore_ST_39 | AACCCACAAGACAAAGCTG |
| Pore_ST_40 | GTCCAGACGACGCTCAACATGT |
| Pore_ST_41 | AATAAGTTTTTAGCAAGCCCACCAGACGTAAAAGCTATAT |
| Pore_ST_42 | CCAGGCCCCAGCAGGGGTGGGCCAGCGACGAGCTCGAATTC |
| Pore_ST_43 | CTTGTTTCATCGTATGCGATTTTAAGAAGCTGGCTCATGAAT |
| Pore_ST_44 | TTGAATAGCCCTAAAACATCACCC |
| Pore_ST_45 | AGCGACAGAATCAAGTTTGCCAGAC |
| Pore_ST_46 | CTTTTTAACCTTATCTAAAATA |
| Pore_ST_47 | TTCCCAGTTGAAATATCTGGCCTCAAATATCAAACCTTCA |
| Pore_ST_48 | TCCGAGACTACTCTTTAGGTAAA |
| Pore_ST_49 | AACGCGAGAAAACCTTCTTTGAT |
| Pore_ST_50 | CCTATGTCTGGATATAAAGTGGCTACAGGAAACCGAGGAAACGCAA CA |
| Pore_ST_51 | TAATTTTTTCAATCCTCATAGCACTAAGTTGTAAAGCCTCTTC |
| Pore_ST_52 | AAACTCCATCCTTTTGTACC |
| Pore_ST_53 | TTGAATACTTCTGAATAATGCCTGATTGGCAAATATTTAAATTGATAA |
| Pore_ST_54 | AACCGATTGAGGAATTAGAAAAT |
| Pore_ST_55 | AAACAAATAACGTTGAAAAAATCATTCATTTTTGGCCTCAG |
| Pore_ST_56 | CTGATAAATTGCCAAGCGCAAATGTTATTTAACA |
| Pore_ST_57 | ACAGGAGGTTGAGGCAGGTCAGGAGCCTTAGACGCTGTGAATATAA TCTG |
| Pore_ST_58 | TTAATAAAATATTTT |
| Pore_ST_59 | GTATCACCGTACTCAGGATTATTCAATGTGAGTCAAAGATG |
| Pore_ST_60 | ATTCGACAACCTCGGGATTTAGTTAGATTATAATGCCATCTTT |
| Pore_ST_61 | GCCTGCCGCCACCCTCAGAGCGCCGCCACCCTTGCTTACAG |
| Pore_ST_62 | TAAATGAATGGCTATTAGTCGCACAGACTTTGATGGTGGTTCCGCGG T |
| Pore_ST_63 | AGGGAACCGAAAATAGAAAAACAGTTTATCA |
| Pore_ST_64 | TCAATCGTCTGAAATTTTAGTCAGTATAACAAAAGACAAAAG |
| Pore_ST_65 | CCACACACCGCCTTGCTGAATCAGTTGGCTCAAACCTAGTT |
| Pore_ST_66 | CTTTTGCGTATCAGCTTTAATTGCAGAAGAGTAAACCAG |
| Pore_ST_67 | GGCGCGCTTAATTTGGGGCTGTCCATCCCATGTACCAGAGCC |
| Pore_ST_68 | AATCACCGGAACCAGAGCCGAATTACCACAAACATTTGCGCTG |
| Pore_ST_69 | ACCAGCGCCAAAGAATACACTAGCC |
| Pore_ST_70 | TAAGAGCAAGAAATAATAATTATCAACAAGGTAAA |
| Pore_ST_71 | TTCGGTCGCTGCAGCTTGAATAA |
| Pore_ST_72 | ACATATAAAAGAAACGCAAAGTGTACAGAGATA |
| Pore_ST_73 | CTAGAGGATCCCCAGGAAGGTCCGGCTTAACAACTAAAGGAA |
| Pore_ST_74 | TCGGAACGAGGCATTTTCGTGCA |
| Pore_ST_75 | CCACCAATATGAAAAGATTCAAAGGGTGAGAAAGGAGCG |
| Pore_ST_76 | TAGCGGGGTTTTGCTCACGATTAAGACATTTGATATCGCCAT |
| Pore_ST_77 | ATTGTAGATAATTTGGGTAAGGGATGTGCTGCAAGGAGCT |
| Pore_ST_78 | GAACACGCAAATTACGCCAGTAAAGGGATTTTAGACGGGC |
| Pore_ST_79 | AACCGCCACCCTCAGAACCCTTATAATCAGTGAGAGAATCAGA |
| Pore_ST_80 | TTTCAGCGCCGCTACAGGACCGCCGCGAACGTGGAGACAGTCAA GAGC |

| | |
|-------------|--|
| Pore_ST_81 | AATATACAAAAAGCCCAGAGAATCGATGAACGGTAATCGTGAAT |
| Pore_ST_82 | GTAATTCTTTTAAATAGTCA |
| Pore_ST_83 | AGATCTGGCAAGTGTAGCGGGTGT |
| Pore_ST_84 | GCGGGAGCGGTGCCGTAAAGC |
| Pore_ST_85 | ATTGCTTTAAACTAGCATGT |
| Pore_ST_86 | CCAGTAGCACCATTACCATTAGAAA |
| Pore_ST_87 | TTCAATAGGTCACGTCCTTCTCTGGTGGATCCTTTGCCCGA |
| Pore_ST_88 | TAACAGTGCCCGTATAAACATCGGCCTTGCCTGAGTGCCACGCCGA A |
| Pore_ST_89 | TAAGAGCCTTAAATCAAGATTAGTTGCTA |
| Pore_ST_90 | GAAACGATTTTTTGTTTAACGTCAAAAATGCATAG |
| Pore_ST_91 | AATCTAAACTTCACCGCCTGG |
| Pore_ST_92 | TATGCGTTATATCTGACCTGCCA |
| Pore_ST_93 | ACGTTATTAATTTATGCTGTAGACAATAAACCCCTCAGCAGCG |
| Pore_ST_94 | CCAAGCGAGGCGAATTTTATCCTGAATCTTACCAACCAGT |
| Pore_ST_95 | ACTATAGAATCCTAAAACAGGAAACAATAAC |
| Pore_ST_96 | AGAGGCTGAGACTCCTCAAGTCACGACCAACTAATTTGGGAAGTTCC |
| Pore_ST_97 | CCTATTTTCGGAACCTATCTCAATCAAGGAATTGGGGGCGGTC |
| Pore_ST_98 | CCCTCGTAACACTGAGTTTCTTAGCGTAAAAAGGTGCATT |
| Pore_ST_99 | AAGGCGGATATTCATTACCCCCTTATTACGAAAGACGCGTTTTA |
| Pore_ST_100 | TTTTGCACCCAATTT |
| Pore_ST_101 | GAGGAGGTCTGAAGCCAGCTGGCGATCGGTG |
| Pore_ST_102 | TATCGCGGATGGTTCAAAGCAGGGAGTTGTTAGCAAACGTAGAATAA T |
| Pore_ST_103 | ACCAACCTTTTTATGGAAACATTAATTAACCACCGGAGCGCGTTT |
| Pore_ST_104 | AGAACTGGCATGATTAAGACTAAATCAACCACT |
| Pore_ST_105 | AGTATTAGCTGGTTTTGAGACGGGCAACAGCTGATTGCCGCAT |
| Pore_ST_106 | CCCCTTGCTTTGAGGCCGATAATCCTGAGAAGTGTTGCCA |
| Pore_ST_107 | TGGGCTTGAGATGCCAGAGCC |
| Pore_ST_108 | ACCACCCTCATTTTCAGAGGAACGGTAACCGTTAATGCGCGT |
| Pore_ST_109 | GAGAGGGTTGATATAAGTAATGATGAATTTTTTAAACATCGGGAAAAT |
| Pore_ST_110 | ACTGAATACCGAGAAAAAGCGGTAAATATTATTTTGTCAACATCCTGA |
| Pore_ST_111 | ACTAATTTAGCGTTCCATATACTGTAAATCAGGT |
| Pore_ST_112 | CATGATCAGTTGAGATTTAGGAATACCACAT |
| Pore_ST_113 | GCTATTACCAACCCGTCGGAT |
| Pore_ST_114 | CAGGACGAGCACAAAGAGTCGCGAGCTGACGATCTACACCAA |
| Pore_ST_115 | AAACGCTCATGGAGTAGCAATACTTTTTCTAGTAAATGAATT |
| Pore_ST_116 | ACGGCCATATCAAATTATTATTA |
| Pore_ST_117 | TAGTAGTAGCATTAACTAACCTCAGAATAGCA |
| Pore_ST_118 | ATGATCTTTCCTACGGAACAACATTATTACAGGTAGCCTG |
| Pore_ST_119 | TTCATCAAGAGAATACATAGCGGATTGCCGGAAGC |
| Pore_ST_120 | AATTACTACCGTGTGACCGTCACCTCAGCGGAGTGAGAATACCG |
| Pore_ST_121 | CATTGTGAACGATTT |
| Pore_ST_122 | TACAGAGGACAGATGAACGGACACCACGCAAAAATCGGAATCAT |
| Pore_ST_123 | ACGTTGAAAACTTTCATTTGCCG |
| Pore_ST_124 | GGGTAAAATACGATAGCAGAGTT |

| | |
|-------------|---|
| Pore_ST_125 | ATAGCGATAGCACATTTAACAA |
| Pore_ST_126 | ACAGGTCAGGATTAGAGAAATCGCCCACGCAT |
| Pore_ST_127 | CCGGGCCACCAGAACCACCACCAGAGCCTTTTCCCTAAGT |
| Pore_ST_128 | ATTCGAGCCTTAGAGCTGCTTTTCGAAAAAAGGCTCCAAAAGACG |
| Pore_ST_129 | TATTAGCGTTTTGTATCGGTTGGAT |
| Pore_ST_130 | GCTGCGCAACTGAGATTAGAAATTTATCATCTCCAAAGGTGA |

A.2 Sequences of strands for PAINT

| Name | Sequence |
|-------------|--|
| Pore_PT_1 | TTTTTCTTCTGCAGGTCGACTTTTTCTTCATTA |
| Pore_PT_2 | TTAATTAGCAATTTTCTTCATTA |
| Pore_PT_3 | AGCATATCCAGTTTTCTTCATTA |
| Pore_PT_4 | CGGACGACGGCTTTTTCTTCATTA |
| Pore_PT_5 | AATTAAGCAATAAAGCCTCAGGTTTAGTACCGTTTTCTTCATTA |
| Pore_PT_6 | CAGTGCCAAGCTTGCATGCTATTCTGAAACATTTTTCTTCATTA |
| Pore_PT_7 | ACGTCAAATTGCAACAGGAATTTTTCTTCATTA |
| Pore_PT_8 | GAGTCTGGAGAGCATAAAGCTTTTTCTTCATTA |
| Pore_PT_9 | AACAATATTACCGCCAGCCGGAACGGGGTCATTTTCTTCATTA |
| Pore_PT_10 | CTGTAGCCGACTTTACAAACATTTTCTTCATTA |
| Pore_PT_11 | CAAAATTAATTAAGTATTAGTACCAGGCGGATTTTTCTTCATTA |
| Pore_PT_12 | GGACAAGAAAATTTTTCTTCATTA |

A.3 Sequences of BARREL 5 strands

| Name | Sequence |
|-------------|--------------------------------------|
| Pore_BR5_1 | AATCAATAACAAGAAAACCAGAAGAGGCTTTGAGG |
| Pore_BR5_2 | AACCTCCCAATGCTTTATTC |
| Pore_BR5_3 | TCAGCAAGTACCGGTAAATTGAGTTA |
| Pore_BR5_4 | CCCTCGTTCAATACTGCATCTTTGGGCACCAACCT |
| Pore_BR5_5 | GAGAATGACTAAGAACCCTTGAAAAAATAAACAGC |
| Pore_BR5_6 | AGATTAAGTTTTTATTACAAGAACCCTTGCCCTGAC |
| Pore_BR5_7 | CCGGTATTCCATAAATGAATAAGTTTGACGGAAAT |
| Pore_BR5_8 | ATTCATTGGGTTTTGACGAGGCGCAGACG |
| Pore_BR5_9 | ATAGCGTCTACCAGACTCCGCGACCAGCCTTTACA |
| Pore_BR5_10 | ATAGCGAGGTAATAGTGAAA |
| Pore_BR5_11 | GCAAGCCGAGGAAGCCCGCAGTATAAAGGCCG |
| Pore_BR5_12 | CTAATAGTTTTAAAGATTATAAGAAAAGATTT |
| Pore_BR5_13 | AGTCCTGAATCGGCTGAATAGCAAAAGTCAGAGG |
| Pore_BR5_14 | ACCCTGACGCAAATCACCAGGCGCATAGG |
| Pore_BR5_15 | ATTACCGCGGAAGCAAACATA |
| Pore_BR5_16 | TTCCAAGAACGGCGCCTGTCCGA |

A.4 Sequences of BARREL 3 strands

| Name | Sequence |
|-------------|--|
| Pore_BR3_1 | GAGAGAATAACATTGCAGATAAAACCAAATTTCAATCAACTTATCCC |
| Pore_BR3_2 | CGTCACAATATCTTCAAACATGTTTTCAATCAACTTATCCC |
| Pore_BR3_3 | AGAGGGGAGGCTTTTGCATGCCTTTCAATCAACTTATCCC |
| Pore_BR3_4 | ATTTGGGGAGGGAACTGTTTAGCAGAAAACCTTTCAATCAACTTATCCC |
| Pore_BR3_5 | TGAAACCATCGTAATGCCATCGCCATTAGACTGGTTTCAATCAACTTATCCC |
| Pore_BR3_6 | CCCCTCAGACTTGCGGGAAATCTTTCAATCAACTTATCCC |
| Pore_BR3_7 | TCATCGGGTAGCAACACCGACAAAATAGATATTTCAATCAACTTATCCC |
| Pore_BR3_8 | GAGAAACACCAGAATTACCTTAGGAATCTTTCAATCAACTTATCCC |
| Pore_BR3_9 | CATATTATTTATCCCAGCTACTTTTAGCGTTTCAATCAACTTATCCC |
| Pore_BR3_10 | ATAGTCACCCAATAGCAATATTTTTCAATCAACTTATCCC |
| Pore_BR3_11 | CTCATTGAGTTATACCAGGAGAACAATTTCAATCAACTTATCCC |
| Pore_BR3_12 | AACACAAAGATTCTAGAAACCTTTCAATCAACTTATCCC |
| Pore_BR3_13 | ATTTCTTAAAAGGCTTGCGAACCAGACATCAAATTTCAATCAACTTATCCC |
| Pore_BR3_14 | TAATTTGCGCTAACGAAGGCTTATTTTCAATCAACTTATCCC |
| Pore_BR3_15 | GGAAAGCAACACTATCATAATTTCAATCAACTTATCCC |
| Pore_BR3_16 | TATTCATTAAACCTAACACCAGGTCTTTTTTCAATCAACTTATCCC |
| Pore_BR3_17 | GAGGAGCCAACGTCATAAATTTTCAATCAACTTATCCC |
| Pore_BR3_18 | GCAGAACGGTATTAACCTAATTTTCAATCAACTTATCCC |
| Pore_BR3_19 | TTTTATTTTCGACCCATCTTTCAATCAACTTATCCC |
| Pore_BR3_20 | GTAATTGAGCGCTAACGAACCTATATCATTTCATCAACTTATCCC |

A.5 Sequences of CAP short strands

| Name | Sequence |
|-------------|---|
| Pore_CPs_1 | TCAGGTAAAATTGCTGTGC |
| Pore_CPs_2 | TCTCCGTGGGAACAAACGGCGCTCACTGCCCGCTTCTACAG |
| Pore_CPs_3 | AAAACGCAAGGCCAATAACCTGTTTTATGGAAGAAA |
| Pore_CPs_4 | CGAAAAATCCCGACCTGAAAGCGTAAGAATACGTGTTTA |
| Pore_CPs_5 | ACTAAATCGGAACCCTAAAGGATCACCATACCCGCCGCTAG |
| Pore_CPs_6 | AGGTTATTCAACCGTAATTCA |
| Pore_CPs_7 | CAATCATATGTACCCCGGTTGTAAACGTTAAATTGCGAGAA |
| Pore_CPs_8 | TTAACGTCAAATTGTATAATTTGGATTGGAGAAGC |
| Pore_CPs_9 | TTCTTTATAAATCAAAGAGCC |
| Pore_CPs_10 | CCCTGAGAGAGTTGCAGCAAGAAATCGGCCACCAGCGCGA |
| Pore_CPs_11 | CCAGTTTGAGGTTAATCGTAACCGTGCTAAAAGTT |
| Pore_CPs_12 | GAGGTGAGTACAAATCCTGAATATTTTTAGCTGTT |
| Pore_CPs_13 | GGCACCGCTTTCGCTAATGAGTGAGCTAACTCACAGGAC |
| Pore_CPs_14 | GAAGATCGCCTGGGGTCAGTCGGGAAAAAGCAC |
| Pore_CPs_15 | GCGAAAGGCCGCGAGAAAGGAAGATGGATTA |
| Pore_CPs_16 | AAAGAATATTTTATGATGGCAATTCATCAATATAATGAAG |

A.6 Materials for staple strand mixture

- 48µL of staple strands 1-48
- 48µL of staple strands 49-96
- 34µL of staple strands 97-130
- 16µL of BR5 x16
- 12µL of PAINT x12
- 16µL of CAP
- 20µL of BR3 x20
- 206µL of H₂O

A.7 Materials for final mixture

- 80µL of scaffold 100nM
- 160µL of staple strand mixture 250nM
- 80µL of TAE Tris-Acetate-EDTA, pH=8.3
- 120µL of MgCl₂ x10
- 360µL of H₂O

8. References

- [1] Hernández-Ainsa, S., & Keyser, U. F. (2014). DNA origami nanopores: Developments, challenges and perspectives. In *Nanoscale* (Vol. 6, Issue 23, pp. 14121–14132). Royal Society of Chemistry. <https://doi.org/10.1039/c4nr04094e>
- [2] Howorka, S. (2017). Building membrane nanopores. In *Nature Nanotechnology* (Vol. 12, Issue 7, pp. 619–630). Nature Publishing Group. <https://doi.org/10.1038/nnano.2017.99>
- [3] Lanphere, C., Offenbartl-Stiegert, D., Dorey, A., Pugh, G., Georgiou, E., Xing, Y., Burns, J. R., & Howorka, S. (2021). Design, assembly, and characterization of membrane-spanning DNA nanopores. *Nature Protocols*, 16(1), 86–130. <https://doi.org/10.1038/s41596-020-0331-7>
- [4] Burns, J. R., Seifert, A., Fertig, N., & Howorka, S. (2016). A biomimetic DNA-based channel for the ligand-controlled transport of charged molecular cargo across a biological membrane. *Nature Nanotechnology*, 11(2), 152–156. <https://doi.org/10.1038/nnano.2015.279>
- [5] *Discovery of DNA Double Helix: Watson and Crick | Learn Science at Scitable*. (n.d.). Retrieved September 2, 2023, from <https://www.nature.com/scitable/topicpage/discovery-of-dna-structure-and-function-watson-397/>

- [6] Dey, S., Fan, C., Gothelf, K. v., Li, J., Lin, C., Liu, L., Liu, N., Nijenhuis, M. A. D., Saccà, B., Simmel, F. C., Yan, H., & Zhan, P. (2021). DNA origami. In *Nature Reviews Methods Primers* (Vol. 1, Issue 1). Springer Nature. <https://doi.org/10.1038/s43586-020-00009-8>
- [7] Bell, N. A. W., & Keyser, U. F. (2014). Nanopores formed by DNA origami: A review. In *FEBS Letters* (Vol. 588, Issue 19, pp. 3564–3570). Elsevier B.V. <https://doi.org/10.1016/j.febslet.2014.06.013>
- [8] Hu, Q., Li, H., Wang, L., Gu, H., & Fan, C. (2019). DNA Nanotechnology-Enabled Drug Delivery Systems. In *Chemical reviews* (Vol. 119, Issue 10, pp. 6459–6506). NLM (Medline). <https://doi.org/10.1021/acs.chemrev.7b00663>
- [9] Xing, C., Huang, Y., Dai, J., Zhong, L., Wang, H., Lin, Y., Li, J., Lu, C. H., & Yang, H. H. (2018). Spatial Regulation of Biomolecular Interactions with a Switchable Trident-Shaped DNA Nanoactuator. *ACS Applied Materials and Interfaces*, 10(38), 32579–32587. <https://doi.org/10.1021/acsami.8b10761>
- [10] Feng, L., Park, S. H., Reif, J. H., & Yan, H. (2003). A Two-State DNA Lattice Switched by DNA Nanoactuator. *Angewandte Chemie*, 115(36), 4478–4482. <https://doi.org/10.1002/ange.200351818>
- [11] Marini, M., Piantanida, L., Musetti, R., Bek, A., Dong, M., Besenbacher, F., Lazzarino, M., & Firrao, G. (2011). A revertible, autonomous, self-assembled DNA-origami nanoactuator. *Nano Letters*, 11(12), 5449–5454. <https://doi.org/10.1021/nl203217m>
- [12] Zhou, B., Dong, Y., & Liu, D. (2021). Recent Progress in DNA Motor-Based Functional Systems. *ACS Applied Bio Materials*, 4(3), 2251–2261. <https://doi.org/10.1021/acsabm.0c01540>
- [13] Ke, Y., Meyer, T., Shih, W. M., & Bellot, G. (2016). Regulation at a distance of biomolecular interactions using a DNA origami nanoactuator. *Nature Communications*, 7. <https://doi.org/10.1038/ncomms10935>
- [14] Main, K. H. S., Provan, J. I., Haynes, P. J., Wells, G., Hartley, J. A., & Pyne, A. L. B. (2021). Atomic force microscopy—A tool for structural and translational DNA research. In *APL Bioengineering* (Vol. 5, Issue 3). American Institute of Physics Inc. <https://doi.org/10.1063/5.0054294>
- [15] Platnich, C. M., Rizzuto, F. J., Cosa, G., & Sleiman, H. F. (2020). Single-molecule methods in structural DNA nanotechnology. In *Chemical Society Reviews* (Vol. 49, Issue 13, pp. 4220–4233). Royal Society of Chemistry. <https://doi.org/10.1039/c9cs00776h>
- [16] NANOMETROLOGY: QI offers next-generation AFM imaging mode for nanometrology | *Laser Focus World*. (n.d.). Retrieved August 31, 2023, from <https://www.laserfocusworld.com/optics/article/16549653/nanometrology-qi-offers-nextgeneration-afm-imaging-mode-for-nanometrology>

- [17] *AFM Modes and Theory — AFM Force Spectroscopy - Nanosurf.* (n.d.). Retrieved September 5, 2023, from <https://www.nanosurf.com/en/support/afm-modes-overview/force-spectroscopy>
- [18] Edington, J.W. (1976). *Practical electron microscopy in materials science* (pp. 1-57). New York, NY: Van Nostrand Reinhold Company.
- [19] Tang, C. Y., & Yang, Z. (2017). Transmission Electron Microscopy (TEM). In *Membrane Characterization* (pp. 145–159). Elsevier Inc. <https://doi.org/10.1016/B978-0-444-63776-5.00008-5>
- [20] Park, J., Park, H., Ercius, P., Pegoraro, A. F., Xu, C., Kim, J. W., Han, S. H., & Weitz, D. A. (2015). Direct Observation of Wet Biological Samples by Graphene Liquid Cell Transmission Electron Microscopy. *Nano Letters*, 15(7), 4737–4744. <https://doi.org/10.1021/acs.nanolett.5b01636>
- [21] Luo, W., He, K., Xia, T., & Fang, X. (2013). Single-molecule monitoring in living cells by use of fluorescence microscopy. In *Analytical and Bioanalytical Chemistry* (Vol. 405, Issue 1, pp. 43–49). <https://doi.org/10.1007/s00216-012-6373-0>
- [22] Semwogerere, D., & Weeks, E. R. (n.d.). *Confocal Microscopy*. <https://doi.org/10.1081/E-EBBE-120024153>
- [23] *Total Internal Reflection Fluorescence (TIRF) Microscopy.* (n.d.). Retrieved May 12, 2023, from <https://www.photometrics.com/learn/single-molecule-microscopy/tirf-microscopy>
- [24] Nwaneshiudu, A., Kuschal, C., Sakamoto, F. H., Rox Anderson, R., Schwarzenberger, K., & Young, R. C. (2012). Introduction to confocal microscopy. *Journal of Investigative Dermatology*, 132(12), 1–5. <https://doi.org/10.1038/jid.2012.429>
- [25] Fish, K. N. (2009). Total internal reflection fluorescence (TIRF) microscopy. In *Current Protocols in Cytometry* (Issue SUPPL.50). John Wiley and Sons Inc. <https://doi.org/10.1002/0471142956.cy1218s50>
- [26] <div class="csl-entry">Young, L. J., Ströhl, F., & Kaminski, C. F. (2016). A guide to structured illumination TIRF microscopy at high speed with multiple colors. <i>Journal of Visualized Experiments</i>, <i>2016</i>(111). <https://doi.org/10.3791/53988></div>
- [27] Denham, S., & Cutchey, D. (2009). *Total Internal Reflection Fluorescence (TIRF) Microscopy. Imaging & Microscopy*, 11(2), 54–55. doi:10.1002/imic.200990043
- [28] Abbe, E. (1873). Beiträge zur Theorie des Mikroskops und der mikroskopischen Wahrnehmung: I. Die Construction von Mikroskopen auf Grund der Theorie. *Archiv Für Mikroskopische Anatomie*, 9(1), 413–418. <https://doi.org/10.1007/BF02956173>
- [29] *Resolution | Nikon's MicroscopyU.* (n.d.). Retrieved November 8, 2023, from <https://www.microscopyu.com/microscopy-basics/resolution>

- [30] Schnitzbauer, J., Strauss, M. T., Schlichthaerle, T., Schueder, F., & Jungmann, R. (2017). Super-resolution microscopy with DNA-PAINT. *Nature Protocols*, 12(6), 1198–1228. <https://doi.org/10.1038/nprot.2017.024>
- [31] Renz, M. (2013). Fluorescence microscopy-A historical and technical perspective. In *Cytometry Part A* (Vol. 83, Issue 9, pp. 767–779). Wiley-Liss Inc. <https://doi.org/10.1002/cyto.a.22295>
- [32] Padilla-Parra, S., & Tramier, M. (2012). FRET microscopy in the living cell: Different approaches, strengths and weaknesses. *BioEssays*, 34(5), 369–376. <https://doi.org/10.1002/bies.201100086>
- [33] *ATDBio - DNA duplex stability*. (n.d.). Retrieved May 16, 2023, from <https://atdbio.com/nucleic-acids-book/DNA-duplex-stability>
- [34] Isbir, T., Kirac, D., Demircan, B., & Dalan, B. (2013). Gel Electrophoresis. In *Brenner's Encyclopedia of Genetics: Second Edition* (pp. 165–167). Elsevier Inc. <https://doi.org/10.1016/B978-0-12-374984-0.00580-5>
- [35] *Gel Electrophoresis | AAT Bioquest*. (n.d.). Retrieved November 8, 2023, from <https://www.aatbio.com/catalog/gel-electrophoresis>
- [36] *Using Plasma for Surface Cleaning and Activation*. (n.d.). Retrieved August 4, 2023, from <https://www.brighton-science.com/blog/using-plasma-for-surface-cleaning-and-activation>
- [37] *Plasma Treatment - Learn the basics and much more here | Tantec*. (n.d.). Retrieved November 10, 2023, from <https://tantec.com/the-basics-of-plasma-treatment/>
- [38] Terpilowski, K., & Rymuszka, D. (2016). Surface properties of glass plates activated by air, oxygen, nitrogen and argon plasma. *Glass Physics and Chemistry*, 42(6), 535–541. <https://doi.org/10.1134/S1087659616060195>
- [39] Gupta, V., Madaan, N., Jensen, D. S., Kunzler, S. C., & Linford, M. R. (2013). Hydrogen plasma treatment of silicon dioxide for improved silane deposition. *Langmuir*, 29(11), 3604–3609. <https://doi.org/10.1021/la304491x>
- [40] Leung, C., Bestembayeva, A., Thorogate, R., Stinson, J., Pyne, A., Marcovich, C., Yang, J., Drechsler, U., Despont, M., Jankowski, T., Tschöpe, M., & Hoogenboom, B. W. (2012). Atomic force microscopy with nanoscale cantilevers resolves different structural conformations of the DNA double helix. *Nano Letters*, 12(7), 3846–3850. <https://doi.org/10.1021/NL301857P>
- [41] *ATTO-TEC GmbH - ATTO 647N*. (n.d.). Retrieved March 30, 2023, from <https://www.atto-tec.com/ATTO-647N.html?language=de>
- [42] *Bruker AFM Probes - SCANASYST-AIR-HR*. (n.d.). Retrieved September 3, 2023, from <https://www.brukerafmprobes.com/p-3787-scanasyst-air-hr.aspx>

[43] *Selecting AFM Probes by AFM Technique*. (n.d.). Retrieved September 4, 2023, from https://www.spmtips.com/how-to-choose-by-afm-technique?qclid=CjwKCAjw3dCnBhBCEiwAVvLcu_XmAVLMMa_P09QIVn6DxNZ52SrUDVmyhPcJT5Dv03DDrMkFpgCTYRoCNhkQAvD_BwE

[44] Wang, Y., Schnitzbauer, J., Hu, Z., Li, X., Cheng, Y., Huang, Z.-L., & Huang, B. (2014). Localization events-based sample drift correction for localization microscopy with redundant cross-correlation algorithm. *Optics Express*, 22(13), 15982. <https://doi.org/10.1364/oe.22.015982>

[45] Hards, A., Zhou, C., Seitz, M., Bräuchle, C., & Zumbusch, A. (2005). Simultaneous AFM manipulation and fluorescence imaging of single DNA strands. *ChemPhysChem*, 6(3), 534–540. <https://doi.org/10.1002/cphc.200400515>

[46] Reinhardt, S. C. M., Masullo, L. A., Baudrexel, I., Steen, P. R., Kowalewski, R., Eklund, A. S., Strauss, S., Unterauer, E. M., Schlichthaerle, T., Strauss, M. T., Klein, C., & Jungmann, R. (2023). Ångström-resolution fluorescence microscopy. *Nature*, 617(7962), 711–716. <https://doi.org/10.1038/s41586-023-05925-9>